Suprathermal Magnetospheric Atomic and Molecular Heavy Ions At and Near Earth, Jupiter, and Saturn: Observations and Identification

S.P. Christon[1], D.C. Hamilton[2], D.G. Mitchell[4], J.M.C. Plane[3], and S.R. Nylund[4]

[1]Focused Analysis and Research, Charleston, SC, USA. [2]University of Maryland, Department of Physics, College Park, Maryland, USA. [3]School of Chemistry, University of Leeds, Leeds, U. K. [4]Johns Hopkins University Applied Physics Laboratory, Laurel, Maryland, USA.

Corresponding author: Stephen Christon (spchriston@aol.com)

Key Points:

- Earth's magnetospheric N_2^+, NO^+, and O_2^+ (~43%, ~46%, and ~10%, respectively) argue for ionospheric ion outflow at ~350-550 km altitude
- Outside Earth and Saturn's magnetospheres, levels of heavy molecular (atomic) ions relative to O^+ are higher (similar) compared to inside
- Heavy molecular to lunar pickup ion ratios are >>1, ~1, and <1 in Earth's magnetosphere, the sheath, and the solar wind, respectively

Please Note: Full page versions of the Figures (most with their full caption) are inserted on the first page after the first citation. My version of MSWord inserted extra blank lines (which I could not adjust) at the insertion point.

Please Note: Two versions of Figure 7 are included, one arranged in portrait view, the other in landscape view, for comparison. The content is identical in each, just the arrangement is different.

Abstract

We compare the long-term suprathermal heavy ion composition measured at three planets using functionally identical charge-energy-mass ion spectrometers, one on Geotail, orbiting Earth at ~9-30 Re, the other on Cassini, in interplanetary space, during Jupiter flyby, and then in orbit around Saturn. O^+, a principal suprathermal (~80-220 keV/e) heavy ion in each magnetosphere, derives primarily from outflowing ionospheric O^+ at Earth, but mostly from satellites and rings at Jupiter and Saturn. Comparable amounts of Iogenic O^+ and S^+ are present at Jupiter. Ions escaping the magnetospheres are: O^+ and S^+ at Jupiter; C^+, N^+, O^+, H_2O^+, $CO^+(N_2^+)$, and O_2^+ at Saturn; and N^+, O^+, N_2^+, NO^+, O_2^+, and Fe^+ at Earth. Generally, escaped atomic ions (molecular ions, MI) at Earth and Saturn have similar (higher) ratios to O^+ compared to their magnetospheric ratios; Saturn's H_2O^+ and Fe^+ ratios are lower. At Earth: after O^+ and N^+, ionospheric origin N_2^+, NO^+, and O_2^+ (with proportions ~0.9:1.0:0.2) dominate magnetospheric heavy ions, consistent with recent high-altitude/latitude ionospheric measurements and models; average ion count rates correlate positively with geomagnetic and solar activity. At ~27-33 amu/e: Earth's MIs dominate over lunar pickup ions (PUIs) in the magnetosphere; MIs are roughly comparable to lunar PUIs in the magnetosheath; and lunar PUIs dominate over MIs beyond Earth's bow shock. Lunar PUIs are detected at ~39-48 amu/e in the lobe and possibly in the plasma sheet at very low levels.

1. Introduction

[1.0] A comparison of heavy ion composition in and near the magnetospheres of Earth, Jupiter, and Saturn is presented in order to (a) more clearly identify, better characterize, and fully understand the different magnetospheric heavy atomic ion and molecular ion (MI) populations of the three magnetospheres, and (b) demonstrate and characterize the uniquely different responses

to atomic and molecular ions provided by the time-of-flight, total-energy ion spectrometers used in this and numerous other studies. These two objectives are intertwined and interdependent, so that either one cannot clearly be presented without significant cross-referencing; therefore, both are addressed herein, rather than separately. Of note, the first observations of MI in Earth's ring current and near-Earth lunar pickup ions (PUI) were made with this class of instrument by Klecker et al. (1986) and Hilchenbach et al. (1992), respectively. That Earth's ionosphere contributes significantly to its magnetospheric O^+ and H^+ ion populations is known from persistent investigation and repeated observation (see e.g., Shelley et al., 1972; Yau et al., 1993, 2011, 2012; Strangeway et al., 2005; Moore et al., 2014, and references therein). Twenty-four years ago, Peterson et al. (1994) noted: "Twenty years after the discovery that significant fluxes of O^+ flow out of the ionosphere (Shelley et al., 1972), there exists little or no quantitative information about the relative importance of the various physical processes responsible for the energization and extraction of O^+ and other heavy ions from the Earth's ionosphere". Now, nearly a quarter of a century later, although continual research (e.g., Yau et al., 1993; 2011; Peterson et al., 1994; Ogawa et al., 2010; Andersson et al, 2004; Wilson et al., 2004; Redmon et al., 2014; Strangeway et al., 2005; Haaland et al., 2012; Yu & Ridley, 2013; Skjæveland et al., 2014; Moore et al., 2014; Foss et al., 2017; Shen et al., 2018; and Seki et al., 2019) has clarified much about thermospheric/ionospheric ion upflow, downflow, outflow, and chemistry - there is still much to be learned. The study of Earth's MI populations remains important in that much of the extant O^+ in its magnetosphere is affected by the altitude and local time of MI interactions during outflow. Likewise, the origination location of MI populations at Jupiter and Saturn determines the level of dissociation that creates a number of the atomic ion populations there. Various disturbances in both the sun and the interplanetary medium can result in significant

planetary magnetospheric responses such as Earth's geomagnetic storms and substorms, which directly affect the planet's thermosphere, ionosphere, and magnetosphere and the extant particle populations, both ionized and neutral, therein. Effects including enhanced upward neutral winds, plasma wave activity during disturbed conditions at and above ~110 km altitude, and F region altitude variations occur from low to high geographic latitudes before, during, and after the more intense phases of magnetospheric disturbances (see e.g., Price and Jacka, 1991; Danilov and Lastovica, 2001; Goncharenko et al., 2004; Blagoveshchenskii, 2013).

[1.1] While progress on many details regarding outflow has been made, that is, the models are better and there are more observations fostering better understanding, we still appear to lack some important ion composition information from the upper ionosphere/thermosphere that might help us better understand and characterize ionospheric outflow at Earth. That is, beyond the overview of the Yau et al. (1993) data by Peterson et al. (1994) and the very recent high altitude measurements by Foss et al. (2017) and the ring current measurements by. Seki et al. (2019), there has been little resolution of the vertical interactions affecting ions during outflow. To our knowledge the literature still does not present an overall consensus as to what chemistry and which processes/conditions/mechanism(s) at what latitudes and altitudes result in the variability of outflowing ionospheric ions (see e.g., Welling and Liemohn, 2016). For example, in the recent statistical study by Shen et al. (2018) of electromagnetic-wave-related ion heating at ~350-700 km altitude, the majority of ionospheric ion heating events were found to be associated with core ion downflows rather than upflows. Only recently has quantitative in-situ observational assessment of the relative contributions of N_2^+, NO^+, and O_2^+, three fundamental components of ionospheric chemistry, been revisited by Foss et al. (2017), who reported conclusions generally consistent with the earlier result from Yau et al. (1993) and Peterson et al. (1994) that

ionospheric O_2^+ is a minor constituent at ~400 km altitude. In the ring current at $3.5 \leq L < 6.6$ (where L is McIlwain's L parameter), Seki et al. (2019) find that keV-energy MI are commonly observed during geomagnetically active periods associated with magnetic storms, substorms, and high-speed solar wind streams; the MI are not detected above background levels in the ring current during quiet intervals and their detection probability increases with increasing geomagnetic disturbance level. Our paper cannot identify the causes or details of outflow processes because the outflow energization processes are at core (sub-keV) plasma energies in the high ionosphere/thermosphere, energies and regions we do not sample. However, Geotail, which orbits at several to tens of planetary radii, carries our instrumentation which measures suprathermal energy, ~80-200 keV, ions in the high energy tail of ion distributions. This instrumentation provides information on the relative abundances of the MI that have flown out of the ionosphere. Cassini's complementary observations at Jupiter and Saturn provide us not only with clarifying observational evidence about the number and composition of energetic heavy ions that populate their magnetospheres, but with several critical observations which help improve our understanding of both instruments' responses at all three planets. The information provided herein may provide incentive for various future focused investigations of Earth's ionosphere and thermosphere using new or existing instrumentation and measurements.

[1.2] Two years of ion composition observations from the AMPTE/CCE spacecraft demonstrated that, after O^+, N^+ is the next most important ionospheric origin ion in the storm-time ring current (Gloeckler and Hamilton, 1987). Regardless of this, most studies of terrestrial ionospheric heavy ion outflow to this day discuss one heavy ion species, O^+, completely ignoring N^+ (e.g., Mall et al., 2002; Christon et al., 2002; Ilie & Liemohn, 2011), knowledge of which is important in understanding the chemistry of Earth's outflow processes. At suprathermal energies in the outer

ring current-to-plasma-sheet region, Christon et al. (2002) find that the average flux ratio of escaped N^+ relative to O^+ is ~40% (~20%) during solar minimum (maximum). Using Geotail/STICS data, they found that at ≳ 9-10 Re during solar minimum, the average dayside ~10–210 keV/e N^+/O^+ flux (PHA) ratio is ~0.36-0.40 (~0.38-0.42) over ~1-2 years, with N^+/O^+ ~1 for ~18 hours on one contributing Geotail orbit, while during solar maximum, the average N^+/O^+ flux (PHA) ratio is ~0.22-0.23 (~0.24-0.26) over ~1-2 years. In a collaborative companion study, Mall et al. (2002), used concurrent Wind/STICS data to find that the average nightside ~8-38 Re magnetospheric ~10–210 keV/e N^+/O^+ density ratio was ~0.45-0.6 from 1995 to 1997 (solar minimum) and decreases in 1997 monotonically to ~0.20-0.23 where it remained from 1998 through mid-2000 (solar maximum). The two studies, taken together, clearly demonstrate solar cycle and radial variations of N^+ relative to O^+. In a somewhat comparable situation, escaped ionospheric MI were discovered in the outer ring current by Klecker et al. (1986) and identified as NO^+ and O_2^+. This MI composition was in contrast to an earlier report by Craven et al. (1985) from polar cap observations at ~1.1-3 Re geocentric that N_2^+ and NO^+ dominated over O_2^+ at higher altitudes and latitudes. This difference was considered inconsequential as Craven et al. postulated that the N_2^+ and NO^+ dominance might be seasonal since there was no overall consensus at that time in the relative abundance of O_2^+ in earlier high-altitude observations. The empirical model of Köhnlein (1989) used observations from 6 satellites to show O_2^+, a major constituent below 100-200 km, falling off more quickly at higher altitudes than N_2^+ and NO^+. Later, Hoegy et al. (1991) summarized a number of ionospheric data and/or model studies, showing that the densities of both N_2^+ and NO^+ were likely to be somewhat greater than that of O_2^+ at altitudes of ~400-600 km. Subsequent MI composition consistent with the Craven et al. (1985) and Hoegy et al. (1991) results was reported by Yau et al. (1993) at ~2-4 Re in a study of

mass spectrometer data obtained on hundreds of ionospheric high altitude, high latitude satellite passes. The complementary comprehensive studies by Yau et al. (1993) and Peterson et al. (1994) clearly identified N_2^+ and NO^+ as the principal, comparably-abundant, outflowing ionospheric Mass-30 (~27-33 amu) molecular ion species in high-latitude, high-altitude measurements at 2-3 Re. Yau et al. (1993) reported O_2^+ to be about an order of magnitude smaller and Peterson et al. (1994) chose to not discuss O_2^+ in their study.

[1.3] Christon, Hamilton, et al. (1994) and Christon, Gloeckler, et al. (1994) referred to escaped ionospheric MI in the magnetosphere as NO^+ and O_2^+, reflecting earlier observations and identification by Klecker et al. (1986) and Gloeckler & Hamilton (1987). The characteristics of MI energy loss processes in the instruments of the 1994 studies (in one, the instrument used herein, and the other, a similar instrument), were not clearly understood at the time. As discovered and presented in this and recent investigations (Christon et al., 2013; 2015), we now understand that atomic and molecular ion energy loss measurements in this class of time-of-flight total-energy instrument must be analyzed differently. Based on the comparisons and evidence presented in this paper which utilizes two nearly-identical charge-energy-mass ion spectrometers in different magnetospheres, we now more fully understand and are better able to more clearly identify and characterize the heavier-than-oxygen suprathermal MI populations at these planets using this class of instrumentation. Singly charged heavy ion populations and their measurement using time-of-flight instruments will hopefully be more clearly understood at all three planets as a result of this study. The improved composition assessment of the long-term MI component of outflown ionospheric MI fluxes observed in Earth's magnetosphere presented herein is intended to help focus planning choices for future thermosphere-ionosphere-magnetosphere observations.

[1.4] The Geotail energetic charged particle data set at Earth contains multi-decadal measurements of ionospheric origin heavy ions that have flown out of Earth's ionosphere into the magnetosphere and some which escape and travel sunward of Earth's bow shock, into the interplanetary medium (see e.g., Christon et al., 2000). A primary purpose of this paper is to clearly identify which MI ultimately flow out of Earth's ionosphere and are subsequently incorporated into Earth's magnetospheric ion population. This identification is facilitated by results from the other primary purpose of this paper, a direct comparison of heavy ion observations at Earth with those at Saturn and Jupiter. In fulfilling these goals, we also address the fate of escaped MI after they leave the protection of the planetary magnetospheres. A factor in and consequence of this study is the recognition that suprathermal lunar pickup ions, PUIs, from the solar wind interaction with Earth's satellite, the Moon, are readily detected in the solar wind from outside the magnetopause to near the Moon. At the lunar distance (~60 Re) sunward of Earth, the solar wind interacts with the Moon, its exosphere, and dust environment (McComas et al., 2009). Additionally, the solar wind interacts with the terrestrial exosphere whose H component, at least, extends to geocentric radial distances of ~100 Re (Baluikin et al., 2019). Further, to our knowledge, little is established about the composition or distance distribution of either Earth's outwardly traveling energetic neutral atom populations. Note that Earth's exosphere is modeled at low-altitudes presuming a six-component exosphere containing H, He, N, O, N_2, and O_2 (see, e.g., McKenna-Lawlor et al., 2005). That solar wind interactions with the Moon produce PUIs has been established by a quarter century of lunar ion observations sunward of Earth, both near Earth, e.g., Hilchenbach et al. (1992), and near the Moon, e.g., Kirsch et al. (1998), Mall et al. (1998), and Halekas et al. (2015). Heavy lunar PUIs are observed to contain at least ~12–42 amu/e ions, primarily of O^+, Si^+, Al^+, P^+, and Ca^+ (Hilchenbach et al., 1992; Kirsch

et al., 1998; Mall et al., 1998) and possibly CO_2^+ (Tanaka et al., 2009), while secondary ion mass spectroscopy of lunar soil simulant samples (Elphic et al., 1991) and actual Apollo regolith samples (Dukes and Baragiola, 2014), that is, the loose surface material covering solid rock, defines a broader range of expected PUIs, additionally including atomic: Na^+, Mg^+, Al^+, Si^+, P^+, K^+, Ca^+, Ti^+, Mn^+, and Fe^+, and molecular: $^{43}AlO^+$, $^{44}SiO^+$, $^{64}TiO^+$, and $^{72}FeO^+$ ions. Of note, Earth's ionospheric meteoric metal neutral and ion layers at ~80-120 km altitude include Na, Mg, Al, Si, K, Ca, Ti, and Fe (Plane et al., 2018), many of the expected lunar PUIs (see also our discussions in Christon et al., 2015; 2017). These metals and important molecules are found in the cosmic dust that forms the zodiacal cloud, a circumsolar disk of small particles and debris produced by asteroid collisions and sublimating comets (Carrillo-Sanchez et al., 2016) that extends to ≥ 10 AU (Nesvorný et al., 2010; Poppe, 2016). The main components of the cometary ices that contribute to cosmic dust are H_2O (~80% by number) followed by CO and CO_2 (Bockelée-Morvan, D., 2011). Therefore, the observation of any of these atomic or molecular ions near Earth may not necessarily suggest their source, the Moon or Earth's ionosphere, both of which have been impacted by cosmic dust for billions of years. Concerted investigations for certain ion species have led to null results, as in the case of lunar Fe^+, which has been sought, but not measured in at least two studies, Hilchenbach et al.(1992) and Kirsch et al. (1998), both using similar instrumentation. We find that, in our current, all-inclusive data set measured in Earth's equatorial magnetosphere (including from the R < ~30 Re plasma sheet and the outer quasi-trapping regions at R > ~9 Re, dayside and nightside), lunar PUIs are not obviously present at levels above the resident terrestrial ion populations therein. In fitting background subtracted Mass-30 ions in the magnetosphere, we show below that inclusion of low levels of Si^+ produces negligible effects on the resulting Mass-30 ion distribution. Finally, our observations are

consistent with the understanding that Earth is the only one of these three planets where the planet's ionosphere supplies the majority of the locally originated heavy ions on the average. While Saturn and Jupiter's magnetospheric heavy ion populations likely originate primarily from their satellites, rings, and/or dust/neutral/ion tori, the Moon does not appear to contribute significantly to Earth's observed magnetospheric suprathermal ion populations in the ~27-33 amu mass range focused on herein. However, we find that higher-mass lunar-and-or-ionosphere species ions are present in the magnetosphere. Outside the magnetopause, lunar ions are readily detected, whereas inside the magnetospheric plasma sheet region, they are not definitively detected, although they are probably present. These intertwined topics are the subject of this paper.

[1.5] Suprathermal Mass-30 ion populations in Earth, Jupiter, and Saturn's magnetospheres are distinct and different. MI in the Mass-30 range are minor components of Earth's total ionospheric contribution to suprathermal ion populations in the magnetosphere and the nearby interplanetary medium, superseded by the atomic ions H^+, He^+, O^+, and N^+ (e.g., Gloeckler and Hamilton, 1987). Comparison of the suprathermal heavy ion measurements from the three planets allow us to utilize the abundant Jovian S^+ measurement peak as a fiducial at 32 amu/e which, when combined with the uncomplicated observations of MI escape from Saturn's magnetosphere, allows us to more clearly identify Earth's magnetospheric MI populations. These observational tools, fiducial and patterned response, have enabled us to better understand the measurements at Earth; allowing us in some situations to separate the ionospheric origin molecular ions N_2^+, NO^+, and O_2^+ from ionospheric origin atomic metal layer ions, including Al^+ and Si^+, and atomic lunar PUIs, including Al^+, Si^+, and P^+, (all with mass numbers between 27 and 31) in near-Earth plasmas with a cautious level of confidence. At Saturn, we report the first

detailed observations of Saturn's H_2O^+, CO^+, and O_2^+ in the interplanetary medium. At Jupiter, no MI from Io or the Galilean satellites appear to survive its intense inner-magnetosphere particle radiation environment, except possibly a trace of CO_2^+, which may be introduced by cosmic dust from the Jupiter family comets (Bockelée-Morvan, 2011). Jovian O^+ and S^+, likely dissociated primarily from Io's molecules and its torus' SO_2, dominate the heavy ion population of Jupiter's magnetosphere. Jupiter's S^+ extends far into the near ~5-AU (astronomical unit) interplanetary medium. At Earth, we demonstrate that primarily N_2^+ and NO^+, but also a detectable, non-negligible amount of O_2^+, flow out into the magnetosphere. We search for lunar PUIs in Earth's equatorial plasma sheet and outer quasi-trapping regions. We provide general information on the overall MI distribution in the ~9-30 Re near-Earth region and the average MI relation to geomagnetic and solar activity. Overall, MI and their dissociation products might play more of a role in magnetospheric dynamics at Jupiter and Saturn than at Earth.

[1.6] The following section contains aspects of the spacecraft trajectories and locations, as well as instrument information. Since several important instrument measurement characteristics are only revealed through the comparison of measurements in different planetary plasma environments and, as far as we know, this will be the first time such information will appear in the literature and used in detailed observation comparisons, these characteristics are introduced and discussed in the following section. A glossary of terminology is located at the end of the paper and duplicated in the supporting information, SI. We attempt to consistently use the terms "outflow" and/or "flow out" to describe transport out of the ionosphere, and reserve "escape" to describe transport out of the magnetosphere.

2. Spacecraft and Instruments

2.0. Spacecraft

[2.0.0] We use data from the functionally identical Geotail/STICS (Supra-Thermal Ion Composition Spectrometer) and Cassini/CHEMS (CHarge-Energy-Mass Spectrometer) ion spectrometers on the Geotail and Cassini spacecraft, respectively. Geotail is an Earth orbiting spacecraft launched in 1992 which explored Earth's deep magnetotail until early-1995, when it was placed into an equatorial ~9 x ~30 Re elliptical orbit where it provides measurements to this day. Cassini was launched from Earth in 1997 and used a Jovian gravity assist in 2001 to arrive at Saturn in mid-2004. Thereafter, Cassini was maneuvered through constantly changing orbit configurations in order to investigate various portions and aspects of Saturn's magnetospheric environs until 2017 when the spacecraft was crashed into Saturn. Data used herein were collected from both instruments for all solar and planetary activity levels. Most high background levels in our datasets likely result from the highest disturbed magnetospheric and/or solar activity intervals which we chose to include in this initial survey of the Earth data. Specific information about the trajectories, though not essential for the focus of this paper, is provided in Figure S2 and Tables S1 to S3 in the SI for reader review. Please note the distinct plasma regime labeling which differentiates the two planets' regimes in the text and highlights their different selection procedures. Instrument information specific to Cassini/CHEMS is at: https://pds-atmospheres.nmsu.edu/data_and_services/atmospheres_data/Cassini/logs/mimi_user_guide_9_26_18.pdf. The documents EPIC_Instrument_Users_Manual-abbr.pdf and EPIC_STICS_PHA_data_product_description.pdf contain Geotail/STICS instrument information and are at: https://spdf.sci.gsfc.nasa.gov/pub/data/geotail/epic/documents/.

[2.0.1] Geotail. Geotail is a spinning spacecraft, with spin axis inclined sunward with an angle of 87º with respect to the solar ecliptic plane, and a spin rate is 20 rpm (Nishida, 1994). A database

283 of 3-hour interval near-Earth plasma regime regions was constructed from contiguous 12-minute
284 interval Geotail data measurement locations in a single regime as determined by the NASA
285 Satellite Situation Center (SSC) Spacecraft Region Identification utility in the manner described
286 in Christon et al. (2017). Plasma regimes (and acronyms) included herein for Earth are: Earth's
287 magnetosphere (SPHERE), magnetosheath (SHEATH), and lobe (LOBE), and the nearby solar
288 wind, interplanetary medium (SW/IM). A map of the plasma regime locations and the locations
289 of the MI observations is plotted in Figure S1 in the SI, and a smaller version of the regime map
290 appears below. Three-hour intervals with mixed region identifications and/or including
291 magnetospheric boundary layers are not used herein. The SPHERE, the primary plasma regime
292 dominated by Earth's magnetic field inside the magnetopause (MP), contains the plasma sheet
293 (PS), ring current, and near-Earth equatorial dayside locations. The low-density LOBE is roughly
294 colocated with and lies above and below the SPHERE in the magnetotail. The SHEATH is a
295 region of disturbed magnetic field and intermediate solar wind dominated plasmas outside the
296 SPHERE. The magnetopause (MP) is the boundary between SPHERE and SHEATH. The outer
297 boundary of the SHEATH is the bow shock (BS), which is the earthward-most boundary of the
298 generally unperturbed solar wind/interplanetary medium, SW/IM, which is dominated by
299 outflowing solar plasma and magnetic field. As a result of its orbit and solar and geomagnetic
300 disturbances, Geotail spends different lengths of time in each plasma regime. These livetime
301 differences affect the observation times therein and therefore the overall relative observation
302 totals in each regime. We do not correct for these differences in this paper, as full quantitative
303 calculations are reserved for a future publication. Rough ratios of the total observation time in
304 the regimes relative to that in the SPHERE are: SPHERE, 1.0; LOBE, 0.1; SHEATH, 0.7; and
305 SW/IM, 1.5; that is, there is ~50% more observation time spent in the SW/IM than in the

SPHERE. We use omnidirectional measurements in this study. Please note that for representative lunar PUI samples, we utilize published measurements of lunar pickup ion composition from Hilchenbach et al. (1992), who used a similar type of ion spectrometer on AMPTE/IRM sunward of Earth's bow shock at ~18.7 Re, and Mall et al. (1998), who used the WIND/STICS ion spectrometer, functionally identical to Geotail/STICS (Gloeckler et al., 1995), in a concerted campaign investigating lunar PUIs on 17 lunar flybys at >17 lunar radii. Note also that because all but one of the Kirsch et al. (1998) study's lunar orbits are likely fully included in the Mall et al. (1998) study, we do not add their data to our set of representative lunar PUI samples.

[2.0.2] Cassini. Information from Cassini's interplanetary cruise to Saturn, including the Jupiter flyby, as well as the first three years of Cassini's orbits around Saturn are used in this paper. Figure S1B shows Cassini's locations from 1999-001 prior to Earth flyby, past Jupiter, to Saturn, and then at Saturn thereafter until 2017-001 in solar ecliptic coordinates. In the SI, Table S2 gives the important events during Cassini's cruise to Saturn. On Cassini's cruise to Saturn, cruise data was obtained as allowed by tracking schedules, so there was very limited data livetime, much less than when Cassini orbited Saturn. During the cruise to Saturn, the CHEMS field-of-view rarely included the solar direction, so the measured fluxes were not necessarily representative of the full three-dimensional interplanetary particle populations. At Saturn, Cassini, a 3-axis stabilized S/C, occasionally rolled for limited intervals. Plasma regimes (and acronyms) used herein for Saturn are: Saturn's magnetosphere (Sphere), magnetosheath (Sheath), and the nearby solar wind, interplanetary medium (Solar Wind). Saturn's Lobe regime is not addressed herein. Figures S1.C, S1.D, and S2 show the Cassini trajectory in Saturn-centered coordinates for an extended interval in which magnetopause and bow shock crossings were identified by a Cassini magnetosphere and plasma science research team (see acknowledgements

329 and Table S3A in the SI). The near-Saturn Solar Wind intervals used herein were collected over
330 28 of the longest continuous near-Saturn interplanetary samples (totaling ~170 hr) from late-
331 2004 to late-2007 using their bow shock identifications (see Table S3 in the SI). Saturn's Sphere
332 data were obtained in the radial range from ~4Rs out to either (1) ~20 Rs or (2) a magnetopause
333 crossing if it was closer (see Christon et al., 2013; 2017). Intervals close to Saturn near ~4-6 Rs,
334 when Cassini was not in nominal, magnetospheric plasma sheet-like plasmas (i.e., radiation
335 belts) were excluded. Lists of the included and excluded R < 20 Rs orbit intervals used herein are
336 in Tables S3A to S3D.

337 2.1 Instruments

338 [2.1.0] The Geotail/STICS and Cassini/CHEMS instruments are ion charge state spectrometers
339 using time of flight (TOF), and total energy (E), to measure singly-charged heavy ions' Mass (M)
340 and Mass per Charge (M/Q) in the ~80-200 keV/e energy range with nearly full three-
341 dimensional measurement capabilities. Although STICS was operational before CHEMS, the
342 instruments are very similar in design and nearly identical functionally. They have been
343 described numerous times in the literature. Geotail/STICS is described in detail most recently in
344 Christon et al. (2017) and Cassini/CHEMS in Christon et al. (2013) (see also Williams et al.,
345 1994, and Krimigis et al., 2004, respectively). The energy range used in this paper is: ~83-167
346 keV/e for Cassini/CHEMS, and ~87–212 keV/e for Geotail/STICS. General features of both are
347 reviewed in Tables S1 - S5 in the SI in which particulars regarding launch, orbit, and cruise,
348 deflection voltages, and onboard species rate classifications. Only new aspects and/or
349 perspectives of the instrumentation will be described in the text. In this analysis, we have
350 resolved several issues related to subtle differences between atomic and molecular ion
351 measurements by this class of time of flight instrument. These differences, described in the

following paragraphs, are utilized throughout the paper and reflect some SI presented in Christon et al. (2013). Although H_2O^+ is presented and briefly discussed herein, full treatment of Saturn's H_2O^+ is reserved for future analysis. An additional point to note is that, except for species close in mass (e.g., N_2^+, NO^+, and O_2^+), the count ratios we report cannot be interpreted as relative abundances because of decreasing detection efficiency with increasing mass, especially for molecules. This paper's primary focus is the Mass-30 diatomic molecular ions.

[2.1.1] Electrostatic focusing selects an ion's energy-per-charge (E/Q) and guides it to pass through a thin carbon foil, and, if not widely scattered, to subsequently strike a solid state detector (SSD). TOF measurement of each incident ion's travel from the carbon foil to the SSD, at regularly cycled deflection E/Q steps permits determination of the ions' Mass per Charge, M/Q, classification. Each ion with a TOF measurement may also have sufficient energy remaining to leave a measured residual energy deposit (Em) above the SSD's electronic threshold energy. If sufficient energy is deposited in the SSD (Em > ~25 keV, the electronic threshold), the ion will also be assigned a non-zero Mass (M) classification based on the E/Q, TOF, and Em. These physical measurement parameters, along with the known instrument state and orientation at the time of ion measurement is called a Pulse Height Analysis event, or a PHA. The instrument's data processing unit (DPU) subsequently increments various rate counters and registers based on the E/Q, TOF, and Em of each incident ion. It also retains a limited sample of the full PHA measurement population and transmits only that sample's information to Earth as a result of telemetry bandwidth limitations. These limited, but precise, PHA samples, not the broader, actively collected counting rates, are the basis of the ability to characterize rare and/or closely intermixed ion species. Counting rates of only some ion species are collected automatically, and even these rates cannot automatically correct for spillover of one

species' events into another species' rate collection box (see e.g., Christon et al., 2002). Fluxes of various other ion species, such as those in this study, can be studied using the transmitted sample PHA information.

[2.1.2] The classification and categorization decisions utilized by the instruments for every measured ion depend on electronically encoded M and M/Q versions of the algorithms we have used to calculate and verify instrument results in this and earlier papers (the interested reader can, for example, review these algorithms in the Geotail/EPIC Instrument Users Manual at https://spdf.sci.gsfc.nasa.gov/pub/data/geotail/epic/documents/). These algorithms convert measured incident energy per charge, time of flight (TOF), and energy deposit combinations for each ion into M and M/Q values utilized in categorization decisions made by the instrument's onboard data processing unit (DPU) and discussed in this paper. Our purpose is not to analyze or revise the algorithms. They and their inherent parameters have been used and kept constant since launch of the spacecraft in the early-1990s. Our purpose is to use the instruments' measurements to understand the differences between atomic and molecular ion responses, a natural consequence for which the algorithms cannot anticipate or compensate.

[2.2.0] Time of flight (TOF) differences: For ions with the same total mass and incident energy per charge MI TOFs are measurably longer than atomic ion TOFs. Molecular ions are known to lose energy in solids in a more complicated manner than atomic ions (see, e.g., Tape et al. (1976) and a discussion in the SI of Christon et al. (2013). Depending on an MI's internal structure, speed, and alignment/orientation with respect to its velocity vector, a diatomic ion, N_2^+, for example, can lose more or (rarely) less energy than two independent N^+ ions entering the material simultaneously at the same initial velocity (see e.g., Heredia-Avalos and Garcia-Molina (2007); Eckardt et al. (1978); and Song et al. (2005), and references therein). In the rare instance

where a MI's axis of symmetry is aligned along its direction of motion, it can lose less energy than when its axis is otherwise oriented, or when its component ions travel independently at the same velocity for the same distance in the medium (see Figure 5 of Arista, 2000). Generally though, in a randomly oriented distribution, more typical in nature, where only a small fraction of molecular orientations are parallel to the general direction of ion travel, ions will generally lose more energy on the average than the independent, identical, constituent, elemental/atomic ions of the molecule, or the rare parallel-alignment ions. This additional energy loss results in a lower particle kinetic energy upon exiting the target and a longer subsequent TOF. This longer TOF results in a higher resultant calculated M/Q value for molecular ions than for atomic ions with the same mass. In a later section we demonstrate the measured difference between molecular ion TOFs to atomic ion TOFs for several selected energy channels.

[2.2.1] Measured residual energy deposit (Em) differences: There are major, observable differences between atomic and molecular ion energy deposits in the SSD. First, MI dissociation and scattering in the carbon foil results in a bimodal set of energy deposits (Em) for MI. One mode represents the small scattering situation in which both constituent ions deposit energy in the SSD. The other mode occurs when only one constituent atom deposits its energy in the SSD and the other atom scatters out of the flight path. Consequently, MI data generally result in bimodal mass distributions as is shown below. After DPU-based corrections for detection phenomena, such as the well-known pulse-height defect (Campbell & Lin, 1973; Ipavich et al., 1978), MIs register higher than anticipated calculated Masses in these instruments compared to atomic ions of equal incident energy. On the spacecraft, the DPU assigns and classifies each ion according to fast Mass-per-charge and Mass onboard encoded algorithmic calculations. An ion's Mass determination is positively correlated with both the: (1) time of flight and (2) energy

421 deposited in the solid state detector. The energy measured by a stopping ion is typically less than
422 the ion's incident energy, and this deficit in measured energy increases with the mass of the
423 incident ion (Ipavich et al., 1978). The DPU's Mass calculation assumes atomic ions, the most
424 typical situation in space particle populations, and this assumption results in an overestimate of
425 an MI's Mass assuming both constituent atoms hit the SSD. For an illustrative example with
426 supporting calculations, see Figure S4 in the SI which compares Ar^+ and the noble-gas dimer
427 Ne_2^+, which both have a total mass of ~40 amu. The DPU algorithm's Mass-correction, which
428 uses the MI's mass determined from the M/Q measurement presuming an incident singly-charged
429 single-nucleus atom, is applied to the two constituent atomic ions, each with approximately one-
430 half of the MI's total mass. As a result of the mass-deficit feature, the constituent ions together
431 deposit more energy than an ion with a mass equal to the sum of the MI's atomic constituents.
432 Assuming an atomic ion, the DPU overcorrects the already higher energy deposit (from each of
433 two atoms) with the higher value related to the heavier atomic ion's (presumed smaller) mass
434 deficit, resulting in a higher than nominal Mass calculation for the MI. The instrument's default
435 calculation clearly overestimates the total Mass for MI which deposit a maximum energy from
436 both constituent atoms in the non-scattering condition.
437 [2.2.2] The above differences between atomic and molecular ions' M and M/Q distributions both
438 enable, and are essential in, the separation of the ionospheric molecular ions, N_2^+, from lunar
439 atomic ions, Si^+, near Earth. In the near Earth solar wind Mass-30 ions have a significant lunar
440 PUI signal of varying proportion depending on the plasma regime of observation. Earth's SW/IM
441 MI data are the most strongly affected, with the PUI most apparent when the Moon is sunward of
442 Earth during high geomagnetic activity intervals which result from high speed solar wind flow.
443 [2.2.3] $^{A}Mq^+$, $^{A}Ma^+$, and $^{A}M^+$ naming conventions. Using the atomic ions at Earth, Jupiter, and

Saturn from our analyses, the M/Q values of atomic ions have been adjusted slightly, e.g., correcting for slight differences in the various instruments resulting from algorithmic approximations and possible foil thickness variations, so that their M/Q response peaks are centered closer to their nominal masses (Christon et al., 2013; 2017). We therefore expect singly-charged heavy atomic ions to be rather close to their nominal mass per charge values. MI species register slightly higher M/Q values than the sum of their component atomic ions, possibly on account of their lower than atomic ion's TOF velocity resulting from the MI's stronger interaction with and subsequent higher energy loss in the instrument's carbon foil. For initial species identification, we, as does the instrument's electronics, rely on the higher-resolution M/Q-resolved, rather than the much lower resolution M-resolved, species determination. Please note that, when we feel it necessary in this paper, we utilize generic, analysis specific naming-conventions for clarity: when addressing data and the method of collection is important, we use $^{A}Mq^{+}$ and $^{A}Ma^{+}$, where A is the mass of the ion and Mq (Ma) indicates that the data is ordered by and binned along the M/Q (M) axis, accumulating over the other variable M (M/Q). Depending on the context of usage, the identity of the ions is either known, unknown, generalized, presumed, or indeterminate because there may be two or more known or presumed individual ion species in the mass-variable range, irrespective of the mass-based variable. The form $^{A}Mq^{+}$ ($^{A}Ma^{+}$) applies to ions identified through and ordered by M/Q (M), categorization and classification, typically in discussions of data collection, and analysis. Ions in the generic ranges ~12-19, ~20-26, ~27-33, and ~39-48 are generically called Mass-16, -20, -30, and -40 ions. If the method of ordering is not relevant in a discussion, we simply refer to $^{A}M^{+}$ ions, such as “Mass-30 ions" are identified as $^{30}M^{+}$ ions. At times, we use histograms of PHA data ordered by either M/Q or M, sometimes with a range criterion placed on the other variable, M or M/Q,

467 respectively. Ordering by M/Q ($^{A}Mq^{+}$) is more often than not utilized for accumulations over the
468 full range of M values. On the other hand, ordering by M ($^{A}Ma^{+}$) is most likely presented for
469 accumulations over a wide range of Mass values and a limited range of M/Q values. Both
470 conventions are used as needed in the analysis.

471 3. Observations

472 [3.0] Figure 1 summarizes major similarities and differences in the three planets' magnetospheric
473 heavy ion composition, with a specific focus on the clear differences between Mass-30 ions
474 (~27-33 amu/e), observed at the three planets, although aspects of the Mass-40 ions (~39-48
475 amu/e) are important at Earth. The high-resolution M/Q measurements are a more accurate and
476 precise tool with which to collect, order, and separate ion species than the lower-resolution M
477 measurements. However, the information conveyed by the M-M/Q color spectrograms is critical
478 for clearly identifying and separating different atomic and molecular ion charge-state species
479 having similar M/Q values. Vertical dashed lines are drawn at 16, 32, and 56 amu/e to simplify
480 data set comparisons and demonstrate the level of accuracy and possible precision of our
481 procedures. The M/Q comparison is accurate enough to demonstrate that the three Mass-30
482 populations are uniquely different: $^{28}Mq^{+}$ and $^{30}Mq^{+}$ ions at Earth; S^{+} dominating at Jupiter; and
483 $^{28}Mq^{+}$ and $^{32}Mq^{+}$ ions at Saturn. Fe^{+}, at ~56 amu/e, is observed at Earth and Saturn, but not at
484 Jupiter or in the interplanetary medium (as shown below). Please note that the generic ion
485 identifier Mq was introduced in the final paragraph of the instrument section.

486 [3.0.0] In our long-term averages in Figure 1, O^{+} is the principal magnetospheric suprathermal
487 heavy ion at all three planets, but not necessarily dominant at all times; levels of H_2O^{+} and S^{+}
488 comparable to O^{+} exist at Saturn and Jupiter, respectively, and the seasonal variation of O^{+} at
489

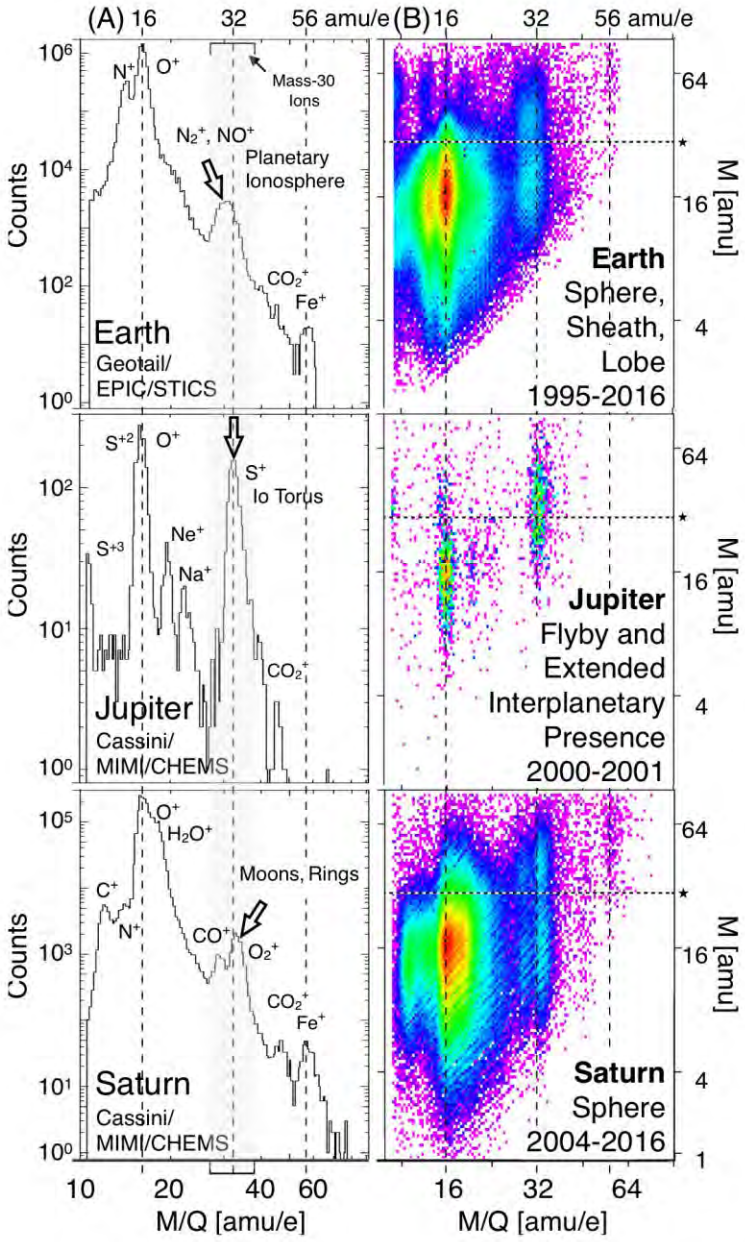

Figure 1. Heavy suprathermal (CHEMS, ~83-167 keV/e; STICS, ~87–212 keV/e) ion Pulse Height Analysis PHA data obtained by: (top) Geotail in and near Earth's magnetosphere; (middle) Cassini during its Jupiter flyby as well as in the interplanetary medium from ~3-9 AU when S^+ was measured; and (bottom) Cassini in Saturn's ≲20 Rs magnetosphere (see text for details). The PHA data are presented as (A, left) mass-per-charge (M/Q) histograms and (B, right) mass (M) versus M/Q color spectrograms (colorbars suppressed). Stars at right and horizontal dashed lines identify M = 32 amu. All data were adjusted slightly in order to center N^+, O^+, and S^+ on their atomic mass in order to account for instrument and spacecraft electronics differences. Mass-30 ions include ~27-33 amu/e. General sources of the Mass-30 ions at each planet are noted.

Earth results in $N^+/O^+ \sim 1$ during solar minimum (Christon et al., 2002; Mall et al., 2002). Additionally, solar wind plasma clearly enters planetary magnetospheres and is subsequently incorporated into their magnetospheric ion populations (Christon, Hamilton, et al., 1994; Peterson et al., 1998; DiFabio, 2012), although solar wind contributions to magnetospheric populations vary by planet and solar season (e.g., Peterson et al., 1981; Fujimoto et al., 1996;1998; Terasawa et al., 1997; DiFabio et al., 2011). As a result of this, the proportion of solar wind pickup O^+ (and/or lunar-origin pickup O^+ in the case of Earth) entering a magnetosphere to the O^+ generated internally, escaping, and possibly reentering at any of the magnetospheres (see e.g., Cohen et al., 2017; Sorathia et al., 2017) is not estimable from single spacecraft studies such as this. Likewise, O^+ escaping from a magnetosphere may not be separable from interplanetary pickup O^+, even using full three-dimensional distribution functions. At Jupiter, the presence of S^{+2} at ~16 amu/e in Figure 1B, middle panel signals that both S and O are important energetic ions at Jupiter and dominance by one or the other may vary depending on the energy range (see e.g., Haggerty et al., 2009). Regardless, in the central magnetotail plasma sheet and dayside equatorial regions of each magnetosphere, O^+ is likely often the dominant heavy ion at all three planets. At Jupiter, O^+, S^+, and Na^+ originate mostly from Io; although icy Galilean satellite data show the presence of O_2, their O_2 is not presumed to necessarily escape the satellites (Johnson et al., 2004). Figure 1 shows that we observe peak $O^+/S^+ < 2$ at Jupiter, while at Earth O^+/N^+ is ~5, and at Saturn O^+/H_2O^+ is ~ 2-3. (Please note that the ions in the prominent O^+-H_2O^+ peak at Saturn are often referred to as the water group ions, or W^+. W^+ ions contain O^+, OH^+, H_2O^+, and H_3O^+; (see e.g., DiFabio et al., 2011, Allen et al., 2018, and Martens et al., 2008). Molecular and atomic ions from the satellites and rings of Jupiter and Saturn are likely the primary sources of their planet's magnetospheric O^+ populations, while, on

515 the other hand, Earth's ionosphere, not the Moon or interplanetary sources, is the source of most
516 of Earth's magnetospheric O^+. The Ne^+ identified near Jupiter in Figure 1, is an interstellar
517 pickup ion (Gloeckler, Fisk, Geiss, et al., 2000; Gloeckler, Fisk, Zurbuchen & Schwadron,
518 2000).
519 [3.0.1] Heavy open arrows in the Figure 1 histograms indicate significant differences in the M/Q
520 distribution of Mass-30 ions at the three planets. Mass-30 ions are a small percentage of O^+ at
521 Earth and Saturn, but comparable to O^+ at Jupiter. Inside Earth's bow shock, Mass-30 ions have a
522 broad, rounded peak centered primarily below 32 amu/e suggesting outright, without any further
523 information, that they are probably dominated by N_2^+ and NO^+, but are clearly missing a coequal
524 O_2^+ component which would have resulted in a peak level extended to and above ~32 amu/e. At
525 Jupiter, the atomic ion S^+ is the dominant Mass-30 ion, its peak centered on 32 amu/e. At Saturn,
526 the well documented, and well understood O_2^+ magnetospheric Mass-30 MI peak is clearly
527 centered at M/Q > 32 amu/e, consistent with our current new understanding of the instruments
528 presented in Section 2. The question remains, how much O_2^+ is present in Earth's magnetosphere.
529 [3.0.2] We briefly present calculations from two recent ionospheric models showing that less O_2^+
530 than either N_2^+ or NO^+ is expected to flow out of the ionosphere for outflow initiated at altitudes
531 of ~250-500 km, consistent with the cited ionospheric studies and our MI observations in Earth's
532 magnetosphere. The large local time variation of ionospheric density, being about two orders of
533 magnitude higher on the dayside than on the nightside, is demonstrated in Figure 2 using ion
534 number density results from two recent ionospheric models, WACCMX (Liu et al., 2010; 2018)
535 and SAMI3 (Huba et al., 2000; 2008). Both are three-dimensional models of Earth's ionosphere
536 and thermosphere, which predict ion profiles that are generally similar to the in situ ionospheric
537 observations of Yau et al. (1993), Peterson et al. (1994), and Foss et al. (2017). Recent
538

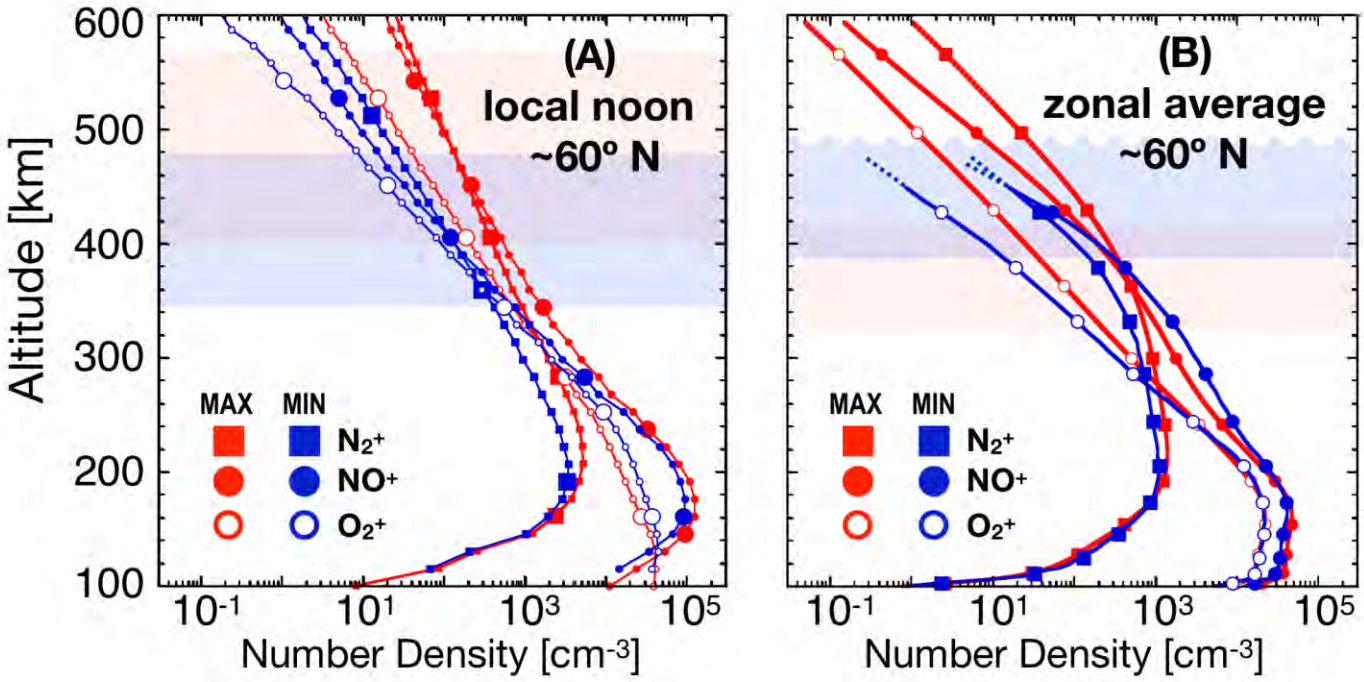

Figure 2. Earth's dayside molecular ion number density profiles of N_2^+, NO^+, and O_2^+ at ~60° N latitude around Spring equinox calculated for solar maximum (MAX) and minimum (MIN) conditions from (A) the SAMI3 ionosphere model near local noon and (B) the WACCM−X thermosphere/ionosphere model for a one-month narrow-latitude zonal average; see text for input parameter and run information. Unique symbols identify and differentiate the three MI species' altitude profile similarities and differences. The red and blue shaded areas, indicate altitude ranges that vary with solar cycle in which the N_2^+, NO^+ densities are approximately equal and O_2^+ levels are somewhat lower, but not absent. This unique molecular ion composition signature is characteristic of outflowing MI (see text).

observations (e.g., Andersson et al., 2004, Wilson et al., 2004, Haaland et al., 2012, and Yu & Ridley, 2013) collectively demonstrate that both the dayside cusp and the nightside auroral zone can contribute substantial quantities of outflowing ions (from cold, sub-eV, to tens of eV energies) to the total ion plasma population throughout the magnetosphere, as well as to the many ionospheric origin ions that are quickly lost downtail (see e.g., Christon, Gloeckler, et al., 1994). Figure 2 concisely summarizes model number densities of N_2^+, NO^+, and O_2^+ in Earth'shigh latitude ionospheric source regions for solar maximum and solar minimum conditions. The model time selections for Figures 2A and 2B are different: in Figure 2A with SAMI3 we calculate 2-day averages for two widely different sets of conditions: first, quiet geomagnetic activity during low solar activity and second, disturbed geomagnetic activity during high solar activity; in Figure 2B, monthly zonal averages around times of solar maximum and minimum are calculated. Calculations in Figure 2B from SAMI3 (at https://ccmc.gsfc.nasa.gov/models/modelinfo.php?model=SAMI3) and WAACM-X (at https://www2.hao.ucar.edu/modeling/waccm-x) show that, although O_2^+ can contribute significantly between ~100-150 km, it becomes a minor component at altitudes higher than ~300-450 km and latitudes ≥50º, locations where ionospheric outflow ion composition is determined. Model outflow from these higher regions shown in panels 2A and 2B results in outflowing MI dominated by nearly equal parts of N_2^+ and NO^+, each generally more populous than O_2^+ by a factor of >3, irrespective of solar and geomagnetic activity (see Table S10 in the SI for the SAMI3 and WACCM-X model run parameters and intervals). That $O_2^+/(N_2^+ + NO^+) < 1$, characteristic of the ionospheric observations noted above, is shown by several other ionospheric models (Koehlein, 1989; Cannata, 1990; Richards, 2013; see also Hoegy, 1991). We note further that in an investigation demonstrating solar cycle variation of ionospheric MI by Richards

(2013), who used yet a different model, O_2^+ was shown to decrease relative to N_2^+ and NO^+ above ~280-290 km. Results from these various models are generally consistent, but the public access to WACCM-X and SAMI3 allows interested readers to look further into the MI compositional aspects demonstrated here. We now resume our investigation of the new information in this report which will reveal that throughout the equatorial ~9 < R < ~30 Re magnetosphere, outflowing ionospheric N_2^+ and NO^+ quantities are comparable, and a relatively smaller amount of O_2^+ escapes overall.

[3.0.3] Differences between atomic and molecular ion responses are immediately apparent in the instruments' color spectrograms in Figure 1B, where atomic ions at all three planets, such as N^+, O^+, S^+, and Fe^+, exhibit single-peaked Mass distributions, but the Mass-30 MIs, N_2^+ and NO^+ at Earth and CO^+ and O_2^+ at Saturn, exhibit two Mass peaks as discussed in the instrument section. No apparent MI instrument responses are clearly evident at Jupiter. Horizontal white, dashed reference lines drawn at M = 32 amu in the color spectrograms (note the stars to the right of the right-hand panels), show that the upper MI peaks are located at Mass values displaced ~25-40% higher than the incident ion's mass, M ~ 28-32 amu. This over-estimation of a MI's total Mass, discussed in Section 2, is visible in Figure 1B at Earth and Saturn for each of the Mass-30 MI distributions. Although the Mass axis is only roughly calibrated, note that Jupiter's S^+ Mass distribution is centered at ~32 amu (midway between 16 and 64 amu on the log scale axis) and the O^+ distributions at all three planets peak at ~16 amu.

[3.1] Jupiter. In Jupiter's magnetosphere, where we obtained the least information, we primarily address S^+, our Mass-30 atomic ion M/Q reference fiducial. Jupiter's high energy particle radiation environment appears to quickly dissociate and ionize most, if not all, molecules into their component atomic ions. These molecules may include SO, SO_2, and S_2 anticipated from Io

(Wilson et al., 2002), CO, CO_2, H_2O, and O_2 from Ganymede, Europa, and Callisto (e.g., Cooper et al., 2001), or Jupiter family comets (Bockelée-Morvan, 2011), and/or NaCl and/or NaOH from Io (McEwan et al., 2007; Kuppers and Schneider, 2000). Io's molecules result in predominantly S^+ and O^+ at suprathermal energies, as evidenced in Figure 3. We do not observe a peak near the expected locations of SO_2^+ and S_2^+ at M/Q ≳ 65 amu/e in or near Jupiter's magnetosphere, suggesting that all ionian SO_2^+ and S_2^+ quickly dissociate before they can be accelerated to suprathermal energies, or that our detection efficiency for the very heavy ions is too low. We presume that a large amount of asteroid belt material in the form of interplanetary dust particles, or IDPs, are also drawn into and present in Jupiter's intense magnetospheric radiation environment. Although we would anticipate all MI to dissociate in Jupiter's magnetosphere, the clear, but small, signal at ~45 amu/e in and near Jupiter's magnetosphere presents a conundrum. The possible species that could result in a ~44-46 amu/e signal are: Sc^+ (with Mass of 45 amu), SiO^+ (44 amu), CO_2^+ (44 amu), and/or possibly $SiOH^+$ (45 amu). The abundance of Sc in cosmic dust, the most likely Sc source at Jupiter, is small, but Si compounds are prevalent in IDPs (Grebowsky & Aikin, 2002; Plane et al., 2016). However, most, if not all, IDP material likely dissociates completely into its component atoms at Jupiter and we assume it unlikely that any IDP origin MIs survive and are observed in Jupiter's magnetosphere. Therefore, assuming that this is likely an MI signal and remembering that MI energy loss in the carbon foil results in a higher than expected M/Q value for MIs than atomic ions, the remaining 44-amu MI candidate (with a ~45 amu/e M/Q value) is CO_2^+. Therefore, this small, distinct peak may be evidence of CO_2^+ derived from Jupiter's Galilean moons (Hibbitts et al., 2000; Gomis and Strazzulla, 2005) or Jupiter family comets (Bockelée-Morvan, 2011). Ne^+, Mg^+, and some O^+ are interplanetary pickup ions (Kallenbach et al., 2000) as the interplanetary data in the bottom panels suggest,

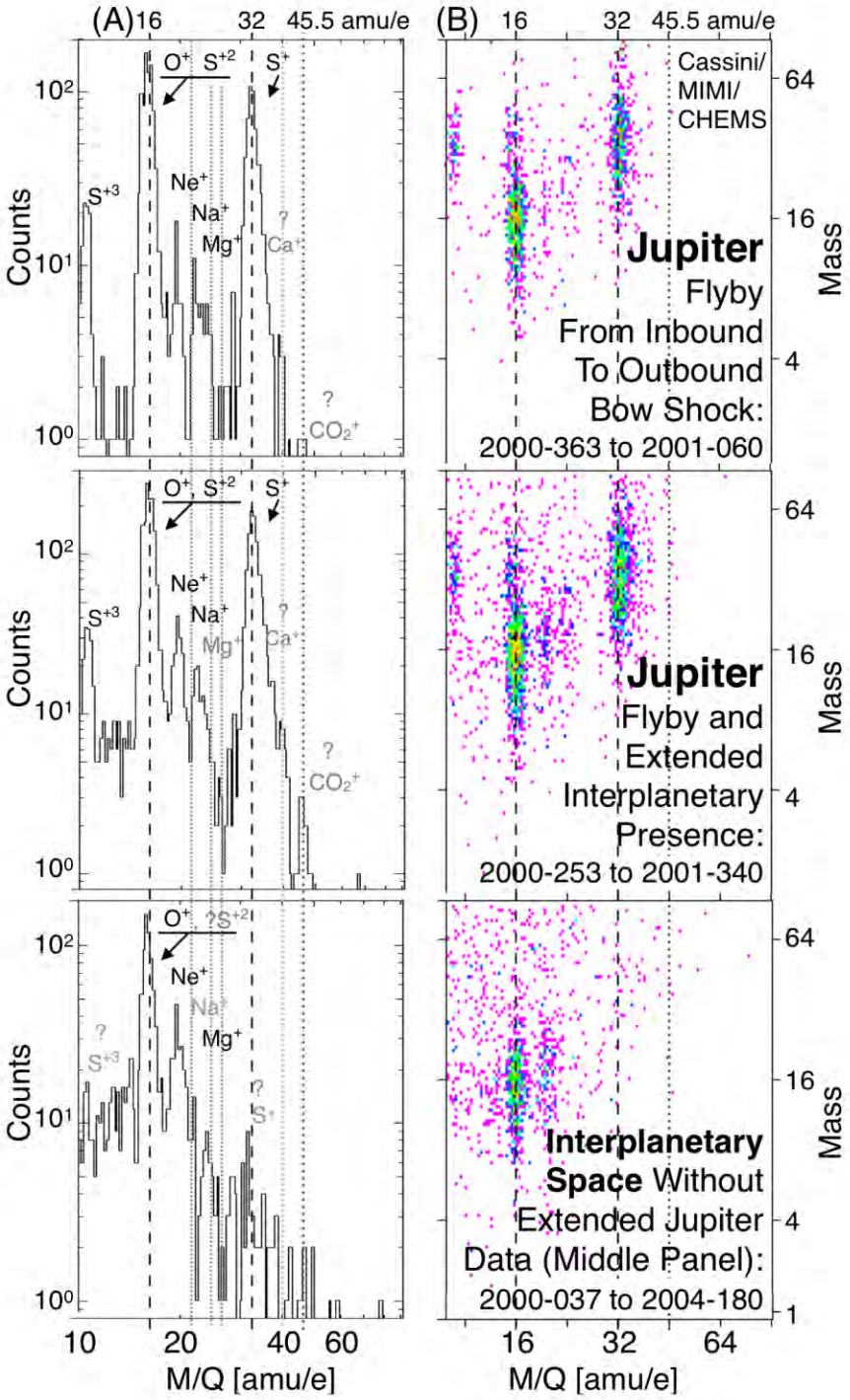

Figure 3. Cassini's measurements of jovian and solar wind/interplanetary medium suprathermal (~83-167 keV/e) ion populations during: (top) the Jupiter flyby between inbound and outbound bow shock encounters; (middle) the extended interval over which S^+ from Jupiter was detected in the solar wind before, during, and after the Jupiter flyby; and (bottom) the ~3 year Cassini cruise to Saturn ,excluding the extended ~1-year interval of jovian fluxes from the middle panel. The tentative identification of jovian magnetospheric Ca^+ and CO_2^+ are noted by lighter dotted lines.

612 although magnetospheric Mg^+ might also derive from outflowing IDP material ablated in the
613 ionosphere of Jupiter (Kim et al., 2001) and/or possibly that of Ganymede, whose diameter at
614 ~0.4 times that of Earth, from which it would be easier to escape. (However, the lack of observed
615 Fe^+ near Jupiter makes an IDP source seem less likely.) Jupiter's magnetospheric Na^+, O^+, and S^+
616 likely derive from Io (Wilson et al., 2002; Bodisch et al., 2017), while the other icy Galilean
617 moons may also contribute to O^+ (Strobel & Yung, 1979). Jupiter's primary contribution to this
618 study is the strong, clear S^+ atomic-ion distribution at 32 amu/e which we use as our Mass-30
619 M/Q reference fiducial. S^+ became increasingly discernible after day 2000-253, ~0.7 AU from
620 Jupiter (Krimigis et al., 2002). S^+ remained intermittently present out to ~6.6 AU and was not
621 detected after days 325-340, 2001 (see Figure 3 and Table S2 in the SI). Note also, that S^{+2} and
622 S^{+3} components, centered at ~32 amu and ~10-11 and ~16 amu/e, respectively, are evident in the
623 upper and middle M-M/Q color spectrograms - a component which would otherwise be masked
624 by O^+ if only M/Q measurements without the accompanying Mass measurements were available.
625 A trace ion signal at ~39-40 amu/e present in and near Jupiter's magnetosphere (3A, 3B), but not
626 in interplanetary space (3C), may represent $^{39}K^+$ || $^{40}Ar^+$ || $^{40}Ca^+$ (please note, that we use the
627 logical symbol " || " below to represent the phrase "and/or" when there are two or more candidate
628 ions that cannot be differentiated). Only $^{33/38}Ar$ and CO_2 have currently been identified in
629 Jupiter's atmosphere (Mahaffy et al., 2000; Kunde et al., 2004). However, although cosmic dust
630 and Jupiter Family comets possibly containing K, Ca, SiO, and CO_2 likely interact with Jupiter's
631 magnetosphere, we will restrict our discussions/references of Jovian Mass-40 ions to Ca^+ and
632 CO_2^+.
633 [3.2.0] MI at Saturn and Earth. Mass-30 ion data obtained at Saturn from late-2004 to late-2007
634 are plotted vertically in Figures 4A and 4B for ease of comparison: (4A) inside Saturn's

magnetosphere at ~4 < R < 20 R_S , in the Sphere (Christon et al., 2013; 2014; 2015) and (4B) in the Solar Wind outside Saturn's magnetosphere at R > R_{BS} (the Saturn bow shock distance). Cassini magnetopause and bow shock crossings were determined by a Cassini magnetosphere and plasma science research team for the years 2004-2007. Lists of the intervals collected for this study are in the SI. Note that we refer to Saturn's R < 20 Rs and R > R_{BS} data as Saturn's "Sphere" and "Solar Wind" data, respectively. The top panel of Figure 2 shows that Earth's Mass-30 molecular ion mass distributions, $^{28}Ma^+$ and $^{30}Ma^+$, overlap significantly. Therefore, the observationally determined distributions in M we show in Figure 4 and discuss below are collected in narrow M/Q range selections near the center of their M/Q distributions in order to limit background spillover from nearby species. Spillover from $^{30}Ma^+$ ions into $^{28}Ma^+$ ions is unlikely, as TOF variations are physically limited toward longer TOFs. The curves for R < 20 Rs are smoothed fits to the PHA histogram. As a result of the uncertainties associated with defining a best fit to the low counting statistics of the R > R_{BS} data, we simply redrew the fitting curves from R < 20 Rs at appropriate levels for the R > R_{BS} data in order to highlight these ions' apparently consistent spectral shape similarity inside and outside Saturn's magnetosphere. For clarity, representative count uncertainties are only shown at two values near the right-hand axis in Figure 4B. No atomic ions appear to be present in these $^{28}Ma^+$ and $^{32}Ma^+$ data collections either inside or outside Saturn's magnetosphere, only molecular ions. The $^{28}Ma^+$ (light blue) and $^{32}Ma^+$ (rose) Mass-30 ions likely dominated by CO^+ and O_2^+, respectively, are more widely separated so there is somewhat less spillover at Saturn (see Figure S8 in the SI). While the species identification of O_2^+ at $^{32}Ma^+$ is much more certain than that of CO^+ at $^{28}Ma^+$ (Christon et al., 2013, 2015; Hamilton and Christon, 2018), noncommittal species descriptors are used for all molecular ion species in this Figure. Both MI species at Saturn display a clear two-lobed shape

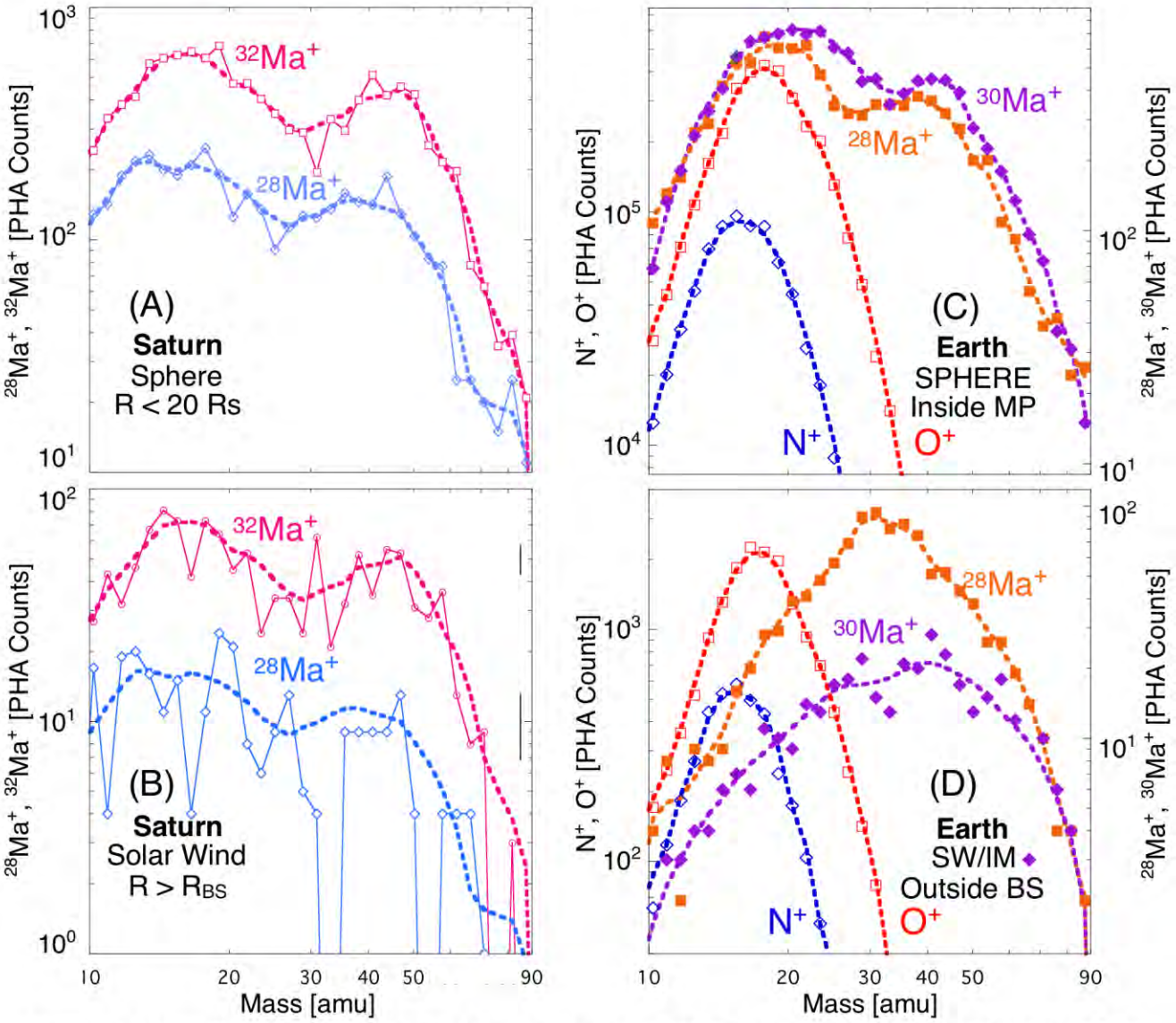

Figure 4. Mass distributions of Mass-30 suprathermal (CHEMS at Saturn, ~83-167 keV/e; STICS at Earth, ~87–212 keV/e) ion data at Saturn and Earth highlight atomic and molecular ion (MI) differences. Data points and smoothed fits are shown. The indeterminate species descriptors "$^{28}Ma^{+}$" and "$^{30}Ma^{+}$" are used as ion species channel names in this figure for primarily singly charged Mass-30 ions selected in narrow M/Q ranges near 28 and 30 amu/e because it is clear that there is an admixture of ion species in at least two cases. The identifier "Ma" represents a M-M/Q spectrogram selection over a limited M/Q, but wide M, range in which the selected ions' species identification is sometimes complex (see text for the full discussion). Mass histograms of $^{28}Ma^{+}$, $^{30}Ma^{+}$, and/or $^{32}Ma^{+}$, heavy ion species having mass numbers of 28, 30, and 32 amu, respectively, are likely dominated by CO^{+} (or N_2^{+}), NO^{+}, and O_2^{+}. At Saturn, data from mid-2004 through 2007 containing: (A) all intervals when Cassini was in Saturn's magnetosphere, the Sphere, at ~4 < R < 20 R_S; and (B) only intervals in the solar wind for which an outbound and a subsequent inbound bow shock (BS) crossing were identified, including travel to and from apoapsis, thus placing Cassini in the Solar Wind near Saturn at R > R_{BS}, the distance of Cassini's bow shock encounters. Representative uncertainties are shown near the right vertical axis in (B). At Earth, data from early-1995 through 2015 are shown for intervals when Geotail was in (C) the SPHERE, Earth's magnetosphere, and (D) the SW/IM, the near Earth, unshocked, solar wind of the interplanetary medium. See text for details.

661 in the magnetosphere and, most likely, in the solar wind, although the statistics are poorer there
662 than in the magnetosphere. The bimodal MI shapes at Saturn are consistent with those observed
663 in Earth's magnetosphere (panel 4C), which suggests measurements of predominantly diatomic
664 Mass-30 MI (see Section 2) inside both magnetospheres. Figures 4A and 4C demonstrate that
665 there is no significant difference in instrument response characteristics to MI inside the two
666 planets' magnetospheres, and that, other than two MI species, we do not detect any evidence for
667 Mass-30 lunar PUI (Al^+, Si^+, or P^+) at measurable levels in Earth's SPHERE plasma regime.
668 Future selective analysis might help reveal times when the atomic lunar PUI in this Mass range
669 are visible in the SPHERE, but that is not our current objective.
670 [3.2.1] Earth. Figures 4C and 4D show the Mass-30 ion mass distributions from Earth's
671 magnetosphere, SPHERE, and the near-Earth solar wind, SW/IM, respectively. The shapes of the
672 Mass-30 ions, $^{28}Ma^+$ (orange) and $^{30}Ma^+$ (purple), compared to those of the dominant atomic ions
673 O^+ (red) and N^+ (blue) at Earth and to the MI data at Saturn in Figures 4A and 4B, indicate that
674 Earth's SPHERE data in Figure 4C contain clear MI responses similar to those from Saturn'
675 Sphere. However, Earth's SW/IM Mass-30 channels in Figure 4D do not contain clear MI
676 responses. Review of Figure 2 suggests that there is no detectible spillover of O^+ into the MI
677 distributions at either planet. Unlike the situation at Saturn, where Sphere and Solar Wind shapes
678 are nominally similar, the shapes of Earth's SW/IM $^{28}Ma^+$ and $^{30}Ma^+$ distributions are not similar
679 to the shapes of either Saturn's or Earth's magnetospheric MI distributions or any single atomic
680 ion's distribution. The less sharply peaked $^{30}Ma^+$ SW/IM distribution's shape is only slightly
681 more similar to the MI shapes in the SPHERE than to the shape of the SW/IM $^{28}Ma^+$. As an
682 operating presumption, we demonstrate below that the difference between Earth's SPHERE and
683 SW/IM Mass-30 ion distributions indicates the presence of lunar PUI responses in Earth's $^{28}Ma^+$

684 and $^{30}Ma^{+}$ SW/IM data. Relative mixtures of PUI and ionospheric contributions present in the
685 two ion channels are not the same. Different portions of the three lunar PUIs' Mass distributions
686 contribute to the two channels, specifically, Al^{+} and Si^{+} in $^{28}Ma^{+}$, and Si^{+} and P^{+} in $^{30}Ma^{+}$,
687 consistent with earlier lunar PUI composition measurements. We now briefly discuss relevant
688 aspects of Mass-30 ion comparisons at Earth and Saturn to clarify the effects of the lunar PUI
689 background interference on our MI observations.
690 [3.2.2]. Figure 5 compares long-term average heavy ion composition measurements normalized
691 to O^{+} in the near-Earth and near-Saturn plasma regimes. Histograms of magnetospheric data are
692 shown in red (measured using red axis values on the left), contrasted with magnetosheath and/or
693 solar wind data in blue (measured using blue axis values on the right). As noted above, the
694 plasma regime label terminologies for Earth and Saturn data are individualized, constructed to be
695 uniquely different visually, so that textual references to each planet's plasma regimes should not
696 to be mistaken for the other's and the reader can clearly and easily differentiate between the two
697 planets in our discussions and comparisons. The labeling differences also highlight the different
698 plasma regime identification procedures at the two planets (see Section 2 and Christon et al.,
699 2013; 2017). Shown are ~21 years of data at Earth and ~3 years at Saturn, so that vertical scaling
700 is consequently different for the two planet's panels. However, vertical scaling for each panel's
701 right and left axes is identical, with the deficit on the right hand axes left open to highlight
702 intensity differences. Dashed fiducial lines at 16, 32, and 56 amu/e are drawn to simplify
703 comparisons (color spectrograms for these Earth and Saturn data are in Figure S3 and nominally
704 drawn, unnormalized individual panels are in Figure S13 in the SI). Despite the vast difference in
705 the Earth and Saturn magnetospheric sizes, the ratios of Mass-16 atomic ion levels in the two
706 magnetospheres compared to their levels in the planets' nearby sheath and solar wind are very

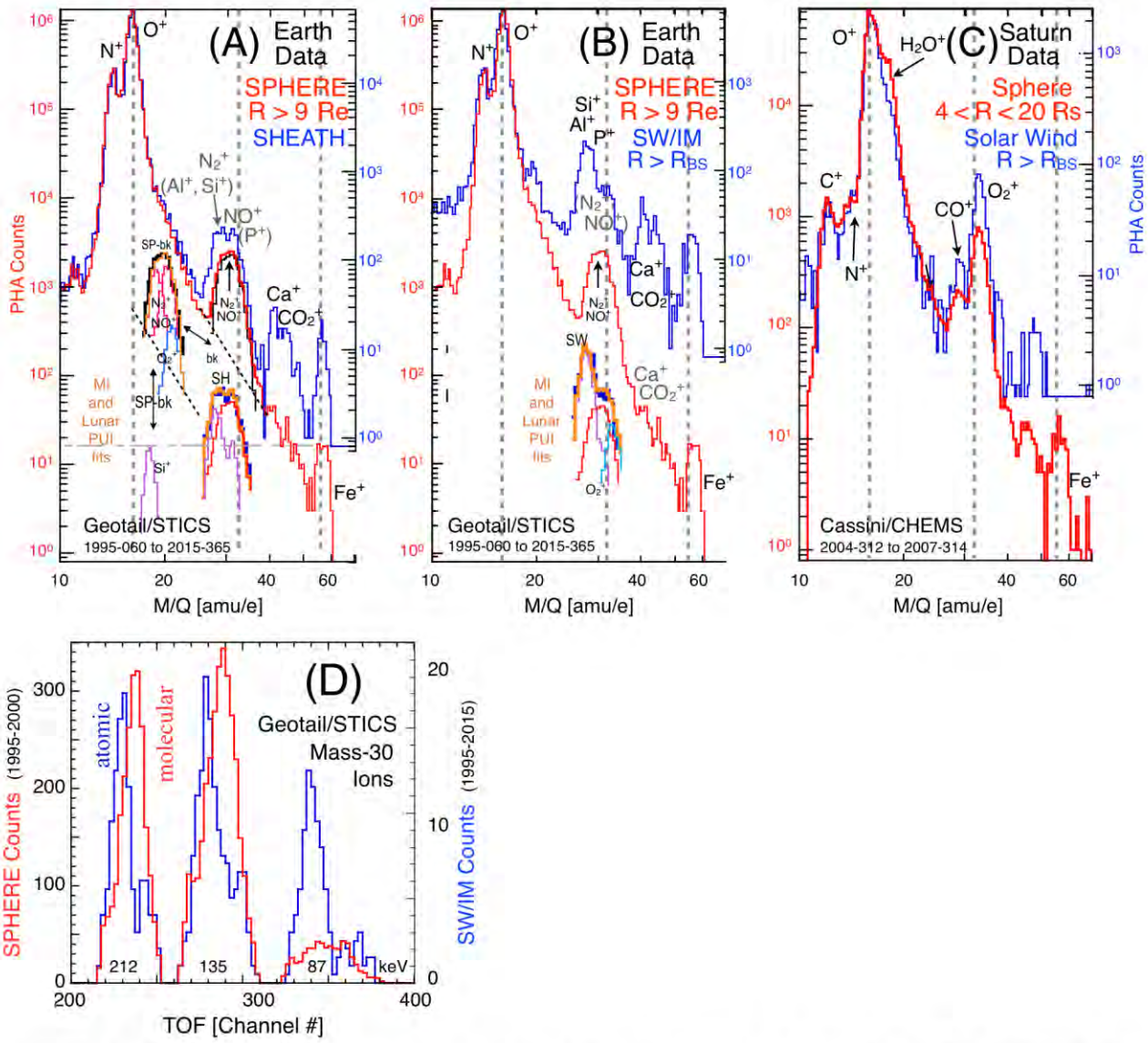

Figure 5. Long-term suprathermal (CHEMS, ~83-167 keV/e; STICS, ~87–212 keV/e) heavy ion composition measurements in near-Earth (A, B) and near-Saturn (C) plasma regimes are normalized to O^+ and compared directly. The vertical axes of SPHERE data (red left axis labels), SHEATH, and SW/IM data (blue right axis labels) are offset in order to compare selected species' importance relative to O^+. Shown are ~21 continuous years of Earth data and samples from ~3 years of select Solar Wind and contemporaneous Sphere intervals at Saturn. Note the distinct plasma regime labeling which differentiates the two planets' regimes in the text and highlights their different selection procedures. Vertical fiducial lines at 16, 32, and 56 amu/e are drawn to simplify visual comparison. At Earth, the Mass-30 SHEATH (A: blue) distribution is intermediate between that of the SPHERE (A, B: red) and SW/IM (B: blue). Floating insets (near bottom of A and B) show rough visual fits (orange) to the background (bk) subtracted SPHERE (SP-bk, black), SHEATH (SH), and SW/IM (SW, at distances R > R_{BS}, the distance to the bow shock) data. The fits use SPHERE MI (A: rose for N_2^+ and NO^+, light blue for O_2^+) and select distributions of lunar pickup ions, PUI, and/or, in the case of the SPHERE, ionospheric Si^+ (purple) at the Fe^+ level (long-dash line). Prominent lunar PUI species are identified. (D) In these instruments, dominant SPHERE molecular ion (MI) dissociation energy loss in the carbon foil result in slightly longer times-of-flight (TOF) with subsequently higher M/Q values than for the dominant SW/IM atomic ions of the same mass. See text.

similar as shown in Figures 5B and 5C; that is, at Earth, the ratios $N^+/O^+_{SPHERE} \approx N^+/O^+_{SHEATH} \approx N^+/O^+_{SW/IM}$, and at Saturn, $N^+/O^+_{Sphere} \approx N^+/O^+_{SolarWind}$ and $C^+/O^+_{Sphere} \approx C^+/O^+_{SolarWind}$. Saturn's Sheath data are excluded for brevity. Of note, H_2O^+ is the only ion in these comparisons whose PHA counts relative to O^+ can be seen to decrease significantly outside the magnetosphere rather than increase (this also likely occurs for OH^+, but OH^+ is masked by O^+ and H_2O^+). The Mass-30 data at Saturn are most informative because the escape of its MI into the Solar Wind appears to be uncomplicated (as shown above in Figures 4A and 4B), in that the escaped MI measurements in the Solar Wind are not masked by other Mass-30 ion species; the same MI species measured in the Sphere are those measured in the Solar Wind outside Saturn's bow shock. Mass-30 MIs are dominated by equal amounts of N_2^+ and NO^+ in Earth's magnetosphere and primarily by O_2^+ at Saturn, except at equinox (Christon et al., 2013), with overall average $MI/O^+ \sim 0.1\%$ at each. That normalization to O^+ does not introduce uncertainty in this presentation of the relative importance of escaped magnetospheric ions and lunar PUIs is supported by the similarity of Mass-16 atomic ions' relative intensities inside and outside these two magnetospheres noted above. (Interested readers can find Figure 5 data plotted separately with identical vertical axes in Figure S13 in the SI.) This similarity suggests that the magnetospheric and solar wind O^+ peaks are both dominated by magnetospheric ions at both planets and the relative proportions of the Mass-16 atomic ions remain similar, as might be anticipated for escape of atomic ions of similar mass and charge. The Figure 5 comparisons are constructed more for rough qualitative, not precise quantitative, comparisons as the amount of data at Earth is more comprehensive than at Saturn and, for this initial report we use fairly rudimentary fitting procedures. Mass-16 atomic ion ratios (N^+ to O^+ at Earth and C^+ and N^+ to O^+ at Saturn) are nearly identical in the different regimes, suggesting similar escape probabilities and solar wind interactions for the $^{16}M^+$ ions.

733 This does not imply that the magnetospheric escape mechanisms are identical, although they may
734 be, irrespective of the factor of ~10 difference in magnetospheric scales. For Mass-30 ions the
735 detection situation is different, being complicated at Earth by the presence of the lunar Mass-30
736 PUI. The nearly flat, double-peaked Mass-30 ion SHEATH PHA distribution (blue in 5A) is
737 intermediate between the rounder SPHERE PHA distribution (red in 5A and 5B), with mostly
738 N_2^+ and NO^+, and the distinctly different SW/IM PHA distribution (blue in 5B), dominated by
739 the narrow lunar PUI peak centered near ~28 amu/e. The flat-topped SHEATH feature has
740 significant contributions from lunar Si^+ and Al^+ PUI. We now determine rough estimates of the
741 composition of Earth's Mass-30 ion peaks.
742 [3.2.3] The insets in Figures 5A and 5B demonstrate the superposition of the model distributions
743 used to visually determine fits (orange in insets) approximating Earth's Mass-30 ion composition
744 in the different plasma regimes (separate larger plots with identical axes are in Figure S13 in the
745 SI). Fits are made to the background-subtracted SPHERE (black in inset SP-bk), the SHEATH
746 (blue in inset SH), and the SW/IM (blue in inset SW) Mass-30 ions. SP-bk is the only inset
747 plotted at the same count level as the data, first under the MI peak of the SPHERE data (red
748 curve) near ~32 amu/e, and then offset to the left near ~20 amu/e with its component fitting
749 curves; the SH inset is plotted lower than the SHEATH data by a factor of ~40, at the correct
750 M/Q location. Precise quantification of all ion components' contributions in this Figure has not
751 been attempted. For fitting shapes, we use (a) Earth's O^+ SHEATH and Saturn's O_2^+ Solar Wind
752 M/Q data peaks as representative atomic and molecular M/Q ion responses, respectively, to
753 model the different regimes' Mass-30 ion shapes, and (b) the SPHERE MI distribution to
754 represent escaped magnetospheric MI in the SHEATH and SW/IM, in which we did not attempt
755 to quantify relative magnetospheric N_2^+, NO^+, and O_2^+ numbers because the relative amounts of

lunar Al^+, Si^+, and P^+ is not necessarily well determined as is shown below. Assuming an exponential decrease, the diagonal dashed black line in Figure 5A estimates the SPHERE's O^+ high-M/Q tail underlying the SPHERE's Mass-30 peak. Subtracting this estimate from the SPHERE's Mass-30 peak creates the background-subtracted 'SP-bk' peak, the black histogram underlying the SPHERE Mass-30 peak and in the SP-bk inset. SP-bk is initially fit with only N_2^+ and NO^+ (both rose-colored) and then with O_2^+ (light-blue colored) fitting shapes, resulting in relative proportions ~43% N_2^+, ~46% NO^+, and ~10% O_2^+. Figures 5A and 5B reveal a distinct transition in Earth's Mass-30 ions from only ionospheric origin MI being apparent in the SPHERE, to mixed escaped magnetospheric MI (still dominant) and lunar atomic PUI in the SHEATH, and then to lunar PUI dominance in the SW/IM. The SHEATH and SW/IM insets use a reduced level escaped-SPHERE MI shape (red) for N_2^+ and NO^+, and different admixtures of Al^+, Si^+, and P^+, the relevant lunar PUI species (purple), in proportions that allow a reasonable overall fit to the Mass-30 data shapes. The relative importance of escaped magnetospheric MI and atomic lunar PUI reverses moving from the SHEATH (with ~64% escaped MI and ~36% PUI) into the SW/IM (with only ~17% escaped MI and ~83% PUI). Our fit to the SW/IM Mass-30 peak, demonstrates the necessity of using a relatively enhanced level of O_2^+ to approximate the SW/IM distribution's shape. Given that (1) we cannot uniquely identify peaks for the individual presumed ion species from ~27 to 33 amu/e, that is for Al^+, Si^+, N_2^+, NO^+ and/or P^+, and (2) the counting uncertainty at these count levels is not negligible, we can vary the relative lunar PUI and MI levels in the SW/IM widely. We found that the Mall et al. (1998) lunar PUI distribution fails to approximate the SW/IM data any better than other lunar PUI choices (see Figure S9 in the SI). Nevertheless, one fact which we will return to below is clear: a low level of PHA counts which we can explain using the model O_2^+ peak is clearly detected in the SW/IM

779 and which cannot be explained by any other currently identified ionospheric or lunar origin ion
780 species. Additionally, as shown in the SW inset in Figure 5B, the model O_2^+ count level relative
781 to N_2^+ and NO^+ is enhanced over its magnetospheric level (see also Figure S13 in the SI). Once
782 the MI are exposed to solar wind flows in the SHEATH and SW/IM, their relative impact
783 dissociation characteristics may become important. However, this study is not designed to
784 answer all questions related to these ions.
785 [3.2.4] Approximately equal ionospheric Si^+ and Fe^+ abundances result from meteoric ablation
786 (Vondrak et al., 2008; Plane, 2012) at Earth. As N_2^+ and NO^+ are commonly observed in
787 ionospheric outflow, Si^+, with a similar mass, should also be observed - possibly more often than
788 the observed Fe^+, attributed to the ionospheric Fe^+ derived from meteoroids. In the background-
789 subtracted SPHERE inset of panel 5A, SP-bk, we show the effect of including a Si^+ component
790 (purple) at the same level as the SPHERE Fe^+. This addition of Si^+ to the SP-bk fit produces a
791 negligible (0.7%) effect on the amount of N_2^+ needed for a good fit (we note further that the
792 addition of Si^+ degraded our subsequent total SP-bk fitting attempts). Since the O^+ background
793 subtraction results in larger uncertainties at the leading edge of the SP-bk data, ~28 amu/e, the
794 efficacy of adding Si^+ is very difficult to ascertain with the present data set. Si^+ is also a principal
795 observed lunar PUI (Hilchenbach et al., 1992; Mall et al., 1998). As anticipated from lunar
796 sample secondary ion mass spectrum, SIMS, studies (Elphic et al., 1991; Dukes and Baragiola,
797 2015), lunar PUI Fe^+ is expected to be present near the Moon at slightly lower levels than Si^+.
798 However, while lunar Si^+ PUIs are observed from the Moon to the magnetopause, no Fe^+ was
799 observed in a concerted campaign of near Moon PUI measurements with an instrument
800 functionally identical to ours (Mall et al., 1998; Kirsch et al., 1998).
801 [3.2.5] By normalizing the plasma regime data to their respective peak O^+ counts, we focus

802 attention on species' abundances relative to O^+. One consequence is that the 1-count levels in
803 Earth's SHEATH and SW/IM (blue curves) appear progressively higher compared to the
804 SPHERE (red curves) in panels 5A and 5B, reflecting a progressively significant decrease in O^+
805 counts with distance from the SPHERE. (Unnormalized versions of the Figure 5 panels are in
806 Figure S13 in the SI.) The same O^+ decrease is apparent for the Sphere (red curve) to Solar Wind
807 (blue curve) comparison at Saturn in panel 5C. That the ratios of N^+ and C^+ to O^+ at Saturn and
808 N^+ to O^+ at Earth remain approximately constant on escape suggests similar magnetospheric
809 escape processes and paths for these heavy atomic ions at both planets, but not necessarily
810 similar specific processes. Secondarily, the Mass-30 ion levels at both planets do not decrease as
811 much as the atomic ion levels suggesting fewer escape losses for the MI, although the presence
812 of lunar PUIs masking escaped MI at Earth complicates a simple, straightforward comparison.
813 Therefore, we address the simpler situation of Saturn's Mass-30 MI first.
814 [3.2.6] Figure 5C compares M/Q histograms of Saturn's Sphere and Solar Wind data. We
815 restricted our survey at Saturn to the Solar Wind regime because magnetopause and bow shock
816 motions appeared to render the Sheath data more difficult to isolate. Saturn's O_2^+ peaks in the
817 Sphere and Solar Wind show no significant difference in overall shape, whereas the Sphere CO^+
818 peak is not sufficiently higher than the local background count level to accurately determine a
819 possible change in shape, given the limited sample intervals currently available. As noted above,
820 Saturn's C^+ and N^+ ratios to O^+ in the Sphere and Solar Wind are comparable. Conversely, both
821 CO^+ and O_2^+ exhibit relative peak count level increases with respect to O^+. Larger CO^+ and O_2^+
822 gyroradii with respect to C^+, N^+, and O^+ are consistent with these MI having larger
823 diffusion/transport coefficients than the lower mass ions (e.g., Scholer et al., 2000), resulting in
824 less MI flux decrease relative to O^+. Probable CO_2^+ in Saturn's Sphere does not appear in the

825 Solar Wind. However, a higher M/Q species evident at ~45-50 amu/e in the Solar Wind, does not
826 appear to have a cognate in the Sphere. One might hypothesize that this ion species, close to the
827 mass of Ti^+ (M/Q = 48 amu/e), may be related to Phoebe and its pervasive ring (Verbischer et
828 al., 2009) and does not appear to enter Saturn's magnetosphere in a manner similar to the
829 apparent difficulty of lunar PUI near Earth to pervade Earth's magnetosphere. Note that Fe^+,
830 clearly observed in the Sphere is absent from the Solar Wind samples we collected for this study.
831 Given the size of Saturn's magnetosphere with respect to Earth's, Fe^+ might be less likely than
832 Mass-30 MIs, for example, expected to escape Saturn's magnetosphere than Earth's, on account
833 of it's larger gyroradius, although the opposite seems to be the case (see e.g., Mauk et al., 2019).
834 These preliminary observations suggest that further collection and research of solar wind and
835 magnetosheath ion data near Saturn is needed to determine: (a) extant ion species, and (b)
836 whether any Fe^+ escapes from Saturn's magnetosphere. One must remember that the dimensions
837 of Saturn's magnetosphere are approximately an order of magnitude larger than Earth's, that is, 1
838 Rs ~ 60,300 km, whereas 1 Re = 6378 km, and $R_{MP,Saturn}$ ~ 22 Rs, whereas $R_{MP,Earth}$ ~ 9-10 Re, so
839 The scale of Saturn's system may play a role in these observational results. We now address
840 Saturn's H_2O^+ component which shows a significant decrease relative to O^+ not seen for any
841 other ion at Saturn or Earth.
842 [3.2.7] We return to the apparent loss of H_2O^+ in the Solar Wind near Saturn. Figure 5C shows
843 that H_2O^+ is depleted with respect to O^+ in the Solar Wind compared to their relative values in
844 the Sphere, whereas CO^+ and O_2^+ are relatively enhanced in the Solar Wind. As this larger
845 relative deficit occurs only for H_2O^+, we interpreted this as likely resulting from stronger solar
846 wind impact dissociation for H_2O^+ than for either CO^+ or O_2^+, resulting from the lower H_2O^+
847 bond energy. (Please note that OH^+, also present in the W^+ peak, probably dissociates similarly,

as its bond energy is lower than that of H_2O^+; see Table S12 in the SI. However, in this work, we have not currently attempted to determine the OH^+ presence at Saturn, be it either inside or outside it's magnetosphere.) The Mass-16 atomic ion ratios in Saturn's Solar Wind data are similar those same ratios in Saturn's Sphere data in a manner similar to the situation for N^+ and O^+ at Earth (see Figures 5B and 5C), suggesting that the O^+ peak in the near-Saturn Solar Wind beyond Saturn's bow shock is likely dominated by Saturn's escaped O^+, not interplanetary PUI O^+. Note that all Sphere data from late-2004 through 2007 is shown in Figure 5C (the species ratios for only those Saturn Sphere orbits adjacent to the Solar Wind intervals of Figure 5C are very similar to the overall sum but have poorer statistics, see Figure S11). At and near Saturn, Cassini and CHEMS were fully operational with near-continuous data recording/transmission, whereas, during the cruise interval data transmission was at intermittent (see Section 2). Because of these different CHEMS operational situations, we have not yet attempted to directly compare these O^+ fluxes to nominal interplanetary data, given the possibly error-prone process of estimating the interplanetary O^+ fluxes during Cassini's cruise to Saturn which makes a reliable comparison difficult. Clearly, the magnetospheric escape processes at Saturn may be complicated and a more detailed analysis should be pursued in the future when additional Cassini bow shock and magnetopause crossing identifications near Saturn have been determined and verified. Nevertheless, the initial bow shock and magnetopause crossing identifications at Saturn have been critical in enabling this analysis, and our considerations and interpretation of the Mass-30 ions' identity outside the planets' magnetospheres. The data have demonstrated that: (A) the peak of O_2^+ M/Q PHA distributions are clearly not centered at the MI's atomic mass, but displaced to M/Q > 32 amu/e both inside and outside Saturn's magnetosphere, and (B) the overall shape of the MI PHA Mass distributions are rather similar inside and outside Saturn's

magnetosphere, very different observational environments.

[3.2.8] Figure 5D shows the clear TOF differences between Mass-30 ions in Earth's SPHERE and SW/IM regimes (collected over ~6 years and ~21 years, respectively) at three widely spaced electrostatic deflection step voltages. The TOFs of SPHERE MI data (red), mostly N_2^+ and NO^+, are generally longer than the TOFs of SW/IM data (blue), where there is a significant contribution from atomic Si^+ lunar PUIs. As explained above in Section 2, MIs travel slower than the atomic ions on account of losing additional energy in the carbon foil. These data demonstrate the significant differences between atomic and molecular ion responses and will be useful in separating the lunar and terrestrial origin ions in subsequent, dedicated studies.

Geomagnetic and Solar Activity Dependence at Earth

[3.3.0] Geomagnetic Activity. Figure 6 shows the overall geomagnetic and solar activity dependence of long-term average 3-hr PHA count sums of the MI channels, N^+, O^+, and Fe^+. These 3-hr PHA count averages are rough guides to different species' occurrence rates, likely more accurate at low levels and underestimates of actual species rates at their highest levels. However, they provide guidance as to species' flux dependence on geomagnetic and solar activity. Data collected over all regimes are plotted versus Kp in Figures (6A) and F10.7 in (6C) with $^{28}Mq^+$ and $^{30}Mq^+$ ions separated. Kp averages are taken over the -, o, + range of integer Kp values, where, for example, Kp = 3 in the plot includes Kp = 3-, 3o, and 3+. Parallel heavy dashed lines in (6A) and (6C) are drawn parallel to the approximate N^+ and O^+ slopes at high Kp and at F10.7 > 100 10^{22} W/m^2/Hz, respectively. These lines represent the nominal moderate-to-high activity ionospheric outflow rate increase of dominant heavy ionospheric atomic ions with respect to Kp and F10.7, that is, the terminal outflow rate. They are meant to guide the eye and to highlight similarities and differences of ion group geomagnetic and solar activity dependences.

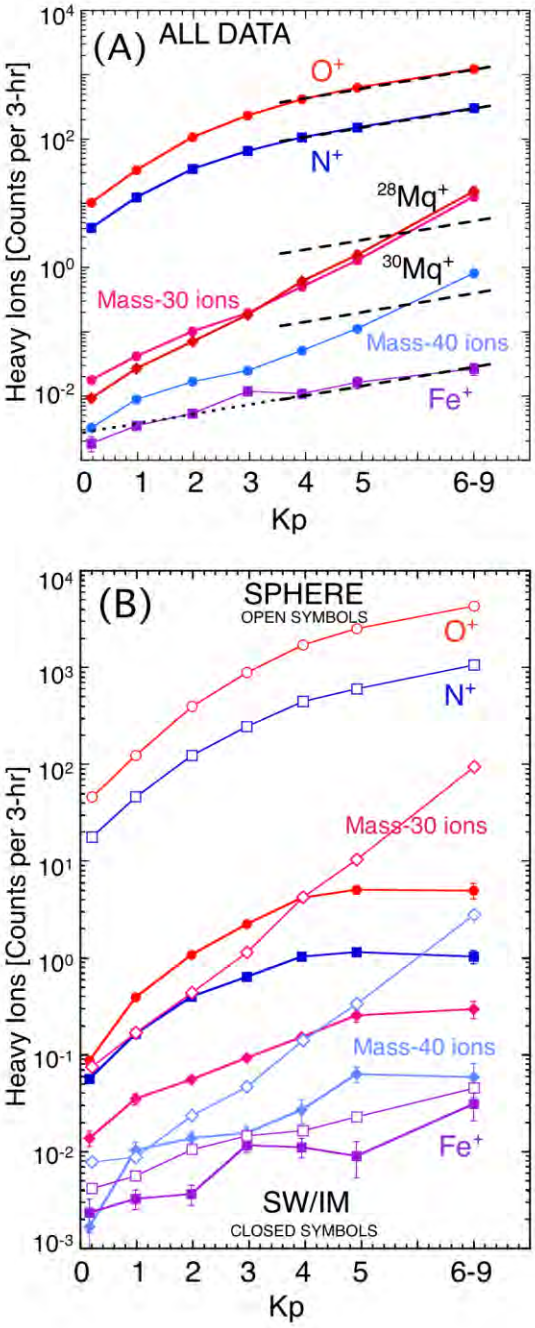

Figure 6. Averages of suprathermal (~87–212 keV/e) N^+, O^+, Fe^+, Mass-30 ions ($^{28}Mq^+$ and $^{30}Mq^+$) and Mass-40 ions 3-hr PHA count sums are plotted versus interval averages of (A, B) Kp and (C) $F_{10.7}$ values from 1995 to 2015. In (A) and (B), all data are shown. In (B) the data are from two plasma regimes, SPHERE (open symbols) and SW/IM (closed symbols). Uncertainties, standard error of the mean, are generally smaller than the point size. Horizontal bars in (C) indicate $F_{10.7}$ ranges. Kp averages are over the -, o, + range of the Kp index integer values. Dashed and dotted lines in (A and C) are intended to guide the eye in comparing the heavier ions to N^+ and O^+ (see text). The dotted extension of the Fe^+ line in (A) highlights the outlying Kp = 3 average which is also apparent in the SW/IM data.

Correlations of the ion groups with Kp are positive overall. At low Kp, Fe^+ increases with Kp less rapidly than any of the other species' average rates, all of which are similar. The O^+ and N^+ outflow Kp-rates relax to that of Fe^+ at high Kp. The overall Fe^+ Kp-rate increase changes the least of all species, being roughly characterized overall by the terminal outflow rate. The Mass-30 and Mass-40 ions' Kp-rates of increase never relax to the average terminal outflow rate of O^+, N^+, and Fe^+, instead they increase significantly in the highest Kp range. The overall Mass-40 ion Kp-rate increase accelerates more rapidly than any other species at low Kp, relaxes somewhat at mid-Kp, and then accelerates to be the fastest outflow Kp-rate at Kp $\geq$ 5. Data collected separately in the SPHERE and SW/IM regimes are plotted as open (closed) symbols versus Kp in Figure 6B, where we note that both Mass-40 ions and Fe^+ may be insufficiently sampled in the SW/IM. SPHERE and SW/IM intervals dominate the magnetospheric ion data set because it is there, in the magnetosphere and the solar wind, respectively, where fluxes are the highest in the first case and where the satellite spends the most time in the second, respectively. In Figure 6B: (a) monotonic Kp-rate increases are evident for all species in the SPHERE at all Kp values, where the Mass-30 and Mass-40 ion increases are the strongest and Fe^+ is the weakest; (b) all SW/IM Kp-rate profiles except that of Fe^+ are generally similar, relaxing, even decreasing slightly in two cases, at high Kp; (c) Fe^+ experiences a large increase at Kp = 3 in the SW/IM, but then decreases until Kp = 5, above which it resumes increasing. The continual strong rate of increased Mass-30 and Mass-40 ion flux in the SPHERE is uniquely different from that of O^+, N^+, and Fe^+, and is consistent with the findings of Lennartsson et al. (2000) and should be studied in the future.

[3.3.1] Figure 6C shows that while O^+ and N^+ F10.7 dependences are similar, only O^+ increases monotonically with $F_{10.7}$ unambiguously. N^+ is more similar to O^+ than to the heavier ions,

although its mid-$F_{10.7}$ points barely increase. In contrast, the Fe^+ dependence on F10.7 is more similar to that of Mass-30 and Mass-40 ions than to N^+ or O^+, even though the Fe^+ and N^+ dependence from low to mid F10.7 values is very similar. From ($80 \leq F_{10.7} \leq 120$) 10^{22} W/m^2/Hz, all species $F_{10.7}$-rates appear to increase, although each with individual characteristics. O^+ and Mass-30 ions increase more strongly at low $F_{10.7}$, N^+ and Fe^+ more weakly. Mass-30 and Mass-40 ion $F_{10.7}$-rates decrease noticeably at (120 to 170) 10^{22} W/m^2/Hz. At ~(120 to 220) 10^{22} W/m^2/Hz, mid-$F_{10.7}$ values, Mass-30, Mass-40, and Fe^+ ion $F_{10.7}$-rates all decline, and then increase significantly at the highest $F_{10.7}$ value. The following discussion of lunar ion fluxes should increase our understanding of the differences. Below, we briefly introduce, define, and characterize relevant information we have found in our data regarding the lunar PUI background in the Mass-30 ion data before characterizing MI variations identifiable in the Mass-30 and Mass-40 ion channels near Earth.

4. Lunar PUI fluxes near Earth

[4.0] Lunar PUI separation/identification. In Section 3 we demonstrated that the Mass-30 $^{28}Mq^+$ and $^{30}Mq^+$ ion channels both contain significant atomic lunar PUI components. The map of Geotail orbit plasma regimes in Figure 7A also shows the Earth (blue dot at center), the average locations of the SPHERE, SHEATH, and SW/IM plasma regimes (as described in Section 2.0.1), the Moon's orbital variation range, and a number of Geotail R < ~30 Re orbit segments for an overview perspective. Two spatial features/conditions are important for considering possible lunar influence: (1) the Moon's Lunar orbital Local Time (or LLT) "Sector 3" range, $10 \leq LLT \leq$ 14 hours (1/6 of the Moon's full orbit), which includes lunar orbit locations where the Moon is more or less "directly" sunward of the Earth and the Geotail orbits to which it can most readily contribute PUIs via convection; and (2) the heavy ion Lunar Wake, drawn here with a broad, ~25

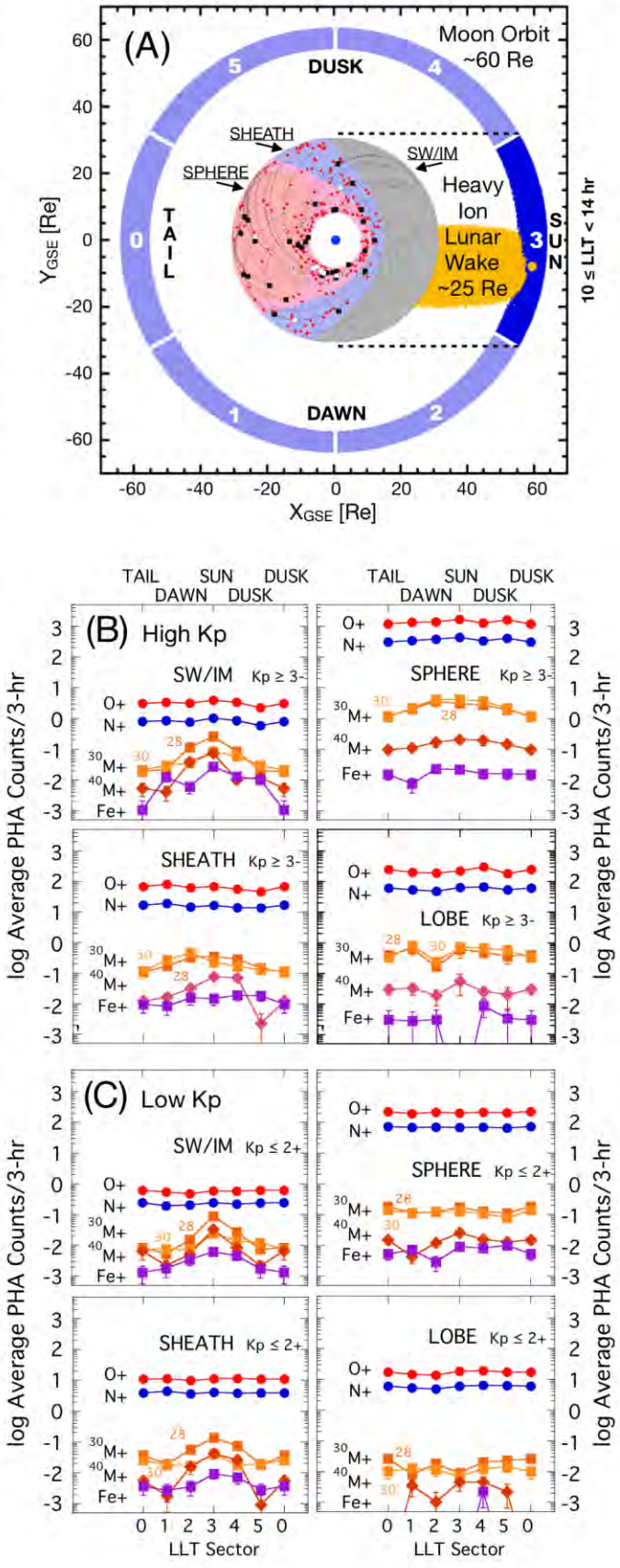

Figure 7. (A) A sketch of the Earth (blue dot at center), the Moon's orbital range, and Geotail orbital range, ~9 < R < 35 Re. Two spatial criteria for considering possible lunar pickup ion influence in Geotail/STICS suprathermal (~87–212 keV/e) ion measurements are the lunar local time (LLT) and the 'Lunar Wake'. LLT marks the orbital location of the Moon with respect to the Earth-Sun line. At 10 ≤ LLT ≤ 13 hours, LLT-sector 3, the Moon is sunward of Geotail's nominal orbital X_{GSE} -Y_{GSE} range. From favorable orbit locations ~60 Re sunward of Earth, the Moon can convectively contribute pickup ions to our SW/IM data near Earth. The 'Lunar Wake', drawn here with a ~25 Re width to include heavy ion (e.g., CO_2^+ or Fe^+) gyroradii in the nominal (~7-9 nT) interplanetary magnetic field at 1 AU, is probably always present, varying in strength, and is likely important in supplying lunar PUI to near-Earth locations. Selected segments of Geotail orbits, the dotted traces near Earth, terminate when an Fe^+ was observed during low to moderate solar/geomagnetic conditions. White (black) squares indicate Fe^+ observations obtained when the Moon was (not) in LLT-sector 3. Red dots show other measured Fe^+ data. Arrows point from underlined labels to three near-Earth plasma regimes. The LOBE (not shown) overlies the SPHERE. (B,C) Four panels at (B) High-Kp and (C) Low-Kp levels enable investigation of some possible observable effects of lunar PUIs intermixed with Earth's escaped ionospheric ions which are related to the Moon's orbital location. The effects differ between observations made in the four near-Earth plasma regimes used in this study.

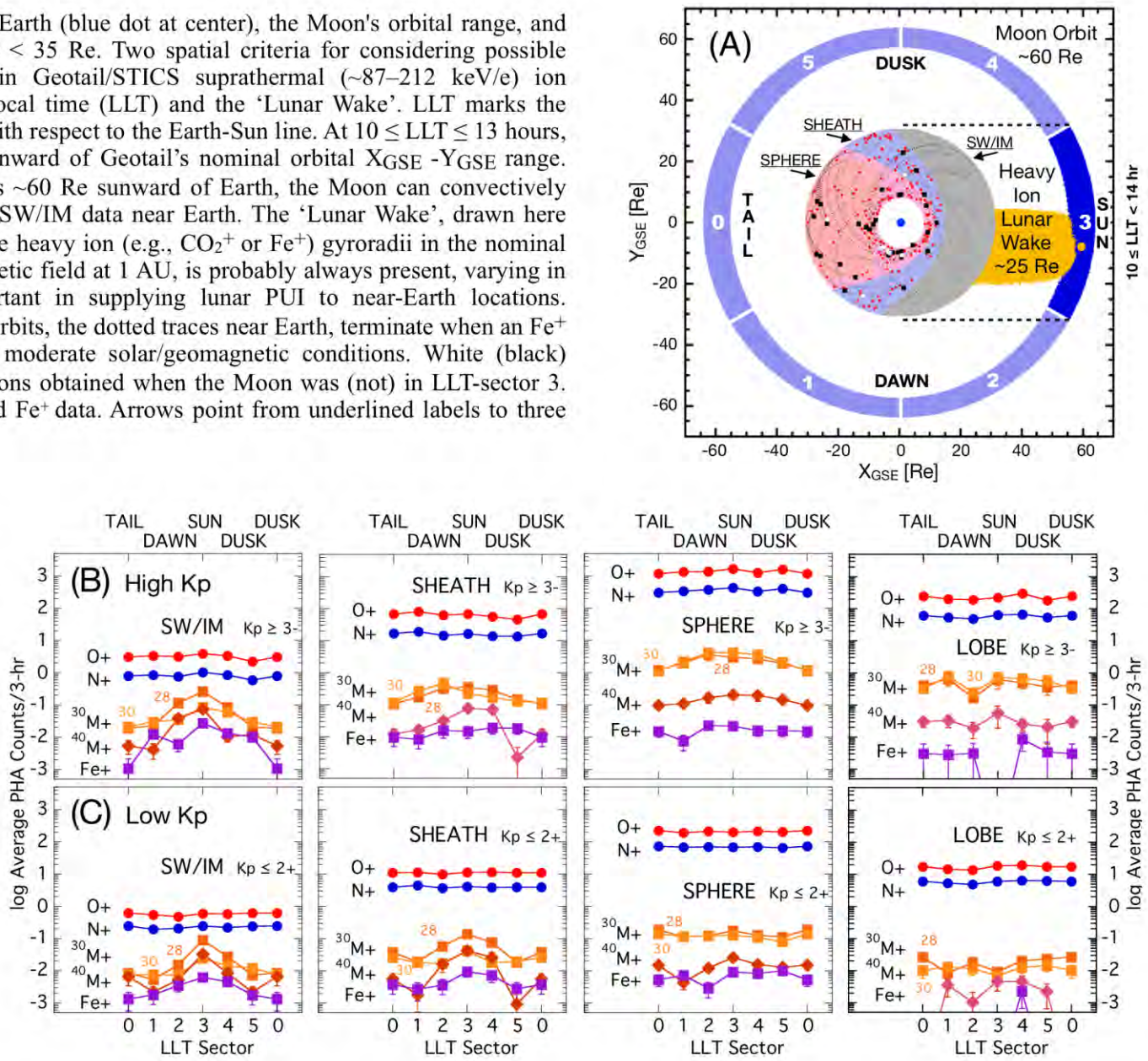

Figure 7. (A) A sketch of the Earth (blue dot at center), the Moon's orbital range, and Geotail orbital range, ~9 < R < 35 Re. Two spatial criteria for considering possible lunar pickup ion influence in Geotail/STICS suprathermal (~87–212 keV/e) ion measurements are the lunar local time (LLT) and the 'Lunar Wake'. LLT marks the orbital location of the Moon with respect to the Earth-Sun line. At 10 ≤ LLT ≤ 13 hours, LLT-sector 3, the Moon is sunward of Geotail's nominal orbital X_{GSE} -Y_{GSE} range. From favorable orbit locations ~60 Re sunward of Earth, the Moon can convectively contribute pickup ions to our SW/IM data near Earth. The 'Lunar Wake', drawn here with a ~25 Re width to include heavy ion (e.g., CO_2^+ or Fe^+) gyroradii in the nominal (~7-9 nT) interplanetary magnetic field at 1 AU, is probably always present, varying in strength, and is likely important in supplying lunar PUI to near-Earth locations. Selected segments of Geotail orbits, the dotted traces near Earth, terminate when an Fe^+ was observed during low to moderate solar/geomagnetic conditions. White (black) squares indicate Fe^+ observations obtained when the Moon was (not) in LLT-sector 3. Red dots show other measured Fe^+ data. Arrows point from underlined labels to three near-Earth plasma regimes. The LOBE (not shown) overlies the SPHERE. (B,C) Four panels at (B) High-Kp and (C) Low-Kp levels enable investigation of some possible observable effects of lunar PUIs intermixed with Earth's escaped ionospheric ions which are related to the Moon's orbital location. The effects differ between observations made in the four near-Earth plasma regimes used in this study.

945
946 Re, width to include heavy ions with masses up to SiO^+, CO_2^+, or Fe^+, for example, suprathermal
947 energy heavy ions with large gyroradii in the nominal (~7-9 nT) interplanetary magnetic field at
948 ~1 AU. In the map near Earth, dotted traces and large black and white squares indicate 37
949 Geotail orbit segments that are ≥24 hours long and end at the Fe^+ measurement (squares). The
950 orbit segments include 42 Fe^+ PHA measurements in the SPHERE (33 black) and in the
951 SHEATH (9 white) obtained during low to moderate geomagnetic and solar activity conditions.
952 A PHA color spectrogram for the data from these orbits is shown in Figure S5 in the SI. The
953 orbit intervals were selected by Christon et al. (2017) for their characteristic of having a low
954 presence of PHA counts in the M/Q range of Mass-30 ions (which may include Al^+, Si^+, N_2^+,
955 NO^+, O_2^+, P^+, and Fe^{+2}), specifically to exclude possible Fe^{+2} charge-exchanged from high-
956 charge-state solar wind iron, $Fe^{+7:+14}$, prior to the measurement of a Fe^+ in the SPHERE or
957 SHEATH. Use of this observation interval selection scheme near Earth under low Mass-30 ion
958 (e.g., Si^+) conditions is germane to arguments regarding lunar PUIs because various laboratory
959 studies have suggested that Fe^+ is an expected product of lunar soil irradiation by typical solar
960 wind energy ions through secondary ion mass spectrometry (e.g., Elphic et al.,1991; Dukes and
961 Baragiola, 2015). Lunar PUI Fe^+ has been anticipated in lunar ion observations and modeling
962 (e.g., Yokota and Saito, 2005; Sarantos et al., 2012; Poppe et al., 2016) but lunar PUI Fe^+ has not
963 yet been observed near the Moon with instruments that are designed to measure Fe^+ (e.g., Mall et
964 al., 1998; Kirsch et al., 1998; Yokota and Saito, 2005; Sarantos et al., 2012; Poppe et al., 2016).
965 Geotail/STICS has measured Fe^+ near Earth. The selected orbit segments include times when the
966 Mass-30 ion counts near Fe^{+2} (M/Q ~ 28 amu/e, M ~50-70 amu) were consistent with the
967 surrounding, extant, low background-count levels representative of relatively low-to-moderate
968 geomagnetic and solar activity intervals near-Earth (Christon et al., 2017). The 9 large white

969 squares here, 7 in the SPHERE and 2 in the SHEATH, are ~21% of the 42-count Fe^+-sample and
970 represent Fe^+ observations made at times when the Moon was sunward of Earth in the ~10-13
971 hour LLT range (LLT Sector 3). The large black squares represent Fe^+ observations from the
972 other select orbit segments when the Moon was not sunward of Earth and it was in locations
973 around the Earth from which one would not necessarily expect to observe lunar PUI transported
974 via convective processes to the SPHERE. (The red dots show the other Fe^+ measurement
975 locations.) The 9 Fe^+ counts measured when the Moon was in LLT Sector 3, as a portion of the
976 42 total PHA events, are not significantly different from the overall average seven total Fe^+
977 counts per LLT Sector, consistent with there being no elevated lunar PUI signal in LLT Sector 3.
978 This argues that the Fe^+ observed in and near the SPHERE at low to moderate geomagnetic
979 activity levels is unlikely to be of lunar origin at times when few Mass-30 ions of either
980 ionospheric or lunar origin are measured in the SPHERE. Further, PHA data from these orbit
981 segments (shown in Figure S5 in the SI, and below) argue that the Fe^+, combined with the Mass-
982 30 ions' M/Q distribution from these orbits, is more consistent with an ionospheric, rather than
983 lunar origin. This does not imply that lunar PUI Fe^+ may not be produced during intervals of
984 more intense geomagnetic and/or solar activity. As we comment below, lunar PUIs may be
985 present in the SPHERE during disturbed conditions, but currently we have not yet characterized
986 their proportion or occurrence likelihood.
987 [4.0.1] Ion Flux Variations Related to Moon Location. Figures 7B and 7C shows average N^+, O^+,
988 Fe^+, Mass-30 ($^{30}M^+$) and Mass-40 ($^{40}M^+$) ion data collected during high-Kp (Kp ≥ 3-) and low-
989 Kp (Kp ≥ 2+) intervals, respectively, in each of the plasma regimes for times when the Moon
990 was in each LLT Sector, irrespective of solar activity level. The highest Kp intervals (Kp ≥ 8o)
991 were excluded from these initial averages because of spatial sampling effects. In the following,

for a specific ion channel, we consider a "signal" to be a LLT Sector PHA count average higher than the channel's overall average having a statistically significant difference from the other averages in that species' Kp and plasma regime selection grouping, such as the $^{30}M^{+}$ and $^{40}M^{+}$ ions in the high-Kp and low-Kp SW/IM panels. The analysis is designed so that a significant lunar PUI signal should result in an LLT distribution that peaks at LLT Sector 3, especially in the SW/IM and SHEATH data. A similar result should be evident for the heavier ions as a result of the solar wind convection anisotropy, although a convective signature would likely dissipate in SW/IM and the SHEATH Sectors farther from Sector 3 and disappear while the spacecraft was in the SPHERE and the LOBE. One would anticipate a strong PUI signal for $^{40}M^{+}$ ions which we presume are dominated by lunar PUI in SW/IM and SHEATH data, but obscured in the SPHERE by backgrounds (see Figure 5 and Figure S3 in the SI). A lunar PUI signal should add to the convective anisotropy peak in all LLT sectors, but primarily in the sunward LLT Sector 3. We take Figure 5's N^{+} and O^{+} distributions in the SW/IM and SHEATH to represent the "lighter-ion" escaped, or escaping, magnetospheric ion signal; $^{40}M^{+}$ in the SW/IM and SHEATH to represent a lunar PUI signal; and Fe+ in the SHEATH to represent a convective signal. Please note that distinct, single-LLT-Sector variations, such as a discontinuous large increase or decrease in a single LLT sector, may result from either (a) unintended inclusion or exclusion of solar related particle events (flares, shocks, and/or CMEs) inadvertently missed in the data inspection/inclusion procedures, or (b) low counting statistics. Several overall aspects shown in the panels are: (a) $^{16}M^{+}$ species do not exhibit any outstanding LLT-Sector peaks in any regime and no statistically significant differences throughout, although, the LLT-Sector 3 average is just significantly different with respect to the LLT-Sector 2 average at low Kp and nearly-so at high Kp; (b) $^{30}M^{+}$ and $^{40}M^{+}$ ions have highly-statistically-significant peaks centered on LLT-Sector 3

in the SW/IM and SHEATH which are more pronounced than any signal possibly present for $^{16}M^+$ ions and Fe^+; (c) SW/IM $^{30}M^+$ and $^{40}M^+$ ions likely have strong lunar PUI contributions, as evidenced by their strong, broad peaks centered on LLT-Sector 3 in the SW/IM at high Kp and for $^{40}M^+$ ions in the SHEATH, although, see (d); (d) at high Kp MI^+ likely dominate SHEATH $^{30}M^+$ ions as suggested by the somewhat uniform overall distribution (more comparable to the $^{16}M^+$ ion data than at low Kp), whereas lunar PUI likely dominate SHEATH $^{30}M^+$ ions at low Kp as indicated by the prominent LLT-Sector 3 peak; (e) the $^{40}M^+$ ions in the SPHERE appear to be dominated by random background counts, hence, the uniform distribution; (f) Fe^+, for which LLT-Sector 3 is sometimes stronger and LLT-Sector 0 is sometimes weaker in the various plasma regimes, seems generally consistent with convective anisotropies, not a lunar PUI source; (g) for high-Kp averages, Fe^+ may have a lunar PUI component in SW/IM data on account of the statistical significance of LLT-Sector 3 which is higher than the next three highest Fe^+ high-Kp averages, the difference is significant for only LLT-Sector 5; (h) Fe^+ appears to have a strong convective anisotropy in the low-Kp SW/IM averages; and, (i) in the LOBE, no species shows a large overall variation and very little Fe^+ is observed. Additionally, comparison of the SW/IM Fe^+ LLT-Sector 3 average to the other Fe^+ LLT-Sector averages in the various regimes (see Table S6 in the SI) suggests that despite similar enhanced levels at and near LLT-Sector 3, the Fe^+ count differences are much less extreme than those of $^{30}M^+$ and/or $^{40}M^+$ ions, tending possibly toward the uniformity characteristics of $^{16}M^+$ ions than lunar PUI. This brief assessment of the ion channels suggests for SW/IM: a clear lunar PUI/convective signal in $^{30}M^+$ and $^{40}M^+$; possible convective signals in $^{16}M^+$; a broad convective and possible lunar PUI signal in Fe^+ at high Kp; SHEATH: clear $^{40}M^+$ and probable/possible $^{40}M^+$ and Fe^+ convective and/or lunar PUI signal; SPHERE: broad, higher $^{30}M^+$ sunward sector levels at high Kp suggest lunar PUI leakage

into the SPHERE; background dominated $^{40}M^+$ shows a possible lunar PUI signal; SPHERE Fe^+ is nominally as uniform as SPHERE $^{16}M^+$, with no statistically significant inter-average differences; and LOBE: statistically significant $^{30}M^+$ and $^{40}M^+$ and possible Fe^+ PUI signals in LLT-sector 5.

[4.1] Mixing of MI and PUI near Earth. Separation of the superposed $^{28}Ma^+$ ions' ionospheric N_2^+ and lunar PUIs dominated by Si^+, in the near-Earth SW/IM's Mass-30 PHA distributions is demonstrated in Figure 8 using two different methods. The solid curves in Figure 8A are smoothed fits to the near Earth SW/IM plasma regime ion data from Figure 4D. O^+ and N^+ are again shown for comparison. As noted above in the discussion of Figure 4, Earth's $^{28}Ma^+$ and $^{30}Ma^+$ SW/IM data are more complex than, and not similar to, the comparable $^{28}Ma^+$ and $^{30}Ma^+$ SPHERE data as a result of the presence of lunar PUIs. For example, in addition to ionospheric N_2^+ and NO^+, the $^{28}Ma^+$ and $^{30}Ma^+$ channels will also contain some lunar Si^+, Al^+, and P^+. As a first step, we first scale the $^{30}Ma^+$ distribution shape upward by a factor of 1.55 (the purple dashed curve) in order to extract the most important differences between the $^{30}Ma^+$ and $^{28}Ma^+$ distributions. At this upward-scaled level, the differences between the lower portions of the scaled $^{30}Ma^+$ curve and the $^{28}Ma^+$ curve (those segments below the gray horizontal area) are statistically negligible, but now comparable. Subtracting the scaled $^{30}Ma^+$ curve (purple dashed curve) from the $^{28}Ma^+$ data (orange solid curve) leads to an initial crude estimate of $^{28}Ma^+$ lunar PUIs, the black dashed curve labeled "Estimate of lunar PUI" in panel 8A. The shape of the Estimate's peak is very similar to that of the O^+ peak, as shown by the shifted O^+ peak (red dashed curve) centered at the Estimate's peak. But for a distinct shoulder at ~15-24 amu, the curves' similarities argue that the SW/IM $^{28}Ma^+$ ions are likely dominated by a single atomic ion

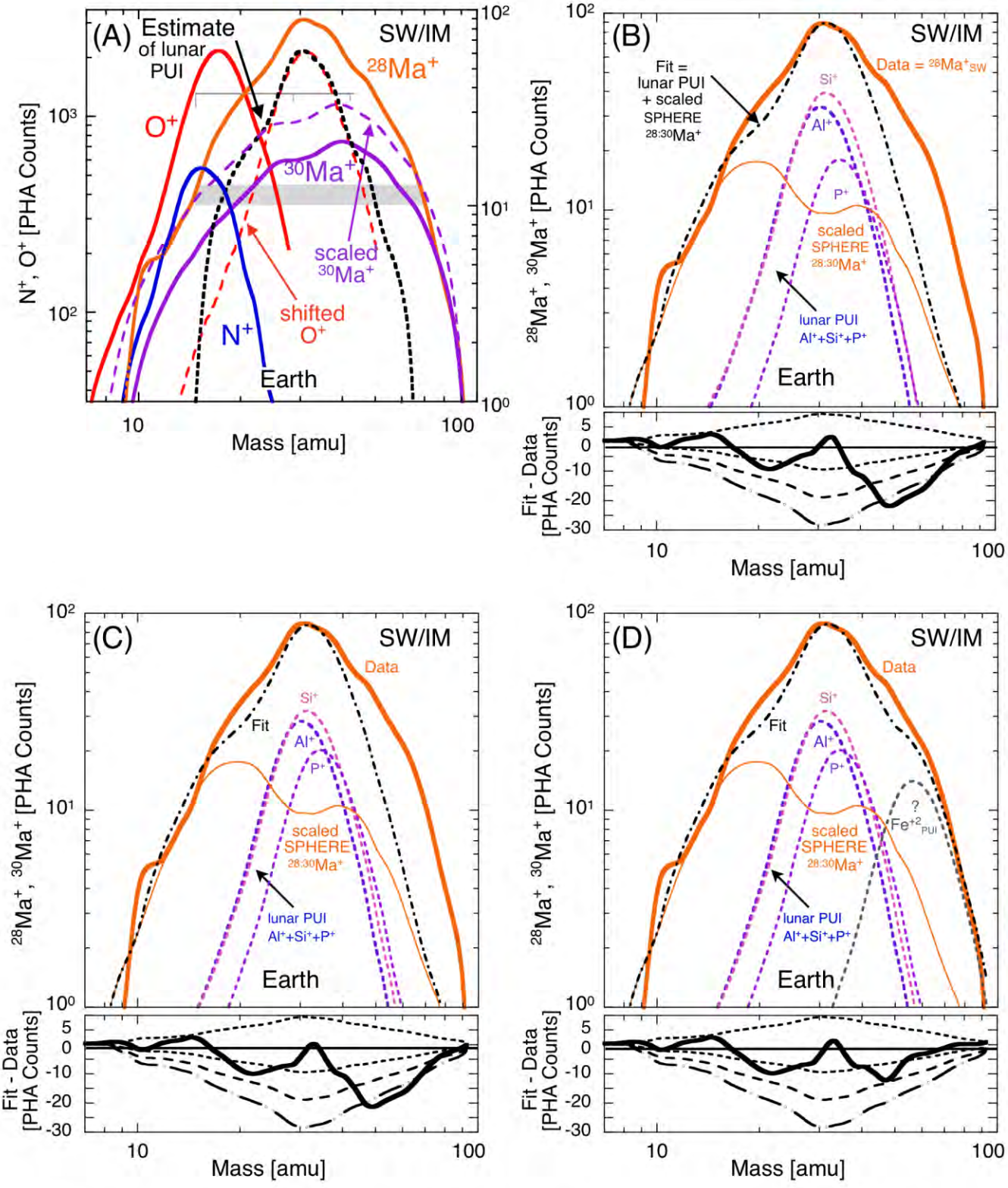

Figure 8. The superposition of the PHA distributions of lunar pickup ions, PUI, mostly Si^+, and ionospheric N_2^+ in the near-Earth solar wind, SW/IM, PHA distributions is investigated using two different comparisons. (A) The suprathermal (~87–212 keV/e) ion data are all from the SW/IM plasma regime near Earth. Solid curves are smoothed, interpolated fits to the data in Figure 3D. The shape of

with a shape similar to that of O^+. This result is encouraging, because Si^+ dominates the lunar Mass-30 PUIs measured by Hilchenbach et al. (1992) and Mall et al. (1998), measurements we will address in the next section.

[4.1.1] A more detailed investigation of the $^{28}Ma^+$ peak is demonstrated in Figures 8B, 8C, and 8D, in which model atomic ion PHA distributions are used to fit the observed $^{28}Ma^+$ data (orange solid curve). First, we determined that the atomic ion Mass distributions of SW/IM O^+ and solar wind $Fe^{+5:+11}$ Mass distributions are similar, but not identical (see Figure S7 in the SI), that is, the $Fe^{+5:+11}$ ions' shape is slightly narrower. However, given that the shape of the lunar PUI component in Figure 8A was very similar to that of O^+ and there is presently no straightforward method to determine the shape of an individual Mass-30 ion's Mass distribution, we simply use the O^+ shape as our model atomic ion shape in the following analysis. We first use this model shape to visually determine the contributions from lunar PUI Al^+, Si^+, and P^+ at levels consistent with the proportions of relevant lunar PUIs from Mall et al. (1998) combined with a scaled representation of an admixture of MI-dominated $^{28}Ma^+$ and $^{30}Ma^+$ SPHERE data assuming escaped magnetospheric MI populations do not change significantly during the escape process (consistent with the distributions of escaped Saturn MI in Figure 4). The heavy dot-dash curves labeled “Fit” in Figures 8B, 8C, and 8D approximate, as best we can, the expected shape of our $^{28}Ma^+$ SW/IM data. (Please note that we use the capitalized word Fit in this paragraph to refer to these “Fit” curves displayed in Figure 8.) The mixture of Mass-30 atomic ion species in lunar PUI from Mall et al. (1998) data shown in Figure 8B is $Al^+ : Si^+ : P^+ = 0.72 \pm 0.09 : 1.00 \pm 0.12 : 0.51 \pm 0.07$ (106 : 148 : 76 PHA counts). These ratios are derived from our assessment of their Figure 1 PHA histograms (shown below and in Figure S10). After subtracting this mixture of ionospheric MI and lunar PUI, the residual (the heavy solid black curve in Figure 8B, lower

1085 panel) demonstrates that we can account for most of the observed SW/IM $^{28}Ma^{+}$ shape within
1086 one standard deviation of the Data curve (1, 2, and 3 standard deviations shown as dashed curves
1087 in the bottom panels of Figures 8B, 8C, and 8D). However, two ranges of wider Fit-Data
1088 mismatch remain: one at ~15-24 amu and the other at ~38-100 amu. Presuming that the lunar
1089 PUI composition might change over different phases of a solar activity cycle and the Mall et al.
1090 data were obtained near the minimum solar activity of 1994-1998, we then sought a different,
1091 more optimal combination of lunar PUIs required to fit our Data (obtained over two full solar
1092 cycles) which is shown the PUIs incorporated into the Fit in Figure 8C. The PUI ratios for this
1093 optimal PUI Fit are: $Al^{+} : Si^{+} : P^{+} = 0.89 : 1.00 : 0.63$. The Data-Fit mismatch below ~40 amu is
1094 slightly better, but the significant Data-Fit mismatch peaking at M ≈ 50 amu remains and does
1095 not appear to be explained by our current estimate of ion composition candidates. Any solution
1096 to the mismatch must have the M/Q of ~28 amu/e and a Mass between ~50 to ~60 amu. The only
1097 reasonable physical explanation we arrived at is that we may be measuring a population of
1098 doubly charged iron, Fe^{+2}, which has M = 56 amu and M/Q = 28 amu/e. Fe^{+2} has been identified
1099 at lower energies in coronal mass ejection solar wind flows (Gilbert et al., 2012) and as a
1100 possible interstellar PUI generated by and transported with the solar wind (Taut et al., 2015).
1101 Recent analysis also revealed that Fe^{+2} is a component of nano-dust particles in space-weathered
1102 lunar soils (Thompson et al., 2016). Therefore, we added a Fe^{+2} model PUI component to our
1103 admixture and found that the overall agreement with data improved as shown in Figure 8D. The
1104 relative Mass-30 PUI ratios with this addition to our optimal PUI Fit is: $Al^{+} : Si^{+} : P^{+} : Fe^{+2} = 0.89 :$
1105 $1.00 : 0.63 : 0.44$. Next, we briefly examine Mass-30 ion upstream measurements, that is, sunward
1106 of the foreshock region of the SW/IM data, a regime where bow-shock-related effects might be
1107 less evident.

1108 [4.2] Earth's foreshock region. Figure 9A demonstrates that, even in the presence of lunar PUI in
1109 the same mass range, small amounts of the three ionospheric molecular ions, N_2^+, NO^+, and O_2^+
1110 are likely visible at $X_{GSE} \geq 20$ Re out to R ~ 30 Re, the furthest sunward locations sampled by
1111 Geotail. These ion data are obtained at ≥ 5 Re sunward of the nominal bow shock subsolar
1112 distance - locations nominally sunward of direct bow shock the bow shock interactions with the
1113 solar wind or lunar PUI, even though some backscattered ions and upstream wave and field
1114 effects are probably present (Mitchell et al., 1983; Kis et al., 2004). Over 40% of all SW/IM
1115 Mass-30 observations are obtained sunward of $X_{GSM} = 20$ Re where Geotail dwells longest at its
1116 ~30 Re apogee, so this selection at ~5-15 Re upstream of the average bow shock location can
1117 reveal significant information about the solar wind as minimally affected by upstream bow shock
1118 related effects that our data set can provide. Figure 9B shows the lunar PUI data from
1119 Hilchenbach et al. (1992) and Mall et al. (1998), the shaded and line histograms, respectively, for
1120 direct comparison of lunar PUIs slightly closer to Earth and near the Moon, respectively.
1121 Hilchenbach et al. (1992) selected antisunward flows at ~18 Re, ~3 Re sunward of the average
1122 bow shock location, during several intervals when the moon was approximately sunward of their
1123 spacecraft. Their data are the most comparable to ours, both data sets having been accumulated
1124 in approximately the same location, although for different purposes, with different
1125 methodologies, and under different solar activity conditions. They noted the presence of O^+ and
1126 suggested the presence of Al^+, Si^+, or S^+ (focusing on their counts near 32 amu/e, while rejecting
1127 detection of Earth's MI) as possible candidate ions for the observed Mass-30 ions, as well as a
1128 few ions with marginal statistics measured from 40 to 54 amu/e that they suggested were
1129 consistent with Ar^+, Ca^+, or Fe^+. Mall et al. (1998) presented two PHA histograms of lunar PUI
1130 data in their Figure 1. A lunar-radial variation was found, where lunar PUI counts decreased with

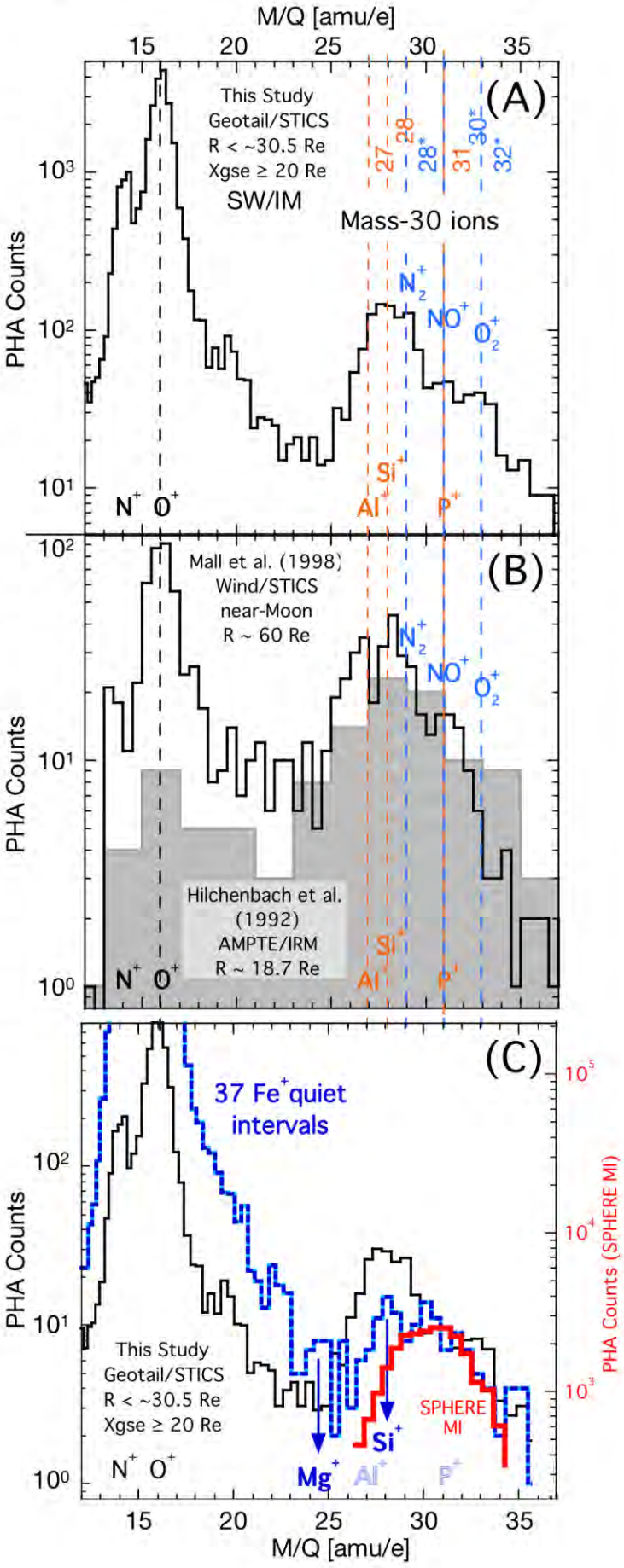

Figure 9. Histograms of N^+, O^+, and Mass 30 ion PHAs ordered by M/Q from (A) this study's farthest upstream Geotail/STICS data compared to that from (B) Mall et al. (1998) and Hilchenbach et al. (1992). Mass-30 molecular ion, MI (blue text), and lunar pickup ions, PUI (tan text), masses are identified. The MI generate higher M/Q values (asterisked values) than atomic ions of the same mass (see text). Our farthest upstream ~87-212 keV/e ion data were measured sunward of the bow shock at $X_{GSE} \geq 20$ Re out to R ~ 30.5 Re over approximately 2 full solar cycles. Hilchenbach et al. (1992) measured ~80-226 keV/e lunar PUIs sunward of the bow shock at R ≤ 18.7 Re over 3 months in late-1985. Mall et al. (1998) presented two PHA histograms of Wind/STICS measurements of ~20-200 keV/e lunar (PUI) obtained from 1995 to 1997 sunward of Earth near the Moon at >17 lunar radii. Given their study's lower number of counts, we summed their two PHA histograms into one (see text). N^+ and O^+ are shown for reference. Both the Hilchenbach et al. (1992) and Mall et al. (1998) data were obtained during minimum solar activity conditions. (C) This panel compares our farthest upstream data (black) to that from the overall SPHERE shape (red), which is dominated by MI, and to the 37 low to moderate solar/geomagnetic condition orbits used for the traces in Figure 7A (blue). Si^+ is both a major ionospheric origin ion from IDPs (Plane et al., 2016) and one of the major lunar pickup ions (e.g., Mall et al., 1998; Poppe et al., 2015). The quiet interval data show little similarity to our farthest upstream data, but do show evidence of peaks at Mg^+ and Si^+ (ionospheric ions) superposed on ions with the overall shape of the SPHERE data, but Al^+ and P^+ (lunar pickup ions) are not evident. The data are plotted in order to match their values near ~32 amu/e.

increasing distance from the Moon. On account of the low number of counts in their histograms, we summed their two M/Q histograms which widened their O^+ to Si^+ energy range to ~20-200 keV/e. We focus on their Mass-30 species, suppressing any discussion of other species they discussed with respect to their data (Mall et al. did not mention Fe^+). Their Moon-related measurements were obtained sunward of Earth at ~17-150 lunar radii from the Moon which is at ~60 Re from the Earth. The mixture of Mass-30 PUI atomic ion species in our summing of their data normalized to Si^+ (in absolute counts) is: $Al^+ : Si^+ : P^+ = 0.72 \pm 0.09 : 1.00 \pm 0.12 : 0.51 \pm 0.07$ (106 : 148 : 76 PHA counts, see also Figure S10 in the SI). In order to center the three data sets' O^+ peaks, we translated the M/Q locations of both the Hilchenbach et al. and Mall et al. data to slightly lower M/Q values by ~0.5 - 1 amu/e. All three data sets are limited by low counting statistics, different observation locations, and widely different solar activity conditions. That is, the Hilchenbach et al. (1992) and Mall et al. (1998) data were both obtained during solar activity minimum conditions, whereas our data encompass all data obtained over two solar cycles, and as seen in Figure 6, lunar ion production is likely enhanced during the disturbed solar conditions, conditions which also result in enhanced ionospheric outflow.

[4.2.0] Finally, Figure 9C shows that sunward of the bow shock O^+ and N^+ still dominate the omnidirectional heavy ions and the Mass-30 ion peak extends from ~25 to ~35 amu/e. We note that O_2^+ is likely evident by the contiguous elevated count levels up to ~34-35 amu/e in the two datasets measured sunward of the bow shock, ours and Hilchenbach et al. (1992). Therefore, these selected SW/IM data obtained somewhat upstream of the bow shock contain straightforward evidence of some O_2^+ in addition to P^+ || NO^+. Our study and Hilchenbach et al. (1992) both measured these data with similar time-of-flight versus total energy instruments, and it appears that both instruments reveal similar evidence sunward of the bow shock of an ion at

~2-3 amu/e higher than the likely P^+ location - an ion that we suggest is O_2^+ given our current understanding of these instruments' response to MI. That is, the near-bow shock data are not consistent with being explained alone by lunar PUI P^+, which should only mask a portion of the NO^+. While there is no obvious evidence of O_2^+ in the Mall et al. near-Moon data, there is evidence of O_2^+ in our data. Because of the small O_2^+ abundance relative to N_2^+ and NO^+ in the SPHERE, O_2^+ is difficult to detect there, being masked by NO^+ and/or various magnetospheric background signals present in this initial survey in which we have presented data from all geomagnetic and solar activity levels (see for example, the color spectrograms in Figure 2 and histograms in Figure 5). We are puzzled by the persistence of O_2^+ relative to N_2^+ and NO^+, species which have bond energies stronger than O_2, both as ions and neutral molecules (see Table S12 in the SI).

[4.2.1] Figure 9C shows this study's farthest upstream data compared to that from the data measured in various regimes on the 37 orbits of low to moderate solar/geomagnetic conditions, which were selected for their low Mass-30 ion conditions (Christon et al., 2017; see also Figure S5) and used to construct the traces in Figure 7A. Mass-30 ions have a peak near ~28 amu/e in both data sets. Si^+ is both a major ionospheric origin metal ion derived from IDPs (Zbinden et al., 1975; Plane et al., 2016) and a prominent lunar pickup ion (e.g., Mall et al., 1998; Halekas et al., 2015; Poppe, Halekas, et al., 2016). Although the quiet interval data show overall similarity to the farthest upstream data, evidence of a peak at Mg^+ and, although not a Mass-30 ion, at Na^+ (both likely from the ionosphere's meteoric metal ion layers), but not necessarily at Al^+ or P^+ (likely lunar pickup ions) argues more strongly for an ionospheric ion dominance and somewhat against a lunar pickup ion presence in these multi-regime data obtained during low-to-moderate

1178 geomagnetic activity. Mg^+, a well-known ionospheric IDP origin ion, has not been clearly
1179 identified in lunar PUI (Halekas et al., 2015; Poppe, Halekas, et al., 2016).
1180
1181 5. Discussion and Summary
1182 [5.0] Important new information on suprathermal atomic and molecular ions in and near the
1183 magnetospheres of Earth, Jupiter, and Saturn is presented in this paper. Although the principal
1184 intended subject of the paper did not initially include atomic ions, establishing characteristics of
1185 some atomic ions in and near the three magnetospheres, for example, a focus on S^+ at Jupiter and
1186 the characterization of some aspects of lunar pickup ions near Earth, was essential in more fully,
1187 and we hope more accurately, describing magnetospheric molecular ions at Earth and Saturn. We
1188 discuss our results in that context, with our primary focus on the molecules and only
1189 supplementary reportage on atomic ions as is relevant to this survey at this juncture.
1190 [5.1] Jupiter. Cassini was in the Jovian magnetosphere for far too short an interval for CHEMS to
1191 obtain detailed composition measurements. Nevertheless, review of the Cassini/CHEMS cruise
1192 data within ~2 AU of Jupiter shows the wide extent of Jovian-origin S^+ in the solar system.
1193 Interplanetary Jovian S^+ is not necessarily energized in Jupiter's magnetosphere, followed by
1194 subsequent escape. Rather, the S^+ in interplanetary space likely derives from energetic neutral S
1195 atoms that escape Jupiter and are subsequently ionized and picked up by the solar wind far from
1196 Jupiter, as demonstrated by Luhmann (2003). Inside the Jovian S^+ PUI cloud, CHEMS observed
1197 S^+ sporadically in interplanetary space from ~4.3 to ~6.6 AU (see Figures S1B and S12), but not
1198 outside of that heliocentric distance range (that is, before ~2000-246 or after ~2002-001). We
1199 feel that, at the level so far investigated, our observations are generally consistent with
1200 Luhmann's model. Even though the data are sparse, the basic unnormalized S^+ interplanetary

observations herein may help interested researchers refine their interplanetary transport models. We noted above that a small amount of Ca^+ and a possible trace of CO_2^+, may be present in and near Jupiter's magnetosphere. This Ca^+ and CO_2^+, and likely O^+, may escape from Jupiter's magnetosphere as S^+ clearly does, and some interplanetary/interstellar PUI O^+ likely enters Jupiter's magnetosphere, further complicating relative abundance comparisons used in evaluating magnetospheric sources and escape scenarios. Other Jupiter-related MI, such as SO^+ from Io and/or O_2^+ from the Galilean satellites, for example, may be ejected into the magnetosphere, but are more weakly bound than CO_2^+ (see Table S6 in the SI) and do not appear to survive in the harsh Jovian environment. Magnetospheric Jovian SO^+ and O_2^+ are not evident in our observations at suprathermal energies. The approximately equal amounts of O^+ and S^+ shown in Figure 3A argue for radiolysis of sulfur-based molecules as a source, with little contribution from the other possible O^+ sources, the water-ice Galilean satellites. However, full accounting of higher O and S charge states consistent with satellite source modeling may decide the true proportion of O^+ and S^+ derived from SO^+.

[5.2] Saturn. Of the ion species identified at up to ~35-40 amu/e inside Saturn's magnetosphere, all but Fe^+ appear to escape, but at or with different rates, paths, or modes. Of note, Fe^+ is not observed in the Solar Wind samples collected for this study. Further review of the complete Sheath and Solar Wind data near Saturn will be needed to expand discussion of this topic. Figures 4 and 5 summarize the new information about MI at Saturn. Although we do not explore details of MI dissociation herein, we suggest that the robust decrease of H_2O^+ relative to O^+ may result from either strong H2O+ impact dissociation in the solar wind or from differences in escape or transport processes. Both CO+ and O2+ appear to have fewer losses escaping Saturn's magnetosphere than C+, N+, and O+, in that the overall MI levels relative to O+ are higher in the

1224 Solar Wind than in the Sphere unlike the atomic ions whose levels relative to O+ are the same in
1225 both plasma regimes. This will all need to be sorted out when accurate instrumental efficiencies
1226 for these MI are applied and differential intensities are evaluated.

1227 [5.3] Earth. An important portion of this paper has been devoted to first establishing and
1228 characterizing the importance of the Mass-30 lunar PUI Al^+, Si^+, and P^+ that are present in the
1229 near-Earth environs outside the magnetosphere, and subsequently treating the lunar PUI as the
1230 background they are in this study of Earth's MI. We roughly quantified the ratios of N_2^+, NO^+,
1231 and O_2^+ that flow out of the ionosphere into Earth's magnetosphere, showing that, relatively, the
1232 components of the magnetospheric MI population are roughly ~43% N_2^+, ~47% NO^+, and ~10%
1233 O_2^+. While demonstrating the separation of several lunar PUI from escaped ionospheric N_2^+ in
1234 our solar wind data, we found possible evidence of a lunar Fe^{+2} PUI component. During low
1235 geomagnetic activity levels when lower levels of MI are present, Si^+, very difficult to
1236 differentiate from the MI signal, is likely present at levels comparable to Fe^+ in these select
1237 intervals, consistent with an ionospheric source for both. Si^+ would be far more evident than Fe^+
1238 if their source was the Moon, because repeated in situ efforts to measure Fe^+ near the Moon have
1239 produced null results. This study was our first opportunity to characterize and investigate these
1240 mixed distributions, given the rarity and low count levels of some of these ions and the need for
1241 sufficient data to make statistically sound relative species proportion estimates. It is clear that
1242 ionospheric origin molecular ions escape into the SHEATH and then into the SW/IM sunward of
1243 the bow shock, and it is likely that they also travel at least ~10-15 Re sunward of the nose of the
1244 bow shock into the upstream solar wind at 1 AU.

1245 6. Concluding Remarks

1246 [6.0] This paper provides new details regarding the molecular and atomic suprathermal heavy ion

composition in and near three important magnetospheres in the solar system, those of Earth, Saturn, and Jupiter. In the largest magnetosphere, that of Jupiter, S^+ and O^+ from dissociated Iogenic molecular S and O compounds and, possibly O^+ from its icy moons are dominant. Jovian S^+ escapes into the interplanetary medium. Tentatively identified CO_2^+ may originate in, survive in, and escape from Jupiter's magnetosphere. At Saturn, the icy moons and rings are the likely sources of its most prominent ions, O^+, H_2O^+, O_2^+, and CO^+. While C^+, N^+, O^+, OH^+, H_2O^+, CO^+, and O_2^+ all escape from Saturn's magnetosphere, Fe^+ is not detected in the Solar Wind near Saturn, and we do not attempt to estimate the relative OH^+ abundance herein. The overall ratio of H_2O^+ relative to O^+ decreases in interplanetary space; all other ion's overall ratios to O^+ are ≥ 1. H_2O^+ must either dissociate more quickly than the CO^+ and O_2^+, or its transport characteristics might constrain its escape more than for these two heavier molecules. At Earth, heavy ions observed inside the magnetosphere are dominated by those of ionospheric origin. Lunar origin ions are not detected at significant levels in the magnetosphere, except in the magnetospheric lobes where Mass-40 lunar Ca^+ and CO_2^+ PUI are detected. We demonstrate that the dominant heavy lunar PUI, Si^+, constitutes, at best, a negligible contribution to the long-term averaged suprathermal magnetospheric Mass-30 ion population. Our measurements of magnetospheric molecular ions, N_2^+ and NO^+ each ~43-46%, and O_2^+ ~10%, all originating in Earth's ionosphere, suggest that geomagnetic storms at Earth typically do not extract ions from ionospheric altitudes much lower or higher than ~300-500 km over the long term, that is, altitudes low enough to allow sufficient amounts of O_2^+ to escape, balanced with dominant, approximately equal, N_2^+ and NO^+ contributions.

7. Acknowledgments

We thank George Gloeckler who conceived the STICS and CHEMS spectrometers and directed their development at the University of Maryland Space Physics Group. Their excellent performance and long lifetimes made this study possible. This work would not exist without the encouragement of R. W. McEntire and D. J. Williams, and help of S. Lasley, R. DiFabio, J. Gunther, J. Cain, E. Tums, P. Wilson, O. Lamm, and many others. We thank NASA for support through Grant numbers NNX13AE61G and NNN06AA01C(NA07). JMCP's work was supported by the European Research Council (project number 291332 - CODITA). We thank C. W. Kelly (University of Leeds) for providing WACCM-X data. We acknowledge the use of the list of Cassini magnetopause and bow shock crossings compiled by H. J. McAndrews, S. J. Kanani, A. Masters, and J. C. Cutler. The NASA Plasma Region identifications for Geotail's orbital locations in and near Earth's magnetosphere were invaluable in this research. The Geotail/EPIC/STICS data set for 1992 through 2010 can be found at http://spdf.gsfc.nasa.gov/pub/data/geotail/epic/stics_pha_ascii_gzip/ and for later times at http://sd-www.jhuapl.edu/Geotail/. Geotail ephemeris data are at http://sscweb.gsfc.nasa.gov/. Solar and geomagnetic indices were obtained from both http://omniweb.gsfc.nasa.gov/form/dx1.html and http://wdc.kugi.kyoto-u.ac.jp/dstae/. The entire Cassini/MIMI/CHEMS data set and Cassini ephemeris data can be found at http://pds.nasa.gov. S.P.C. thanks J. M. Huba for a helpful discussion about the SAMI3 Model which was developed by J. Huba, G. Joyce, and M. Swisdak of the Plasma Physics Div., Naval Research Laboratory and Icarus Research, Inc. SAMI3 simulation results are provided by the Community Coordinated Modeling Center at Goddard Space Flight Center through their public Runs on Request system (http://ccmc.gsfc.nasa.gov).

7 Glossary

Glossary of Acronyms and Terms

BR* - Basic Rate M-vs-M/Q collection region (where * is 0 - 2 for STICS and 0 - 6 for CHEMS)

CHEMS - the Charge-Energy-Mass ion composition Spectrometer on the Cassini spacecraft

CIR - large-scale, fast/slow solar wind stream interaction regions that corotate with the sun

CME - Coronal Mass Ejection - large-scale solar plasma flux that propagates in the solar wind

E - total ion kinetic energy

Em - energy deposited in the solid state detector by an incident ion

EPIC - the energetic particle experiment on the Geotail spacecraft in Earth orbit

escape - the process of magnetospheric ions exiting the magnetospheres of their origination

EUV - Extreme UltraViolet high-energy electromagnetic radiation naturally generated by the sun which affects planetary atmospheres and ionospheres

F10.7 - a measurement of the 10.7 cm radio flux RF emissions from the Sun, approximately correlated with solar EUV flux

IDP - Interplanetary Dust Particle (dust, small asteroids, meteoroids, comet particulates)

io..., pu..., sw..., - prefixes distinguishing ionosphere, pickup, and solar wind source ions

Kp - geomagnetic activity index

livetime correction - procedure used in calculating ion fluxes using PHAs and Basic Rates

LOBE - part of magnetosphere where magnetic field pressure dominates over plasma pressure

LPUI - a lunar origin PUI

M - ion mass determined instrumentally from energy deposit and time of flight

M/Q - mass per charge determined instrumentally from time of flight and E/Q

magnetosphere - region where planetary magnetic fields dominate

Mass-16 ions ($^{16}M^+$): Earth: N^+, O^+; Jupiter: O^+; Saturn: C^+, N^+, O^+, OH^+, H_2O^+, H_3O^+

Mass-20 ions ($^{20}M^+$): Earth, Moon, Jupiter, Saturn, Interplanetary: Ne^+, Na^+, Mg^+

Mass-30 ions ($^{30}M^+$): Earth(Moon): N_2^+, NO^+, Al^+, Si^+, P^+; Jupiter: S^+; Saturn: CO^+, O_2^+

Mass-40 ions ($^{40}M^+$): Earth(Moon): K^+, Ar^+, Ca^+, CO_2^+, SiO^+, Ti^+; Jupiter: CO_2^+, SO^+; Saturn: Ar^+ || Ca^+, CO_2^+

MIMI - the energetic particle experiment on the Cassini spacecraft

$^{28}MQ^+$ - Saturn's ~28-30 amu/e molecular ions, which could be N_2^+ and/or CO^+

outflow - the process in which ions exit (flow out of) the ionosphere of their origination

PHA - a Pulse Height Analyzed ion event sample of all ions measured by STICS or CHEMS

prime Fe PHA - a Fe PHA event in a restricted M and MPQ analysis range

PUI - a PickUp Ion, an initially neutral particle ionized and picked up by the solar wind

Q - charge (charge state) of an ion

RID - an acronym for plasma Regime IDentification, only used in the Supporting Information

SHEATH - turbulent, shocked solar wind plasma region between magnetopause and bow shock

Solar Cycle - the ~11-year disturbance activity cycle of the sun

SPHERE - parts of magnetosphere where particle pressure dominates over magnetic pressure

STICS - SupraThermal Ion Composition Spectrometer charge-energy-mass ion composition spectrometers on the Geotail and WIND spacecraft

SW, SH, SP, LB - two-letter acronyms for the SW/IM, SHEATH, SPHERE, and LOBE names

SW/IM - unshocked solar wind, interplanetary medium outside the bow shock

TOF - time of flight measured instrumentally

Vsw - solar wind speed

W^+ - ion group containing O^+, OH^+, H_2O^+, and H_3O^+

8 Figure Captions

Figure 1. Heavy suprathermal (CHEMS, ~83-167 keV/e; STICS, ~87–212 keV/e) ion Pulse Height Analysis PHA data obtained by: (top) Geotail in and near Earth's magnetosphere; (middle) Cassini during its Jupiter flyby as well as in the interplanetary medium from ~3-9 AU when S^+ was measured; and (bottom) Cassini in Saturn's ≲20 Rs magnetosphere (see text for details). The PHA data are presented as (A, left) mass-per-charge (M/Q) histograms and (B, right) mass (M) versus M/Q color spectrograms (colorbars suppressed). Stars at right and horizontal dashed lines identify M = 32 amu. All data were adjusted slightly in order to center N^+, O^+, and S^+ on their atomic mass in order to account for instrument and spacecraft electronics differences. Mass-30 ions include ~27-33 amu/e. General sources of the Mass-30 ions at each planet are noted.

Figure 2. Earth's dayside molecular ion number density profiles of N_2^+, NO^+, and O_2^+ at ~60º N latitude around Spring equinox calculated for solar maximum (MAX) and minimum (MIN) conditions from (A) the SAMI3 ionosphere model near local noon and (B) the WACCM-X thermosphere/ionosphere model for a one-month narrow-latitude zonal average; see text for input parameter and run information. Unique symbols identify and differentiate the three MI species' altitude profile similarities and differences. The red and blue shaded areas, indicate altitude ranges that vary with solar cycle in which the N_2^+, NO^+ densities are approximately equal and O_2^+ levels are somewhat lower, but not absent. This unique molecular ion composition signature is characteristic of outflowing MI (see text).

Figure 3. Cassini's measurements of jovian and solar wind/interplanetary medium suprathermal (~83-167 keV/e) ion populations during: (top) the Jupiter flyby between inbound and outbound bow shock encounters; (middle) the extended interval over which S^+ from Jupiter was detected in the solar wind before, during, and after the Jupiter flyby; and (bottom) the ~3 year Cassini cruise to Saturn ,excluding the extended ~1-year interval of jovian fluxes from the middle panel. The tentative identification of jovian magnetospheric Ca^+ and CO_2^+ are noted by lighter dotted lines.

Figure 4. Mass distributions of Mass-30 suprathermal (CHEMS at Saturn, ~83-167 keV/e; STICS at Earth, ~87–212 keV/e) ion data at Saturn and Earth highlight atomic and molecular ion (MI) differences. Data points and smoothed fits are shown. The indeterminate species descriptors "$^{28}Ma^+$" and "$^{30}Ma^+$" are used as ion species channel names in this figure for primarily singly charged Mass-30 ions selected in narrow M/Q ranges near 28 and 30 amu/e because it is clear that there is an admixture of ion species in at least two cases. The identifier "Ma" represents a M-M/Q spectrogram selection over a limited M/Q, but wide M, range in which the selected ions' species identification is sometimes complex (see text for the full discussion). Mass histograms of $^{28}Ma^+$, $^{30}Ma^+$, and/or $^{32}Ma^+$, heavy ion species having mass numbers of 28, 30, and 32 amu, respectively, are likely dominated by CO^+ (or N_2^+), NO^+, and O_2^+. At Saturn, data from mid-2004 through 2007 containing: (A) all intervals when Cassini was in Saturn's magnetosphere, the Sphere, at ~$4 < R < 20$ R_S; and (B) only intervals in the solar wind for which an outbound and a subsequent inbound bow shock (BS) crossing were identified, including travel to and from apoapsis, thus placing Cassini in the Solar Wind near Saturn at $R > R_{BS}$, the distance of Cassini's bow shock encounters. Representative uncertainties are shown near the right vertical axis in (B). At Earth, data from early-1995 through 2015 are shown for intervals when Geotail was in (C) the

SPHERE, Earth's magnetosphere, and (D) the SW/IM, the near Earth, unshocked, solar wind of the interplanetary medium. See text for details.

Figure 5. Long-term suprathermal (CHEMS, ~83-167 keV/e; STICS, ~87–212 keV/e) heavy ion composition measurements in near-Earth (A, B) and near-Saturn (C) plasma regimes are normalized to O^+ and compared directly. The vertical axes of SPHERE data (red left axis labels), SHEATH, and SW/IM data (blue right axis labels) are offset in order to compare selected species' importance relative to O^+. Shown are ~21 continuous years of Earth data and samples from ~3 years of select Solar Wind and contemporaneous Sphere intervals at Saturn. Note the distinct plasma regime labeling which differentiates the two planets' regimes in the text and highlights their different selection procedures. Vertical fiducial lines at 16, 32, and 56 amu/e are drawn to simplify visual comparison. At Earth, the Mass-30 SHEATH (A: blue) distribution is intermediate between that of the SPHERE (A, B: red) and SW/IM (B: blue). Floating insets (near bottom of A and B) show rough visual fits (orange) to the background (bk) subtracted SPHERE (SP-bk, black), SHEATH (SH), and SW/IM (SW, at distances $R > R_{BS}$, the distance to the bow shock) data. The fits use SPHERE MI (A: rose for N_2^+ and NO^+, light blue for O_2^+) and select distributions of lunar pickup ions, PUI, and/or, in the case of the SPHERE, ionospheric Si^+ (purple) at the Fe^+ level (long-dash line). Prominent lunar PUI species are identified. (D) In these instruments, dominant SPHERE molecular ion (MI) dissociation energy loss in the carbon foil result in slightly longer times-of-flight (TOF) with subsequently higher M/Q values than for the dominant SW/IM atomic ions of the same mass. See text.

Figure 6. Averages of suprathermal (~87–212 keV/e) N^+, O^+, Fe^+, Mass-30 ions ($^{28}Mq^+$ and $^{30}Mq^+$) and Mass-40 ions 3-hr PHA count sums are plotted versus interval averages of (A, B) Kp and (C) $F_{10.7}$ values from 1995 to 2015. In (A) and (B), all data are shown. In (B) the data are

from two plasma regimes, SPHERE (open symbols) and SW/IM (closed symbols). Uncertainties, standard error of the mean, are generally smaller than the point size. Horizontal bars in (C) indicate $F_{10.7}$ ranges. Kp averages are over the -, ○, + range of the Kp index integer values. Dashed and dotted lines in (A and C) are intended to guide the eye in comparing the heavier ions to N^+ and O^+ (see text). The dotted extension of the Fe^+ line in (A) highlights the outlying Kp = 3 average which is also apparent in the SW/IM data.

Figure 7. (A) A sketch of the Earth (blue dot at center), the Moon's orbital range, and Geotail orbital range, ~9 < R < 35 Re. Two spatial criteria for considering possible lunar pickup ion influence in Geotail/STICS suprathermal (~87–212 keV/e) ion measurements are the lunar local time (LLT) and the 'Lunar Wake'. LLT marks the orbital location of the Moon with respect to the Earth-Sun line. At 10 ≤ LLT ≤ 13 hours, LLT-sector 3, the Moon is sunward of Geotail's nominal orbital X_{GSE} -Y_{GSE} range. From favorable orbit locations ~60 Re sunward of Earth, the Moon can convectively contribute pickup ions to our SW/IM data near Earth. The 'Lunar Wake', drawn here with a ~25 Re width to include heavy ion (e.g., CO_2^+ or Fe^+) gyroradii in the nominal (~7-9 nT) interplanetary magnetic field at 1 AU, is probably always present, varying in strength, and is likely important in supplying lunar PUI to near-Earth locations. Selected segments of Geotail orbits, the dotted traces near Earth, terminate when an Fe^+ was observed during low to moderate solar/geomagnetic conditions. White (black) squares indicate Fe^+ observations obtained when the Moon was (not) in LLT-sector 3. Red dots show other measured Fe^+ data. Arrows point from underlined labels to three near-Earth plasma regimes. The LOBE (not shown) overlies the SPHERE. (B,C) Four panels at (B) High-Kp and (C) Low-Kp levels enable investigation of some possible observable effects of lunar PUIs intermixed with Earth's escaped ionospheric ions which are related to the Moon's orbital location. The effects differ between

observations made in the four near-Earth plasma regimes used in this study.

Figure 8. The superposition of the PHA distributions of lunar pickup ions, PUI, mostly Si^+, and ionospheric N_2^+ in the near-Earth solar wind, SW/IM, PHA distributions is investigated using two different comparisons. (A) The suprathermal (~87–212 keV/e) ion data are all from the SW/IM plasma regime near Earth. Solid curves are smoothed, interpolated fits to the data in Figure 3D. The shape of neither the $^{28}Ma^+$, 28-amu (orange), nor $^{30}Ma^+$, 30-amu (purple), ion mass distribution, is similar to the corresponding bimodal SPHERE MI shapes at Earth or Saturn (see the scaled SPHERE shape in panel 8B and Figure 4C). Expecting a smaller lunar PUI background in the $^{30}Ma^+$ data based on previous measurements by Mall et al. (1998), we approximate Earth's MI portion of the $^{28}Ma^+$ SW/IM data by scaling the $^{30}Ma^+$ curve upward (dashed purple curve), and subtract this from the SW/IM $^{28}Ma^+$ (orange) curve. This results in the black dashed curve, a crude estimate of lunar PUI (mostly Si^+ and Al^+) contributing to the $^{28}Ma^+$ data, which has a shape similar to the SW/IM O^+ (shown also as the red dashed curve shifted to ~30 amu). Differences between the Fit and Data below the gray horizontal area drawn at ~10-12 counts are not statistically significant. (B, C, and D) In a different treatment investigating possible components of the SW/IM $^{28}Ma^+_{SW}$ data, we construct a Fit from a scaled combination of Earth's SPHERE MI, $^{28}Ma^+_{SP}$ and $^{30}Ma^+_{SP}$, ions added to different ratios of relevant lunar atomic PUI populations. Al^+, Si^+, and P^+ were identified by Mall et al. (1998) as the principal Mass-30 ions. Separately, in a panel below each set of PUI and Fit curves, the difference between our Fit and the measured $^{28}Ma^+_{SW}$ ions is shown along with dashed +1 to -3 standard deviation curves for the Data. In panel 8B, we use our derived Mall et al. relative proportions (see text) and in panel 8C, we adjust the PUI Al^+, Si^+, and P^+ relative proportions to get a better visual fit. Finally, in panel 8D, in order to further reduce the Fit - Data differences,

1449 we combine those best-fit lunar PUI proportions with a hypothetical lunar Fe^{+2} population to
1450 compare to the Data.

Figure 9. Histograms of N^+, O^+, and Mass 30 ion PHAs ordered by M/Q from (A) this study's farthest upstream Geotail/STICS data compared to that from (B) Mall et al. (1998) and Hilchenbach et al. (1992). Mass-30 molecular ion, MI (blue text), and lunar pickup ions, PUI (tan text), masses are identified. The MI generate higher M/Q values (asterisked values) than atomic ions of the same mass (see text). Our farthest upstream ~87-212 keV/e ion data were measured sunward of the bow shock at $X_{GSE} \geq 20$ Re out to R ~ 30.5 Re over approximately 2 full solar cycles. Hilchenbach et al. (1992) measured ~80-226 keV/e lunar PUIs sunward of the bow shock at R ≤ 18.7 Re over 3 months in late-1985. Mall et al. (1998) presented two PHA histograms of Wind/STICS measurements of ~20-200 keV/e lunar (PUI) obtained from 1995 to 1997 sunward of Earth near the Moon at >17 lunar radii. Given their study's lower number of counts, we summed their two PHA histograms into one (see text). N^+ and O^+ are shown for reference. Both the Hilchenbach et al. (1992) and Mall et al. (1998) data were obtained during minimum solar activity conditions. (C) This panel compares our farthest upstream data (black) to that from the overall SPHERE shape (red), which is dominated by MI, and to the 37 low to moderate solar/geomagnetic condition orbits used for the traces in Figure 7A (blue). Si^+ is both a major ionospheric origin ion from IDPs (Plane et al., 2016) and one of the major lunar pickup ions (e.g., Mall et al., 1998; Poppe et al., 2015). The quiet interval data show little similarity to our farthest upstream data, but do show evidence of peaks at Mg^+ and Si^+ (ionospheric ions) superposed on ions with the overall shape of the SPHERE data, but Al^+ and P^+ (lunar pickup ions) are not evident. The data are plotted in order to match their values near ~32 amu/e.

9 References

1473 Allen, R. C., Mitchell, D. G., Paranicas, C. P., Hamilton, D. C., Clark, G., Rymer, A. M., et al.
1474 (2018). Internal versus external sources of plasma at Saturn: Overview from Magnetospheric
1475 Imaging Investigation/Charge-Energy-Mass Spectrometer data. J*ournal of Geophysical*
1476 *Research: Space Physics, 123*, 4712–4727. https://doi.org/10.1029/2018JA025262

1477 Andersson, L., Peterson, W. K., & McBryde, K. M. (2004). Dynamic coordinates for auroral ion
1478 outflow., *Journal of Geophysical Research, 109, A08201*.
1479 https://doi.org/10.1029/2004JA010424.

1480 Baluikin, I. I., Bertaux, J.-L., Quémerais, E., Izmodenov, V. V., & Schmidt, W. (2019).
1481 SWAN/SOHO lyman-a-mapping: Hydrogen Geocorona extends far beyond the moon. *Journal*
1482 *of Geophysical Research: Space Physics, 124* (accepted). DOI: 10,1029 / 2018JA026136

1483 Bautista, M. A., Romano, P., & Pradhan, A. K. (1998). Resonance-averaged photoionization
1484 cross sections for astrophysical models. *Astrophysical Journal Supplement Series, 118*(1), 259-
1485 265. https://doi.org/10.1086/313132

1486 Benna, M., Mahaffy, P. R., Halekas, J. S., Elphic, R. C., & Delory, G. T. (2015). Variability of
1487 helium, neon, and argon in the lunar exosphere as observed by the LADEE NMS instrument.
1488 *Geophysical Research Letters, 42*, 3723–3729. https://doi.org/doi:10.1002/ 2015GL064120

1489 Blagoveshchenskii, D. V. (2013). Effect of geomagnetic storms (substorms) on the ionosphere:
1490 1. A review. *Geomagnetism and Aeronomy, 53*, 3, 275-290.
1491 https://doi.org/10.1134/S0016793213030031

1492 Bockelée-Morvan, D. (2011). An overview of comet composition. in *IAU Symposium 280, The*
1493 *Molecular Universe*, edited by J. Cernicharo, & R. Bachiller (Cambridge: Cambridge Univ.
1494 Press), 261-274. https://doi.org/10.1017/S1743921311025038

1495 Bodisch, K. M., Dougherty, L. P., & Bagenal, F. (2017). Survey of Voyager plasma science ions
1496 at Jupiter: 3. Protons and minor ions, *Journal of Geophysical Research: Space Physics, 122*.
1497 https://doi.org/10.1002/ 2017JA024148.
1498 Bridges, J. C., Burchell, M. J., Changela, H. C., Foster, N. J., Cre, J. A., Carpenter, J. D.,
1499 Gurman, S. J., Franchi, I. A., & Busemann, H. (2010). Iron oxides in comet 81P/Wild 2,
1500 *Meteoritics and Planetary Science, 45*, 1, 55–72. https://doi.org/10.1111/j.1945-
1501 5100.2009.01005.x
1502 Campbell, R. D., & Lin, R. P. (1973). Energy loss of low energy nuclei in silicon surface barrier
1503 detectors. *Review of Scientific Instruments., 44, 10*, 1510-1512.
1504 https://doi.org/10.1063/1.1685986
1505 Cannata, R. W. (1990). Thermal ion upwelling in the High-Latitude Ionosphere. Ph.D.
1506 Dissertation, Atmospheric and Space Sciences, University of Michigan.
1507 Carlson, R. W. (1999). A tenuous carbon dioxide atmosphere on Jupiter's moon Callisto, *Science*
1508 *283*, 5403, 820-821. https://doi.org/10.1126/science.283.5403.820
1509 Carrillo-S. nchez, J. D., Nesvorn. , D., Pokorný, P., Janches, D., & Plane, J. M. C. (2016).
1510 Sources of cosmic dust in the Earth's atmosphere. *Geophysical Research Letters, 43*, 11,979–
1511 11,986. https://doi.org/10.1002/ 2016GL071697.
1512 Christon, S. P., Gloeckler, G., Williams, D. J., Mukai, T., McEntire, R. W., Jacquey, C., et al.
1513 (1994). Energetic atomic and molecular ions of ionospheric origin observed in distant
1514 magnetotail flow-reversal events. *Geophysical Research Letters, 21*, 3023–3026. https://doi.
1515 org/10.1029/94GL02095
1516 Christon, S. P., Hamilton, D. C., Gloeckler, G., Eastman, T. E., & Ipavich, F. M. (1994). High
1517 charge state carbon and oxygen ions in Earth's equatorial quasi-trapping region. *Journal of*

Geophysical Research: Space Physics, 99(A7), 13465–13488. https://doi.org/10.1029/93JA0332

Christon, S. P., Hamilton, D. C., Mitchell, D. G., DiFabio, R. D., & Krimigis, S. M. (2014). Suprathermal magnetospheric minor ions heavier than water at Saturn: Discovery of $^{28}M^{+}$ seasonal variations. *Journal of Geophysical Research: Space Physics, 119*. https://doi.org/10.1002/2014JA020010

Christon, S. P., Hamilton, D. C., DiFabio, R. D., Mitchell, D. G., Krimigis, S. M., & Jontof-Hutter, D. S. (2013). Saturn suprathermal O_2^{+} and mass-28^{+} molecular ions: Long-term seasonal and solar variation. *Journal of Geophysical Research: Space Physics, 118*. https://doi.org/10.1002/jgra.50383

Christon, S.P., Desai, M. I., Eastman, T. E., Gloeckler, G., Kokubun, S.,. Lui, A. T. Y, McEntire, R. W., Roelof, E. C., & Williams, D. J. (2000). Low-charge-state heavy ions upstream of Earth's bow shock and sunward flux of ionospheric O^{+1}, N^{+1}, and O^{+2} ions: Geotail observations. *Geophysical Research Letters, 27*, 2433-2436. https://doi.org/10.1029/2000GL000039

Christon, S. P., Hamilton, D. C., Mitchell, D. G., DiFabio, R. D., & Krimigis, S. M. (2014). Suprathermal magnetospheric minor ions heavier than water at Saturn: Discovery of $^{28}M^{+}$ seasonal variations. *Journal of Geophysical Research: Space Physics, 119*, 5662–5673. https://doi.org/10.1002/2014JA020010

Christon, S. P., Hamilton, D. C., Plane, J. M. C., Mitchell, D. G., DiFabio, R. D., & Krimigis, S. M. (2015). Discovery of suprathermal Fe^{+} in Saturn's magnetosphere. *Journal of Geophysical Research: Space Physics, 120*, 2720–2738. https://doi.org/10.1002/2014JA020906

1540 Christon, S. P., Hamilton, D. C., Plane, J. M. C., Mitchell, D. G., Grebowsky, J. M., Spjeldvik,
1541 W. N., & Nylund, S. R. (2017). Discovery of suprathermal ionospheric origin Fe^{+} in and near
1542 Earth's magnetosphere. *Journal of Geophysical Research: Space Physics, 122*.
1543 https://doi.org/10.1002/2017JA024414

1544 Christon, S. P., Mall, U., Eastman, T. E., Gloeckler, G., Lui, A. T. Y., McEntire, R. W., Roelof,
1545 E. C. (2002). Solar cycle and geomagnetic N^{+1}/O^{+1} variation in outer dayside magnetosphere:
1546 Possible relation to topside ionosphere. *Geophysical Research Letters, 29*(5), 1058. https://doi.
1547 org/10.1029/2001GL013988

1548 Cohen, I. J., Mauk, B. H., Anderson, B. J., Westlake, J. H., Sibeck, D. G., Giles, B. L., et al.
1549 (2016), Observations of energetic particle escape at the magnetopause: Early results from the
1550 MMS Energetic Ion Spectrometer (EIS), *Geophysical Research Letters,* 43, 5960–5968,
1551 https://doi.org/doi:10.1002/2016GL068689

1552 Cooper, J. F., Johnson, R. E., Mauk, B. H., Garrett, H. B., Gehrels, N. (2001). Energetic Ion and
1553 Electron irradiation of the icy galilean satellites. *Icarus, 149, 1*, 133-159.
1554 https://doi.org/10.1006/icar.2000.6498

1555 Craven, P. D., Olsen, R. C., Chappell, C. R., & Kakani, L. (1985). Observations of molecular
1556 ions in the Earth's magnetosphere. *Journal of Geophysical Research, 90*(A8), 7599–7605.
1557 https://doi.org/10.1029/JA090iA08p07599

1558 Danilov, A. D., & Lastovica, J. (2001) Effects of geomagnetic storms on the ionosphere and
1559 atmosphere, *International Journal of Geomagnetism and Aeronomy, 2*, 3, 209-224.
1560 http://elpub.wdcb.ru/journals/ijga/v02/gai99312/gai99312.htm

1561 DiFabio, R. D., Hamilton, D. C., Krimigis, S. M., & Mitchell, D. G. (2011). Long term time
1562 variations of the suprathermal ions in Saturn's magnetosphere. *Geophysical Research Letters*, ,
1563 L18103. https://doi.org/:10.1029/ 2011GL048841
1564 DiFabio, R. D. (2012). Spatial and temporal variations of the suprathermal (3-220 keV/e) ion
1565 composition in Saturn's equatorial magnetosphere. Ph.D. Dissertation. University of Maryland,
1566 College Park, Maryland, USA. https://drum.lib.umd.edu/handle/1903/12700
1567 Dukes, C. A., & Baragiola, R. A. (2015). The lunar surface-exosphere connection: Measurement
1568 of secondary-ions from Apollo soils. *Icarus, 255*, 51-57.
1569 https://doi.org/10.1016/j.icarus.2014.11.032
1570 Eckardt, J. C.; Lantschner, G.; Arista, N. R.; Baragiola, R. A.Baragiola (1978). Electronic
1571 stopping of slow molecular ions in solids. *Journal of Physics C: Solid State Physics, 11, 21*,
1572 L851-L855. https://doi.org/doi:10.1088/0022-3719/11/21/001
1573 Elphic, R. C., Funsten III, H. O., Barraclough, B. L., McComas, D. J., Paffett, M. T., Vaniman,
1574 D. T., & Heiken, G. (1991). Lunar surface composition and solar wind-induced secondary ion
1575 mass spectrometry. *Geophysical Research Letters, 18*, 2165-2168.
1576 https://doi.org/10.1029/91GL02669
1577 Foss, V., Yau, A. W., & Shizgal, B. (2017). Molecular ions in ion upflows and their effects on
1578 hot atomic oxygen production. American Geophysical Union Fall Meeting 2017, abstract
1579 #SA43B-2654. http://adsabs.harvard.edu/abs/2017AGUFMSA43B2654F
1580 Fujimoto, M., Nishida, A., Mukai, T., Saito, Y., Yamamoto, T., & Kokubun, S. (1996). Plasma
1581 entry from the flanks of the near-earth magnetotail: GEOTAIL observations in the dawnside
1582 LLBL and the plasma sheet. *Journal of Geomagnetism and Geoelectricity, 48, 5*, 711-727.
1583 https://doi.org/10.5636/jgg.48.711

1584 Fujimoto, M., Terasawa, T., Mukai, T., Saito, Y., Yamamoto, T., & Kokubun, S. (1998). Plasma
1585 entry from the flanks of the near-Earth magnetotail: Geotail observations. *Journal of*
1586 *Geophysical Research, 103*, 4391–4408. https://doi.org/10.1029/97JA03340 Geotail/EPIC
1587 Instrument Users Manual (IUM), prepared by C. E. Schlemm (1993) also referred to as the
1588 Geotail/EPIC_IUM; a concise, reduced version of the EPIC DPU Software Users Guide,
1589 prepared by A. Hestermeyer (1991).
1590 Gilbert, J. A., Lepri, S. T., Landi, E., & Zurbuchen, T. H. (2012). First measurements of the
1591 complete heavy-ion charge state distributions of C, O, and Fe associated with interplanetary
1592 coronal mass ejections. *Astrophys. Journal, 751*, 20. https://doi.org/10.1088/0004-
1593 637X/751/1/20
1594 Gloeckler, G., Balsiger, H., Bürgi, A., Bochsler, P., Fisk, L. A., Galvin, A. B., Geiss, J., Gliem,
1595 F., Hamilton, D. C., Holzer, T. E., Hovestadt, D., Ipavich, F. M., Kirsch, E., Lundgren, R. A.,
1596 Ogilvie, K. W., Sheldon, R. B., & Wilken, B. (1995). The solar wind and suprathermal ion
1597 composition investigation on the WIND spacecraft. *Space Science Reviews, 71*, 1–4, 79–124.
1598 https://doi. org/10.1007/BF00751327
1599 Gloeckler, G., Fisk, L. A., Geiss, J., Schwadron, N. A., & Zurbuchen, T. H. (2000). Elemental
1600 composition of the inner source pickup ions. *Journal of Geophysical Research, 105*, 7459–
1601 7463. https://doi.org/10.1029/1999JA000224
1602 Gloeckler, G., Fisk, L. A., Zurbuchen, T. H., & Schwadron, N. A. (2000). Sources, injection and
1603 acceleration of heliospheric ion populations. In R. Mewaldt, et al. (Eds.), *AIP Conference*
1604 *Proceedings,* CP528*: Acceleration and Transport of Energetic Particles Observed in the*
1605 *Heliosphere: ACE 2000 Symposium* (pp. 221–228). https://doi.org/10.1063/1.1324316

1606 Gloeckler, G., & Hamilton, D. C. (1987). AMPTE ion composition results. *Physica Scripta, T18*,
1607 73–84. https://doi.org/10.1088/0031-8949/1987/T18/009
1608 Gomis, O., & Strazzulla, G. (2005). CO_2 production by ion irradiation of H_2O ice on top of
1609 carbonaceous materials and its relevance to the Galilean satellites. Icarus, 177, ,2, 570-576.
1610 https://doi.org/10.1016/j.icarus.2005.04.003
1611 Goncharenko, L. P., Salah, J. E., Foster, J. C., & Huang, C. (2004). Variations in lower
1612 thermosphere dynamics at midlatitudes during intense geomagnetic storms, *Journal of*
1613 *Geophysical Research, 109,* A04304, doi:10.1029/2003JA010244
1614 Grebowsky, J. M., & Aikin, A. C. (2002). In situ measurements of meteoric ions. In E. Murad, &
1615 I. P. Williams (Eds.), *Meteors in the Earth's Atmosphere* (pp. 189–214). Cambridge:
1616 Cambridge Univ. Press.
1617 Haaland, S., Eriksson, A., Engwall, E., Lybekk, B., Nilsson, H., Pedersen, A., Svenes, K., André,
1618 M., Förster, M., Li, K., Johnsen, C., Østgaard, N. (2012). Estimating the capture and loss of
1619 cold plasma from ionospheric outflow. Journal of Geophysical Research, 117, A7.
1620 http://doi.org/10.1029/2012JA017679
1621 Haggerty, D. K., Hill, M. E., McNutt Jr., R. L., & Paranicas, C. (2009). Composition of energetic
1622 particles in the Jovian magnetotail, *Journal of Geophysical Research*, 114, A02208.
1623 https://doi.org/10.1029/2008JA013659
1624 Halekas, J. S., Benna, M., Mahaffy, P. R., Elphic, R. C., Poppe, A. R., & Delory, G. T. (2015).
1625 Detections of lunar exospheric ions by the LADEE neutral mass spectrometer. *Geophysical*
1626 *Research Letters, 42*, 5162–5169. https://doi.org/10.1002/2015GL064746

1627 Hibbitts, C. A., McCord, T. B., & Hansen, G. B. (2000). Distributions of CO_2 and SO_2 on the
1628 surface of Callisto. *Journal of Geophysical Research, 105*, 22541-22558.
1629 https://doi.org/10.1029/1999JE001101
1630 Hilchenbach, M., Hovestadt, D., Klecker, B., & Moebius, E. (1992). Detection of singly ionized
1631 lunar pick-up ions upstream of the Earth's bow shock. in *Solar Wind Seven; Proceedings of the*
1632 *3rd COSPAR Colloquium*, Goslar, Germany, Sept. 16-20, 1991 (A93-33554 13-92), p. 349-
1633 355.
1634 Hoegy, W. R., Grebowsky, J. M., & Brace, L. H. (1991). Ionospheric ion composition from
1635 satellite measurements made during 1970–1980: Altitude profiles, *Adv.ances in Space*
1636 *Research, 11*, 173–182. https://doi.org/10.1016/0273-1177(91)90340-P
1637 Huba, J. D., Joyce, G., & Fedder, J. A. (2000). Sami2 is Another Model of the Ionosphere
1638 (SAMI2): A new low-latitude ionosphere model. *Journal of Geophysical Research, 105*(A10),
1639 23035–23053. https://doi.org/10.1029/2000JA000035
1640 Huba, J. D., Joyce, G., & Krall, J. (2008). Three-dimensional equatorial spread F modeling.
1641 *Geophysical Research Letters, 35*, L10102. https://doi.org/10.1029/ 2008GL033509
1642 Ilie, R., & Liemohn, M. W. (2016). The outflow of ionospheric nitrogen ions: A possible tracer
1643 for the altitude-dependent transport and energization processes of ionospheric plasma. *Journal*
1644 *of Geophysical Research: Space Physics, 121*, 9250–9255.
1645 https://doi.org/10.1002/2015JA022162
1646 Ipavich, F. M., R. A. Lundgren, B. A. Lambird and G. Gloeckler (1978). Measurements of pulse-
1647 height defect in Au-Si detectors for H, He, C, N, O, Ne, Ar, Kr from ~2 to ~400 keV/nucleon,
1648 *Nuclear Instruments and Methods, 154*, 291-294. https://doi.org/10.1016/0029-
1649 554X(78)90412-3.

1650 Johnson, R. E., Carlson, R. W., Cooper, J. F., Paranicas, C., Moore, M. H., Wong, M. C. (2004).
1651 Radiation effects on the surfaces of the Galilean satellites. in *Jupiter. The planet, satellites and*
1652 *magnetosphere*. ed. by F. Bagenal, T. E. Dowling, & W. B. McKinnon (Eds.) 485-512.
1653 Cambridge Planetary Science, Vol. 1, Cambridge, UK. Cambridge University Press., isbn: 0-
1654 521-81808-7.

1655 Kallenbach, R., Geiss, J., Gloeckler, G., & von Steiger, R. (2000). Pick-up ion measurements in
1656 the heliosphere—A review. *Astrophysics and Space Science, 274*, 97.
1657 https://doi.org/10.1023/A:1026587620772

1658 Kim, Y. H., Pesnell, W. D., Grebowsky, J. M., & Fox, J. L. (2001). Meteoric ions in the
1659 ionosphere of Jupiter. *Icarus, 150*(2), 261–278. https://doi.org/10.1006/icar.2001.6590

1660 Kirsch, E., Wilken, B., Gloeckler, G., Galvin, A. B., Geiss, J., Hovestadt, D. (1998). Search for
1661 lunar pickup ions. COSPAR Colloquia Series, Beijing, 9, 65–69.
1662 https://doi.org/10.1016/S0964-2749(98)80011-5

1663 Kis, A., Scholer, M. Klecker, B. Möbius, E. Lucek, E. A. Reme, H. Bosqued, J. M. Kistler, L.
1664 M., & Kucharek, H. (2004). Multi-spacecraft observations of diffuse ions upstream of Earth's
1665 bow shock. *Geophysical Research Letters, 31, L20801*, https://doi.org/10.1029/2004GL020759

1666 Klecker, B., Möbius, E., Hovestadt, D., Scholer, M., Gloeckler, G., & Ipavich, F. M. (1986).
1667 Discovery of energetic molecular ions (NO^+ and O_2^+) in the storm ring current. *Geophysical*
1668 *Research Letters, 13*, 632-635. https://doi.org/10.1029/GL013i007p00632

1669 Köhnlein, W. (1989). A model of the terrestrial ionosphere in the altitude interval 50–4000 km
1670 II. Molecular ions (N_2^+, NO^+, O_2^+) and electron density, *Earth Moon Planets, 47*, 109-163.
1671 https://doi.org/10.1007/BF00058139

1672 Krimigis, S. M., Mitchell, D. G., Hamilton, D. C., Dandouras, J., Armstrong, T. P., Bolton, S. J.,
1673 et al. (2002). A nebula of gases from Io surrounding Jupiter. *Nature, 415*, 6875, 994-996.
1674 https://doi.org/10.1038/415994a
1675 Krimigis, S. M., Mitchell, D. G., Hamilton, D. C., Livi, S., Dandouras, J., Jaskulek, et al. (2004).
1676 Magnetosphere Imaging Instrument (MIMI) on the Cassini mission to Saturn/Titan, *Space*
1677 *Science Reviews, 114*, 233-329. https://doi.org/10.1007/s11214-004-1410-8
1678 Kunde, V. G., Flasar, F. M., Jennings, D. E., Bézard, B., Strobel, D. F., Conrath, B. J., et al.,
1679 (2004). Jupiter's atmospheric composition from the Cassini Thermal Infrared Spectroscopy
1680 Experiment. *Science, 305*, 5690, 1582-1587. https://doi.org/10.1126/science.1100240
1681 Kuppers, M., & Schneider, N. M. (2000). Discovery of chlorine in the Io torus. *Geophysical*
1682 *Research Letters, 27*, 513-516. https://doi.org/10.1029/1999GL010718
1683 Lennartsson, O. W., Collin, H. L., Ghielmetti, A. G., & Peterson, W. K. (2000). A statistical
1684 comparison of the outflow of NO^+, NO^+ and O_2^+ molecular ions with that of atomic O^+ ions
1685 using Polar/TIMAS observations. *Journal of Atmospheric and Solar-Terrestrial Physics, 62*,
1686 477-483. https://doi.org/10.1016/S1364-6826(00)00019-5
1687 Liu, H.-L., Foster, B. T., Hagan, M. E., McInerney, J. M., Maute, A., Qian, L., Richmond, A. D.,
1688 Roble, R. G., Solomon, S. C., Garcia, R. R., Kinnison, D., Marsh, D. R., Smith, A. K., Richter,
1689 J., Sassi, F., & Oberheide, J. (2010). Thermosphere extension of the Whole Atmosphere
1690 Community Climate Model. *Journal of Geophysical Research: Space Physics,* 115, A12,
1691 A12302. https://doi.org/10.1029/2010JA015586
1692 Liu, H.-L., Bardeen, C. G., Foster, B. T., Lauritzen, P., Liu, J., Lu, G., . . . Wang, W. (2018).
1693 Development and validation of the Whole Atmosphere Community Climate Model with

thermosphere and ionosphere extension (WACCM-X 2.0). *Journal of Advances in Modeling Earth Systems, 10*, 381–402. https://doi.org/ 10.1002/2017MS001232

Luhmann, J. G. (2003). Expected heliospheric attributes of Jovian pickup ions from the extended neutral gas disk. *Planetary and Space Science, 51,* 387–392. https://doi.org/10.1016/S0032-0633(03)00034-5

Mahaffy, P. R., H. B. Niemann, A. Alpert, S. K. Atreya, J. Demick, T. M. Donahue, D. N. Harpold, & T. C. Owen (2000). Noble gas abundance and isotope ratios in the atmosphere of Jupiter from the Galileo Probe Mass Spectrometer. *Journal of Geophysical Research*, 105(E6), 15061–15071. https://doi.org/10.1029/1999JE001224

Mall, U. A., Christon, S. P., Kirsch, E., & Gloeckler, G. (2002). On the solar cycle dependence of the N^+/O^+ content in the magnetosphere and its relation to atomic N and O in the Earth's exosphere. *Geophysical Research Letters, 29*(12), 1593. https://doi.org/10.1029/2001GL013957

Mall, U., Kirsch, E., Cierpka, K., Wilken, B., Soding, A., Neubauer, F., Gloeckler, G., & Galvin, A. (1998). Direct observation of lunar pick-up ions near the Moon. *Geophysical Research Letters*, 25, 3799–3802. https://doi.org/10.1029/ 1998GL900003.

Martens, H. R., Reisenfeld, D. B., Williams, J. D.,Johnson, R. E., & Smith, H. T. (2008). Observations of molecular oxygen ions in Saturn's inner magnetosphere. *Geophysical Research Letters, 35*, L20103. https://doi.org/10.1029/2008GL035433

Mauk, B. H., Cohen, I. J., Haggerty, D. K., Hospodarsky, G. B., Connerney, J. E. P., Anderson, B. J., et al. (2019). Investigation of mass/charge-dependent escape of energetic ions across the magnetopauses of Earth and Jupiter. *Journal of Geophysical Research: Space Physics, 124*. https:// doi.org/10.1029/2019JA026626

1717 McComas, D. J. Allegrini,, F., Bochsler, P., Frisch, P., Funsten, H. O., Gruntman, M.,. et al.
1718 (2009), Lunar backscatter and neutralization of the solar wind: First observations of neutral
1719 atoms from the Moon. *Geophysical Research Letters, 36*, L12104, doi:10.1029/2009GL038794
1720 McEwen, A. S., Keszthelyi, L. P., Lopes, R., Schenk, P. M., & Spencer, J. R. (2007). The
1721 Lithosphere and Surface of Io, in *Jupiter, The Planet, Satellites and Magnetosphere*, Editors:
1722 Bagenal, F., Dowling, T. E., & McKinnon, W. B., Cambridge, UK: Cambridge University
1723 Press, 307-326. isbn: 9780521035453
1724 McKenna-Lawlor, S., Li, L., Barabash, S., Kudela, K., Balaz, J., Strharsky, I., Brinkfeldt, K.,
1725 Gunell, H., Shen, C., Shi, J., Cao, J.-B., Zong, Q., Fu, S-Y., Roelof, E. C., Brandt, P. C., &
1726 Dandouras, I. (2005). The NUADU experiment on TC-2 and the first Energetic Neutral Atom
1727 (ENA) images recorded by this instrument. *Annales Geophysicae, 23*, 2825–2849.
1728 https://doi.org/10.5194/angeo-23-2825-2005
1729 Mitchell, D. G., Roelof, E. C., Sanderson, T. R., Reinhard, R., & Wenzel, K.-P. (1983).
1730 ISEE/IMP observations of simultaneous upstream ion events. *Journal of Geophysical*
1731 *Research, 88*, 5635-5644. https://doi.org/10.1029/JA088iA07p05635
1732 Moore, T. E., Fok, M.-C., & Garcia-Sage, K. (2014). The ionospheric outflow feedback loop.
1733 *Journal of Atmospheric and Solar-Terrestrial Physics,* 115-116, 59-66.
1734 https://doi.org/10.1016/j.jastp.2014.02.002
1735 Nesvorný, D., Jenniskens, P., Levison, H. F., Bottke, W. F., Vokrouhlický, D., & Gounelle, M.
1736 (2010). Cometary origin of the zodiacal cloud and carbonaceous micrometeorites. implications
1737 for hot debris disks. *Astrophysical Journal, 713, 2*, 816-836. https://doi.org/10.1088/0004-
1738 637X/713/2/816

1739 Nishida, A. (1994). The GEOTAIL mission. *Geophysical Research Letters, 21*, 25, 2871-2873.
1740 https://doi.org/10.1029/94GL01223

1741 Ogawa, Y., S. C. Buchert, A. Sakurai, S. Nozawa, & R. Fujii (2010). Solar activity dependence
1742 of ion upflow in the polar ionosphere observed with the European Incoherent Scatter
1743 (EISCAT) Tromsø UHF radar. *Journal of Geophysical Research,* 115, A07310.
1744 https://doi.org/10.1029/2009JA014766

1745 Peterson, W. K., Abe, T., Fukunishi, F., Greffen, M. J., Hayakawa, H., et al. (1994). On the
1746 sources of energization of molecular ions at ionospheric altitudes. *Journal of Geophysical*
1747 *Research,* 99, 23,257–23,274. https://doi.org/10.1029/94JA01738

1748 Peterson, W. K., Sharp, R. D., Shelley, E. G, Johnson, R. G., &Balsiger, H. (1981). Energetic ion
1749 composition of the plasma sheet. *Journal of Geophysical Research,* 86, 761-767.
1750 https://doi.org/10.1029/JA086iA02p00761

1751 Peterson, W. K., Y.-K. Tung, C. W. Carlson, J. H. Clemmons, H. L. Collin, R. E. Ergun, et al.

1752 (1998). Simultaneous observations of solar wind plasma entry from FAST and POLAR.
1753 *Geophysical Research Letters,* 25, 12, 2081-2084. https://doi.org/10.1029/98GL00668.

1754 Plane, J. M. C. (2012). Cosmic dust in the Earth's atmosphere (Critical Review), *Chemical*
1755 *Society Reviews,* 41, 6507-6518. https://doi.org/10.1039/C2CS35132C

1756 Plane, J. M. C., Flynn, G. J., Määttänen, A., Moores, J. E., Poppe, A. R., Carrillo-Sanchez, J. D.,
1757 Listowski, C. (2018). Impacts of Cosmic Dust on Planetary Atmospheres and Surfaces. Space
1758 Science Reviews, 214:23, 1-42. https://doi.org/10.1007/s11214-017-0458-1

1759 Plane, J. M. C., Gómez-Martín, J. C., Feng, W., & Janches, D. (2016). Silicon chemistry in the
1760 mesosphere and lower thermosphere. *Journal of Geophysical Research Atmospheres,* 121,
1761 3718–3728. https://doi.org/10.1002/2015JD024691

1762 Poppe, A. R. (2016). An improved model for interplanetary dust fluxes in the outer solar system.
1763 *Icarus, 264*, 369-386. https://doi.org/10.1016/j.icarus.2015.10.001
1764 Poppe, A. R., Halekas, J. S., Szalay, J. R., Horányi, M., Levin, Z., & Kempf, S. (2016).
1765 LADEE/LDEX observations of lunar pickup ion distribution and variability. *Geophysical*
1766 *Research Letters, 43*, 3069–3077. https://doi.org/10.1002/2016GL068393
1767 Price, G. D., & Jacka, F. (1991). The influence of geomagnetic activity on the upper
1768 mesosphere/lower thermosphere in the auroral zone. I. Vertical winds. *Journal of Atmospheric*
1769 *and Solar-Terrestrial Physics, 53*, 10, 909–922. https://doi.org/10.1016/0021-9169(91)90004-
1770 Q
1771 Redmon, R. J., Peterson, W. K., Andersson, L., Richards, P. G., & Yau, A. W. (2014). An
1772 assessment of the role of soft electron precipitation in global ion upwelling. *Journal of*
1773 *Geophysical Research: Space Physics, 119*, 7665–7678,
1774 https://doi.org/10.1002/2014JA020061.
1775 Richards, P. G. (2013). Solar Cycle Changes in the Photochemistry of the Ionosphere and
1776 Thermosphere. In *Modeling the Ionosphere-Thermosphere System* (eds J. Huba, R. Schunk, &
1777 G. Khazanov), John Wiley, & Sons, Ltd, Chichester, UK.
1778 https://doi.org/10.1002/9781118704417.ch3
1779 Sarantos, M., Hartle, R. E., Killen, R. M., Saito, Y., Slavin, J. A., & Glocer, A. (2012), Flux
1780 estimates of ions from the lunar exosphere, *Geophysical Research Letters, 39*, L13101,
1781 https://doi.org/10.1029/2012GL052001
1782 Scholer, M., Kucharek, H., & Giacalone, J. (2000). Cross-field diffusion of charged particles and
1783 the problem of ion injection and acceleration at quasi-perpendicular shocks. *Journal of*

Geophysical Research: Space Physics, 105, 18,285-18,293. https://doi.org/10.1029/1999JA000324.

Seki, K., Keika, K., Kasahara, S., Yokota, S., Hori, T., Asamura, K., et al. (2019). Statistical properties of molecular ions in the ring current observed by the Arase (ERG) satellite. https://doi.org/doi: 10.1029/2019GL084163

Shelley, E. G., Johnson, R. G., & Sharp, R. D. (1972). Satellite observations of energetic heavy ions during a geomagnetic storm. *Journal of Geophysical Research*, 77(31), 6104-6110. https://doi.org/10.1029/JA077i031p06104

Shen, Y., Knudsen, D. J., Burchill, J. K., Howarth, A. D., Yau, A. W., Miles, et al. (2018). Low-altitude ion heating, downflowing ions, and bbelf waves in the return current region. *Journal of Geophysical Research: Space Physics,* 123(4), 3087-3110. https://doi.org/10.1002/2017JA024955

Skjæveland, Å., Moen, J., & Carlson, H. C. (2014), Which cusp upflow events can possibly turn into outflows?. *Journal of Geophysical Research: Space Physics, 119,* 6876–6890. https://doi.org/10.1002/ 2013JA019495

Sorathia, K. A., Merkin, V. G., Ukhorskiy, A. Y., Mauk, B. H., & Sibeck, D. G. (2017). Energetic particle loss through the magnetopause: A combined global MHD and test-particle study. *Journal of Geophysical Research, Space Physics, 122*, 9329–9343. https://doi.org/10.1002/2017JA024268

Strangeway, R. J., Ergun, R. E., Su, Carlson, Y.-J., C. W., & Elphic, R. C. (2005). Factors controlling ionospheric outflows as observed at intermediate altitudes. *Journal of Geophysical Research,* 110, A03221.https://doi.org/10.1029/2004JA010829

1806 Tape, J. W., W. M. Gibson, J. Remillieu, R. Laubert, & H. E. Wegner (1976). Energy loss of
1807 atomic and molecular ion beams in thin foils. *Nuclear Inststruments and Methods, 132*, 75-77,
1808 https://doi.org/10.1016/0029-554X(76)90713-8
1809 Tanaka, T., Saito, Y., Yokota, S., Asamura, K., Nishino, M. N., Tsunakawa, et al. (2009).First in
1810 situ observation of the Moon-originating ions in the Earth's Magnetosphere by MAP-PACE on
1811 SELENE (KAGUYA). *Geophysical Research Letters,* 36, L22106.
1812 https://doi.org/10.1029/2009GL040682
1813 Taut, A., Berger, L., Drews, C., & Wimmer-Schweingruber, R. F. (2015). Composition of inner-
1814 source heavy pickup ions at 1 AU: SOHO/CELIAS/CTOF observations—Implications for the
1815 production mechanisms. *Astronomy and Astrophysics, 576*(A55). https://doi.org/10.1051/0004-
1816 6361/201425139
1817 Terasawa, T., Fujimoto, M., Mukai, T., Shinohara, I., Saito, Y., Yamamoto, T., et al. (1997).
1818 Solar wind control of density and temperature in the near-Earth plasma sheet:
1819 WIND/GEOTAIL collaboration. *Geophysical Research Letters, 24*, 935–938.
1820 https://doi.org/10.1029/96GL04018
1821 Thomsen, M. F., D. B. Reisenfeld, D. M. Delapp, R. L. Tokar, D. T. Young, F. J. Crary, E. C.
1822 Sittler, M. A. McGraw, & J. D. Williams (2010). Survey of ion plasma parameters in Saturn's
1823 magnetosphere. *Journal of Geophysical Research, 115*, A10220.
1824 https://doi.org/10.1029/2010JA015267
1825 Verbischer, A. J., Skrutskie, M. F., & Hamilton, D. P. (2009). Saturn's largest ring. *Nature, 461*,
1826 1098–1100. https://doi.org/10.1038/nature08515

1827 Vondrak, T., Plane, J. M. C., Broadley, S., & Janches, D. (2008). A chemical model of meteoric
1828 ablation. *Atmospheric Chemistry and Physics,* 8(23), 7015-7031. https://doi.org/10.5194/acp-8-
1829 7015-2008
1830 Welling, D. T., & Liemohn, M. W. (2016). The ionospheric source of magnetospheric plasma is
1831 not a black box input for global models. *Journal of Geophysical Research, Space Physics, 121*,
1832 5559–5565. https://doi.org/10.1002/2016JA022646
1833 Williams, D. J., McEntire, R. W., Schlemm, C. II, Lui, A. T. Y., Gloeckler, G., Christon, S. P., &
1834 Gliem, F. (1994). Geotail energetic particles and ion composition instrument. *Journal of*
1835 *Geomagnetism and Geoelectricity, 46*, 39–57. https://doi.org/10.5636/jgg.46.39
1836 Wilson, G. R., Ober, D. M., Germany, G. A., & Lund, E. J. (2004). Nightside auroral zone and
1837 polar cap ion outflow as a function of substorm size and phase. *Journal of Geophysical*
1838 *Research, 109*, A02206. https://doi.org/10.1029/2003JA009835.
1839 Wilson, J. K., Mendillo, M., & Baumgardner, J. (2002). The dual sources of Io's sodium clouds.
1840 *Icarus, 157*, 476–489 https://doi.org/10.1006/icar.2002.6821
1841 Yau, A. W., A. Howarth, A., Peterson, W. K., & Abe, T. (2012). Transport of thermal-energy
1842 ionospheric oxygen (O^+) ions between the ionosphere and the plasma sheet and ring current at
1843 quiet times preceding magnetic storms. *Journal of Geophysical Research, 117*, A07215.
1844 https://doi.org/10.1029/2012JA017803
1845 Yau, A. W., Whalen, B. A., Goodenough, C., Sagawa, E., & Mukai, T. (1993). EXOS D
1846 (Akebono) observations of molecular NO^+ and N_2^+ upflowing ions in the high-altitude auroral
1847 ionosphere. *Journal of Geophysical Research, 98*(A7), 11205–11224.
1848 https://doi.org/10.1029/92JA02019

1849 Yau, A. W., Peterson, W. K., & T. Abe (2011). Influences of the ionosphere, thermosphere and
1850 magnetosphere on ion outflows. In *The Dynamic Magnetosphere*, Edited by W. Liu, & M.
1851 Fujimoto, Springer, Netherlands, 283-314. https://doi.org/10.1007/978-94-007-0501-2_16
1852 Yokota, S., & Saito, Y. (2005). Estimation of picked-up lunar ions for future compositional
1853 remote SIMS analyses of the lunar surface. *Earth Planets and Space, 57,* 281–289.
1854 10.1186/BF03352564
1855 Yu, Y., & Ridley, A. J. (2013). Exploring the influence of ionospheric O+ outflow on
1856 magnetospheric dynamics: dependence on the source location. *Journal of Geophysical*
1857 *Research, Space Physics, 118*, 1711–1722. https://doi.org/10.1029/2012JA018411.
1858 Zbinden, P. A., Hidalgo, M. A., Eberhahdt, P., & Geiss, J. (1975). Mass spectrometer
1859 measurements of the positive ion composition in the D- and E-regions of the ionosphere.
1860 *Planetary and Space Science, 23, 12,* 1621-1642. https://doi.org/10.1016/0032-0633(75)90090-
1861 2
1862